UNIVERSITY OF EXETER

DOCTORAL THESIS

Giving Metamaterials a Hand

Electromagnetic Interactions in Chiral Metamaterials

Author:

Lauren Barr

Supervisors:

Prof. Euan Hendry

Prof. Alastair P. Hibbins

A thesis submitted for the degree of

Doctor of Philosophy in Physics

in the

EPSRC Centre for Doctoral Training in Metamaterials

College of Engineering, Mathematics and Physics

7th August 2018

Declaration of Authorship

I, Lauren Barr, declare that all material in this thesis which is not my own work, and any material previously submitted and approved for the award of a degree by this University, has been clearly identified.

Signed:

_____

Date:

_____

For George Francis Henry Loan

Acknowledgements

There are so many people who have contributed to the completion of this thesis in all manner of ways. I hope to use the space here to thank all of them.

Firstly, my huge and sincere thanks is extended to my supervisors, Euan and Alastair. They have encouraged and supported me during the smooth and rough parts of my PhD experience. They set me back on the path when I wandered off too far, but always gave me a free rein to explore when I wanted it. I can say for sure I would not have achieved anywhere near as much without both of them. Thank you so much for your energy and devotion!

I also owe a great deal to the members of my research group, in particular those who have helped out with the technical side of things. Roy never failed to encourage and inspire with his immense passion for physics. Ian has always been ready to contribute from his vast knowledge of all things metamaterial. Ben gave offered assistance in the early days of my PhD. Simon has so much enthusiasm for physics, he has never failed to inspire and teach. Sam H is a guru of fabrication and coffee. Cam has always helped with material characterisation, and Gareth has provided many unusual insights to all areas of physics and life. The guys in the workshop, stores and IT support helped immensely with tasks I couldn't have done myself, in particular Pete, Kevin, Nick, Paul, John, Richard and Chris F. You are all awesome - thank you!

Huge thanks are also due to my collaborators in Birmingham. Qinghua, Biao and Shuang taught me about the world of topological physics, with some help from Andrey, and gave me the chance to explore a new topic and work with some top physicists. Thank you for that!

Aside from these, I want to thank all the others who enriched my PhD experience beyond a simple academic endeavour. My long-time office-mates Sathya, Erick and King Chris made every day fun, even when the times got tough, with their rich humour and infinite distractions. In the last few months of my PhD studies I explored the land of Chult every other Wednesday, and I'd like to thank my fellow adventurers Sam S, Tom G, Toby, Gareth, Ben, Chris M and Slee for the great times. Others who have provided happy memories from my time in G33 are Peter, Rayko, Ilya, Angus, Natalie, Jacob, Tom C, Miguel and Joseph - thanks for all the fun and the many cups of tea! The corridors of the physics building were also happy places, and I enjoyed running into many other colleagues there (occasionally also in the pub), particularly Matt, Gareth, Nicola, Iddo, Ana, Jake, Elias, Liam, Santi, Liz, Jess, Ahmad and Tom G II. It just wouldn't have been the same without you!

Another group of people who have really contributed to my time in Exeter are the Exeter University and Optics Society. We have had so much fun meeting the scientists of the future at scientific outreach events. I want to thank in particular Alba and Henry for their dedication to sharing science with the public, and making it so enjoyable for everyone. You guys are incredible!

Although they have been far away, my family have been huge part of life and reason for my happiness. Mum has encouraged me to do what makes me happy, and Dad is always ready with a joke and a bit of craic. They've both had my back through it all. Christie and James have kept my play-list and wine-list in top form. My Grandparents, Aunties, Uncles and Cousins have provided many, many welcome excuses to come home and celebrate being a family. Thank you all for the love and support!

Finally I'd like to thank Adolfo for being there through the whole process, offering advice from personal experience, plenty of encouragement, enthusiasm for chilling in Dartmoor (or on the sofa), and yummy food! I can't thank you enough for everything you do!

UNIVERSITY OF EXETER

Abstract

EPSRC Centre for Doctoral Training in Metamaterials

College of Engineering, Mathematics and Physics

Doctor of Philosophy in Physics

Giving Metamaterials a Hand

by Lauren Barr

The focus of this thesis is the interaction of electromagnetic fields with chiral structures in the microwave regime. Through this study, which focuses on three regimes of electromagnetic interactions, I aim to develop a deeper understanding of the consequences and manifestations of chiral interactions The structures are on the order of, or smaller than, the wavelength of the probing radiation. As the structures are chiral, they have broken inversion symmetry, and exist in two states where one is the mirror image of the other. The results in this thesis can have impacts on future optical communications technologies and methods of sensing biological molecules.

To begin with, the manipulation of the circular polarisation of a propagating beam by bilayer chiral metasurfaces is investigated. The metasurfaces consist of two layers of stacked crosses with a twist between top and bottom layers, forming chiral metamolecules. A broad frequency region of dispersionless polarisation rotation appears between two resonances, due to alignment between electric and magnetic dipoles. The dependence of this effect on the layer separation is studied for two similar metasurfaces.

Evanescent chiral electromagnetic fields are the focus of the next chapter. An array of chiral antennas produces chiral near-fields at their resonant frequency. Aligned

and subwavelength helices placed within this field interact differently depending on the handedness of the field with respect to the handedness of the helices. This difference in interaction strength is measured for the helices and an effective medium model where multipolar interactions are forbidden. Comparison of these two systems leads to the conclusion that the contribution to a chiral interaction from multipolar modes is minimal, in contrast to previous publications.

The third study concentrates on the electromagnetic wave bound to an "infinitely long" metal helix. The helix has infinite-fold screw symmetry, and this leads to interesting features in the energy-dispersion of the waves it supports. The broad frequency range of high, tunable, dispersionless index is interpreted using a geometrical approach, and the factors that limit the bandwidth explained. A modified geometry is suggested for increased bandwidth.

The final part of the thesis is dedicated to future work, based on the results presented thus far. Three suggestions for future study are presented, including chiroptical signals from higher-order chiral arrangements, the effect of reflecting surfaces next to chiral objects and the possible use of orbital angular momentum for chiroptical measurements.

Contents

List of Figures

Chapter 1

Introduction

1.1 Motivation

Symmetry is fundamental to life. More specifically, a lack of symmetry.

The presence of objects and systems that lack inversion symmetry in nature has fascinated scientists for centuries. First discovered by Arago when he looked at sunlight passing through a quartz crystal [1], it was some time before Lord Kelvin coined the term chiral [2]. Before this, Pasteur discovered the role chirality played in nature, which he reported in a chapter of a book dedicated to Biot, another scientist who delved into the study of chirality [3]. He noticed that the sediment at the bottom of a wine barrel rotated light in one direction, while the same crystals formed in the lab did not. This was due to the fact that molecules of only one handedness were formed by the bacteria that produced the wine, as the process itself is mediated by chiral molecules and structures within the bacteria. The chiral origins of life are still a mystery, but have sparked many intriguing theories.

Biological systems across all length scales display chirality. From sugars and amino acids, to complex proteins, to microstructures in some beetle scales and the macroscopic patterns of snail shells. The handedness of molecules determines their interaction within a biological system. An example of this is the molecule carvone, which is responsible for the smell of both spearmint leaves and caraway seeds.

While chemically identical in both, it exists in the right-handed state, or enantiomer, in caraway, and the left-handed in spearmint. The receptors in our noses are chiral, and so can distinguish between the two enantiomers, so our brain knows that spearmint leaves and caraway seeds smell very different.

Apart from this somewhat frivolous example, other more sinister consequences of biological chirality have arisen. In addition to the health risks that accompany undetermined chirality, there is also a financial loss associated. The common painkiller ibuprofen is handed, and exists in two enantiomers. In manufacturing the drug, equal quantities of both enantiomers are produced, but one is completely inert. This means companies produce and sell double the necessary quantity of ibuprofen, and many other drugs. There is a great deal of work looking at ways to efficiently separate molecules based on handedness, or preferably produce only one handedness in the first place, as nature does.

As well as being a hindrance for drug companies, chirality is a useful degree of freedom in terms of electromagnetic radiation. Controlling polarisation has lead to directive, broadband antennas, the concepts of which are still used in today's Wi-Fi. Some chiral materials exhibit the photonic spin Hall effect, and others support topologically protected states. Both of these phenomena may pave the way to new technologies in spintronics and quantum computing in the future.

An understanding of how chiral electromagnetic waves interact with and manipulate chiral objects is beneficial to fields in physics, chemistry and biology. However in recent years, works claiming to enhance the sensitivity of chiral molecule detection thanks to "superchiral" light have caused controversy. This work and the others that followed have given rise to an industrious area of research, but the systems under study are often complicated by the use of biological samples and difficult fabrication techniques. The emergence of the study of microwave metamaterials,

where structures are designed on the millimetre length scale to manipulate millimetre wavelengths, can lend a hand in this quest, by simplifying and extracting the underlying phenomena behind the observations.

Furthermore, there has been a surge in the design of metamaterials that manipulate the polarisation and propagation of waves across many frequency bands. The main challenge in this area is to create metamaterials with broad operational bandwidths, or in situ tunability, for applications in multimode optical communications. Delving into the origins of the propagation and polarisation of waves in chiral structures yields insights into how the geometry can be tuned to achieve broader operational bandwidths and more efficient control.

1.2 Aim

The aim of this thesis is to probe the effects of electromagnetic chirality using microwave metamaterials by studying, experimentally and numerically, the interaction of GHz frequency radiation with structured chiral media. Three different kinds of wave-matter interaction are studied to develop an understanding of the different regimes in which chiral interactions can be found. I study far-field chiral waves, evanescent chiral near-fields and waves bound to a chiral wave-guide. The result of these studies is a deeper understanding of the origins of the effects observed in all three regimes, and an idea for how to better manipulate a variety of chiral interactions for potential applications in communication and sensing.

1.3 Outline

In chapter 2, the historical background and a review of the relevant literature on the study of chirality and metamaterials are presented. Chapter 3 provides details on

the fabrication, experimental and numerical techniques used to gather the results presented in the following chapters.

Chapter 4 studies how chiral metasurfaces manipulate the circular polarisation of GHz frequency waves in the far-field regime. Two bilayer metasurfaces are compared. The first is an array of metal crosses on the top and bottom sides of a dielectric layer. The top and bottom crosses are aligned, but those on the bottom are twisted with respect to those on the top, creating a chiral unit cell. In the second metasurface the bottom layer of crosses is replaced by an array of cross-shaped holes in a conducting layer. Broadband rotation of the plane of linear polarisation is observed for the second metasurface, and this is explained as the result of two overlapping resonances.

Chapter 5 presents the results from a study of near-field chiral interactions. Arrays of chiral antennas operating at 16 GHz generate evanescently decaying fields that are right and left handed. These chiral fields are probed with a layer of subwavelength, aligned helices by measuring their interaction with antennas of opposite handedness. Non-local contributions to the chiral interaction are investigated through comparison to a local homogeneous approximation for the helical layer. No significant enhancement is observed in the non-local medium over the local approximation, providing evidence that non-local contributions to chirality are small. This result has implications for the enhanced sensing of chiral molecules.

Chapter 6 discusses the bound waves on an infinitely long helical wave-guide. The screw symmetry of the helix causes interesting features in the energy-dispersion of the bound wave, including broadband linear dispersion and high index, ideal for slow wave applications. This effect and the factors that limit the frequency range of the linear dispersion are discussed in terms of the geometrical parameters of the helix, and a theoretical description of the dispersion. The insights gained from this study lead to the design of an improved geometry with a larger operational bandwidth.

Chapter 7 highlights some future work to be undertaken based on the previous results. Studying the effect of positioning subwavelength chiral objects in arrays with large chiral unit cells may offer insight into the detection of chiral molecules and their mutual interactions. I also suggest looking more closely at chiral objects placed next to reflecting surfaces, as initial results show that reflected waves exhibit complex fluctuations in their handedness based on separation, orientation and losses in the chiral medium. Finally I discuss an investigation into the effect of orbital angular momentum in waves and evanescent fields on chiroptical interactions. Recent publications suggest this could be a route to enhanced detection of chiral molecules, and will manifest differently in the near- or far-field, and in aligned or randomly oriented molecules.

Chapter 8 contains the overall conclusions that can be derived from the work presented in this thesis.

Chapter 2

Background Theory

Introduction

In this chapter I will review the two main concepts addressed in this thesis: chirality and metamaterials.

I will begin by outlining the important historical events in the study of chirality, highlighting how these discoveries influenced the field today. This will lead to a general definition of chirality, which can be applied to materials and electromagnetic fields. When discussing the latter of these, the idea of enhanced or "superchiral" fields will be examined.

I will then move on to look at metamaterials and metasurfaces, focusing particularly on the work on chiral metamaterials and metasurfaces that has been carried out. Finally an overview of homogenisation is included in this section, as one defining feature of metamaterials.

Along the way, the relevant chapters containing work that builds upon the background knowledge will be highlighted.

2.1 Chirality

2.1.1 Historical Background

This introduction is of general interest, and sets much of the current work in historical context.

The first experimental observation of chirality was performed by Arago in 1811, when he studied sunlight passing through a quartz crystal and two crossed polarisers. Later in 1818 Biot discovered a second type of quartz crystal that rotated the plane of polarised light in the opposite direction [4]. He also discovered that the effects observed by Arago where due to two distinctive (but closely related) phenomena; optical rotation and circular dichroism, which will be reviewed in section 2.1.4.

Optical rotation was also discovered in liquids (turpentine) and solutions of camphor, sugar and tartaric acid. It became clear that the effect could stem from properties of the individual molecules, as well as from the arrangement of atoms such as in a quartz crystal.

The first known experiment to study the optical rotation of waves travelling through artificial media was performed by Bose in 1898 [5]. Through this study he clearly demonstrated that optical activity is due to a twist in the medium. Still, it was not until 1904 when Lord Kelvin first defined chirality, when he stated "I call any geometrical figure, or any group of points, chiral, and say it has chirality, if its image in a plane mirror, ideally realized, cannot be brought to coincide with itself" [2].

Chiral objects can exist in two distinct configurations, called enantiomorphs (enantiomers in the context of molecules), often referred to as left- or right-handed (LH, RH). It is only possible to convert between RH and LH enantiomers via a parity inversion (taking each point of the object and inverting it in space), and not by any

rotation, translation or reversal of time. Enantiomorphs can be distinguished most easily through an interaction with another chiral object, such as chiral electromagnetic radiation in the chiroptical techniques outlined in section 2.1.4. The weak force also discriminates between enantiomorphs, however the effect is incredibly small.

2.1.2 Defining Chirality

This section presents a full definition of chirality that is relevant to all chapters.

The definition provided by Kelvin is satisfactory for 3-dimensional stationary objects. However if we are to consider time-varying electric and magnetic fields, we need something more robust. Also, there are cases where the effects of chirality can be detected in systems that are not truly chiral, and it will be important to distinguish these.

True Chirality

The issue with moving objects is illustrated through the example of a spinning cone in figure 2.1. In figure 2.1 (A) the cone is stationary, and a parity inversion (P) results in an object that can be made identical to the original via a rotation of π radians about an axis perpendicular to the cone axis (R), and time reversal (T). In figure 2.1 (B) the cone is translating along its axis, and a parity inversion does not produce the same result as a rotation and time reversal. Therefore we can see that, while a stationary spinning cone is not chiral, a translating spinning cone does exhibit true chirality[6].

This lack of clarity prompted the work of Barron, who settled upon a definition of chirality that is widely accepted throughout the scientific community. He stated that "true chirality is shown by systems existing in two distinct enantiomeric states that are inter-converted by space inversion, but not by time reversal combined with any proper spatial rotation" [6].

Applying the same principles as above to electrons, treated as spinning spheres, we see that only when an electron is translating along an axis parallel to the projection of its spin can it be considered chiral. This raises some interesting questions about the link between chirality and relativity, as the direction of motion of an electron with any given spin state is dependent on the relative motions of electron and observer. Furthermore, we can extend this line of thought to photons. When propagating at the speed of light in a vacuum photons will have a well-defined chirality determined by their spin state and direction of propagation. However when travelling through a medium their velocity reduces, even to the point at which they become stationary. Therefore it seems that in this situation defining the chirality of a circularly polarised, stationary photon is no longer possible. This highlights one issue in defining the chirality of a photon based on its spin angular momentum, a discussion that will be expanded in section 2.1.5.

Electromagnetic Chirality

Having defined a geometrical, time-independent chirality, we can now consider electromagnetic (EM) chirality. We have considered spin angular momentum in single electrons and photons, but we can also predict the chirality of electric and magnetic fields using a classical interpretation. Firstly we identify that a uniform static electric field is a time-even polar vector, i.e. its direction is reversed by a parity inversion, but not by time reversal. Static magnetic fields are defined as time-odd axial vectors, where they are reversed by time reversal but not by parity inversion. Any one of these fields cannot be considered chiral when isolated, as any changes to direction are reversed by a rotation of π radians. In 1984 M. S. Curie noticed that parallel electric and magnetic fields would produce a spatially dissymmetric system (i.e. one that lacks inversion symmetry). However in the case of static uniform fields this does not equate to true chirality since the arrangements produced by a parity

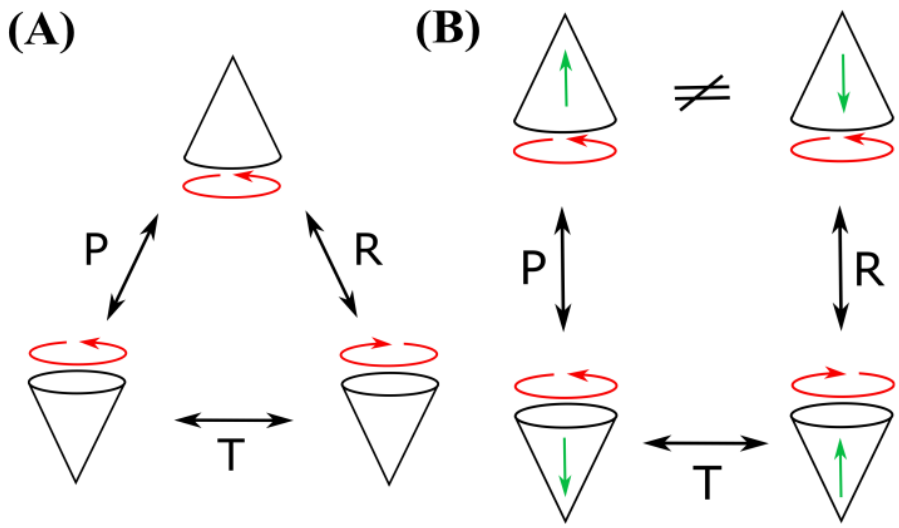

FIGURE 2.1: **Demonstration of true chirality. (A)** shows a cone that is stationary in space but spinning about its major axis, with the direction of spinning shown by the red arrow. Performing a parity inversion (P) on the cone is equivalent to a rotation (R) of π radians and time reversal (T), so the spinning cone is not a chiral object. **(B)** shows a spinning translating cone, with the direction of translation shown by a green arrow. A parity inversion, followed by time reversal and rotation does not result in the original system - the direction of translation has been reversed - so the translating spinning cone is truly chiral.

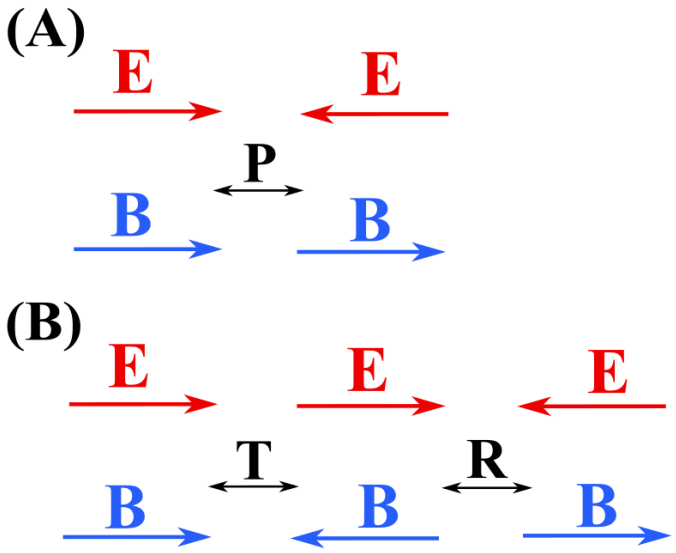

FIGURE 2.2: **The chirality of static electric (E) and magnetic (B) fields. (A)** shows how a combination of E and B fields behave under a parity inversion (P), with the E field changing sign since it is a polar vector, and the B field remaining the same since it is an axial vector. **(B)** shows that under time reversal (T), since E is time-even and B is time-odd, and rotation (R) by π radians perpendicular to the field directions, the same field configuration is achieved, as in **(A)**. This illustrates that static aligned E and B fields are not truly chiral. However adding a time dependence, specifically a phase difference of $\pm\pi/2$ radians between E and B, leads to a chiral electromagnetic field.

operation are inter-converted by time reversal, as illustrated in figure 2.2 [7].

Curie only neglected one important parameter - phase. We know that circularly polarised electromagnetic (EM) radiation is chiral, as it is a collection of photons in the same spin state, travelling through space. In a circularly polarised monochromatic plane wave, the magnetic and electric field vectors map out a helical path as the wave moves through space, while maintaining the $\pm\pi/2$ phase difference inherent to a plane wave. The handedness of the wave is determined by the sense of rotation of the electric field along the axis of propagation, or equivalently the sign of the phase relation between electric and magnetic fields. This gives two distinct defining characteristics of a circularly polarised wave; the spin angular momentum ($\mathbb{I}(\tilde{E^*} \times \tilde{E})$) and the optical helicity ($\mathbb{I}(\tilde{E^*} \cdot \tilde{B})$). $\tilde{E}$ and $\tilde{B}$ are the complex electric

and magnetic fields respectively, the * indicates the complex conjugate, and the $\mathbb{I}$ means only the imaginary part is considered. It is the optical helicity, also known as the optical chirality or chiral density, that is commonly associated with chiroptical interactions [8, 9].

Knowing this, it is possible to write a generic definition of EM chirality. This is particularly useful when discussing the notion of superchiral fields in section 2.1.5, but it has also been shown that there is a strong correlation between the chirality of near-fields around an antenna and its optical activity observed in the far-field [10].

The property now associated with electromagnetic chirality first appeared in a work by Lipkin in 1964 [11], along with nine other conserved quantities in electromagnetism. He did not attribute these to any physical property, however, and it wasn't until 2010 when Tang and Cohen used the Z^{000} zilch to define the chirality of an EM wave, C [12]. C is a time-even pseudo-scalar, that reverses sign upon inversion but is invariant under time reversal, and so obeys the conditions previously set out for true chirality.

$$Z^{000} \equiv C = \frac{\epsilon_0}{2}\mathbf{E}\cdot(\nabla\times\mathbf{E}) + \frac{1}{2\mu_0}\mathbf{B}\cdot(\nabla\times\mathbf{B}) \tag{2.1}$$

where $\mathbf{E}$ and $\mathbf{B}$ are the electric and magnetic fields of the EM wave, and ϵ_0 and μ_0 are the permittivity and permeability of free space. This can be rewritten in terms of complex field amplitudes, denoted by the tilde.

$$C = -\frac{\epsilon_0\omega}{2}\mathbb{I}\left[\tilde{\mathbf{E}}^*\cdot\tilde{\mathbf{B}}\right] \tag{2.2}$$

where ω is the frequency of the field and $\mathbb{I}$ indicates the imaginary part. Assuming unit intensity, $C_{\mathrm{CP}} = \pm\omega\epsilon_0|E_0|^2/2c$ for circularly polarised plane waves. This quantity represents the components of electric and magnetic fields that are parallel with a $\pm\frac{\pi}{2}$ phase difference. Figure 2.3 illustrates that this is true for circularly polarised light. In the top panel, a right-handed circularly polarised wave has its electric (E)

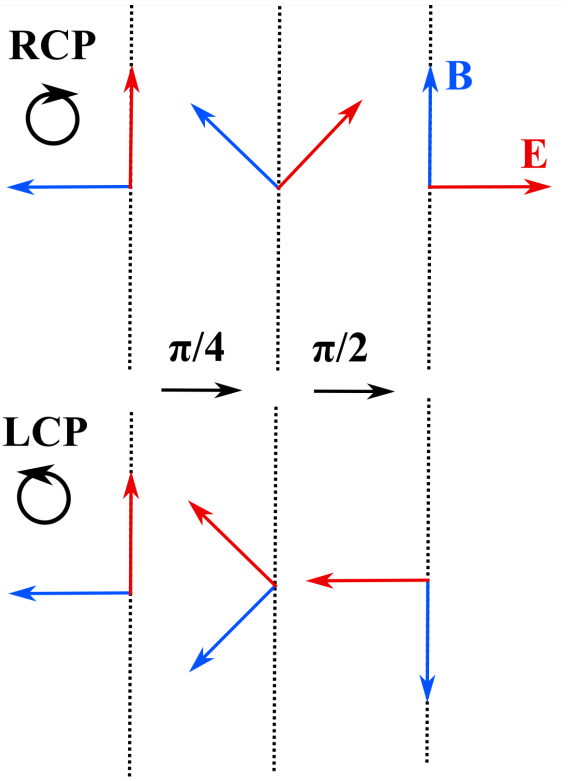

FIGURE 2.3: **Applying the definition of *C* to right- and left-circularly polarised (RCP, LCP) waves.** At phase = 0, the electric field (E, red arrow) field of a RCP wave lies along the dotted black line After a phase progression of $\pi/2$, the magnetic field (B, blue arrow) now lies along the same line, showing that this wave satisfies the condition in equation 1.36 as the fields are parallel with a $\pi/2$ phase difference. For the LCP wave there is a factor of -1 in the phase relation, as the B field leads the E field.

field along the dotted line at a particular point in phase. After the wave has passed through a phase of $\frac{\pi}{2}$ radians the magnetic field (B) is now parallel to the dashed line, and $C_{\mathrm{RCP}} = +\omega\epsilon_0|E_0|^2/2c$. The bottom panel shows a left-handed wave with the magnetic field leading the electric field, leading to a value of $C_{\mathrm{LCP}} = -\omega\epsilon_0|E_0|^2/2c$. This measure of the chirality of an EM field is not restricted to only monochromatic plane waves, and also describes evanescently decaying near-fields with overlapping parallel E and B fields.

This quantity has since been defined as the angular momentum of the curl of the field [13]. The effectiveness of such a quantity is yet to be fully understood, and this

idea will be discussed further in section 2.1.5.

Magneto-optic Effect

We rely on different interactions with RH and LH chiral EM fields to detect chirality. However, this can be misleading, as there are systems that will exhibit some of the characteristics of chirality, without being truly chiral at all.

The first notable example is a wave propagating along the direction of an external magnetic field in a gyromagnetic material, such as in a Faraday isolator. The key difference between this system and an optically active medium is the reciprocity, as illustrated in figure 2.4 [14]. When a linearly polarised wave travels through a chiral medium, the plane of polarisation will rotate in a direction determined by the handedness of the medium. If time is reversed, the wave will travel backwards through the medium, rotate in the same direction with respect to its propagation direction, and arrive on the other side with the same polarisation it started with. Therefore, reversing time does not change the handedness of the medium. If we now consider a linearly polarised wave travelling through a magneto-optic medium, the plane of polarisation will rotate, similarly to in the chiral medium. Upon time reversal of the wave, not the magnetic field in the material itself, the wave travels backwards through the medium with the opposite sense of rotation with respect to its propagation. The time-reversal symmetry has not been preserved, therefore a magneto-optic medium is not chiral according to Barron's definition.

Planar Chirality

Another interesting system to consider is a 2-dimensional or planar chiral structure. According to Kelvin and Barron's definitions, a truly chiral object must be 3-dimensional, otherwise we may move from one enantiomer to the other by rotating the object out of its plane. In other words, if RH EM fields exist on one half-space of

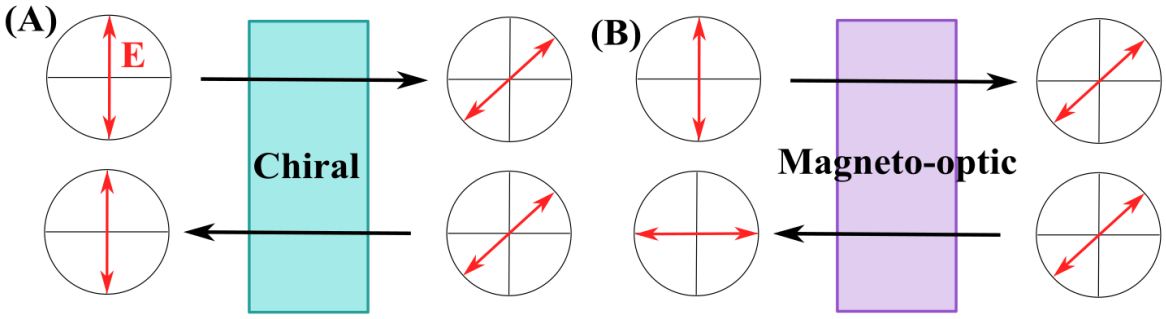

FIGURE 2.4: **Distinguishing chiral and magneto-optic media. In (A)** an EM wave with its electric field (E, red arrows) polarised vertically travels through a chiral medium and emerges with the E field having gone through a 45° rotation. Upon time reversal, or the wave travelling backwards through the chiral medium, the E field is rotated in the same direction with respect to its reversed propagation direction, and emerges on the far side, with the original vertical polarisation. In **(B)** the wave travels through a magneto-optic medium, and upon travelling back through the medium from the other side, emerges horizontally polarised, illustrating the non-reciprocity of magneto-optic media.

the structure, the fields on the other side will be equal and of opposite handedness, leading to an overall achiral field. Chiral fields can be observed in the near-fields around even achiral objects, but do not manifest in the far-field [15]. Despite this, considerable work has been done on planar chiral arrays as they are straightforward to fabricate. In any case, for a useful measure of chirality to be made, the symmetry above and below the plane must be broken, and there are several ways to achieve this.

In most cases, the presence of a substrate is sufficient to break this symmetry [16]. In the absence of a substrate, small defects in the fabrication of a real sample have also been enough to observe a measurable signatures of chirality [17]. But apart from these routes to break the geometrical symmetry, it has been proposed that the decay of the electric field across the depth of a suitably thick planar chiral structure may break the symmetry of the fields, leading to measurable chirality [18]. Ohmic losses also play an important part in determining the measured chirality of a thick planar-chiral array [19].

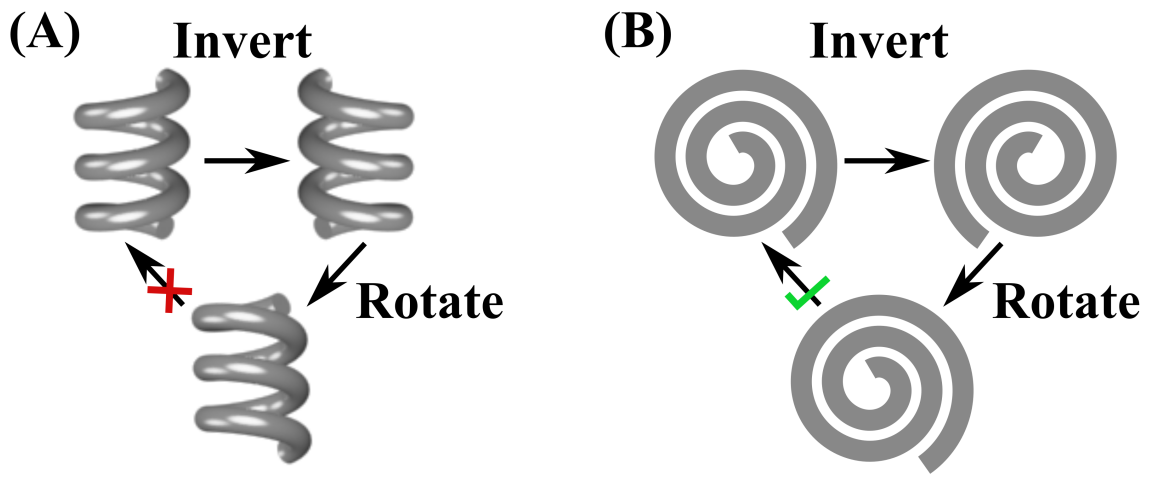

FIGURE 2.5: **Planar and three-dimensional chirality.** **(A)** shows a three-dimensionally chiral object that undergoes a parity inversion and a rotation, but remains distinguishable from the original. In **(B)** a planar chiral object can be inverted and then rotated out of its plane to return to the original, showing that a planar chiral object is not truly chiral unless it has some additional part to break the out-of-plane symmetry, such as a substrate.

An intrinsically chiral structure with only planar-chiral symmetry has recently been presented [20]. By creating an array of planar gammadions from a thick (relative to the wavelength) high-index dielectric, currents can flow out of the plane of the array. This allows in-plane magnetic fields, that can overlap with the in-plane electric fields and produce a chiral signal at normal incidence that does not change sign upon reversing the direction of incidence.

This idea that the combination of EM fields and geometry can determine the chiroptical interactions in a system has lead to another interesting phenomenon. When a planar anisotropic array is studied at angles away from normal incidence, extrinsic chirality can be measured [21]. Again, this is not a true form of chirality, as rotating the array in the plane reverses the handedness of the system, but it is a method to create easily fabricated, tunable polarisers.

2.1.3 Chiral Material Parameters

This description of chiral material parameters is particularly relevant to chapter 5.

Now, we look at the description of a bulk, homogeneous chiral medium in terms of its material parameters and interaction with electromagnetic radiation. The constitutive relations for a general medium are:

$$\begin{bmatrix} \bar{\mathbf{D}} \\ \bar{\mathbf{B}} \end{bmatrix} = \begin{bmatrix} \bar{\bar{\epsilon}} & \bar{\bar{\xi}} \\ \bar{\bar{\zeta}} & \bar{\bar{\mu}} \end{bmatrix} \begin{bmatrix} \bar{\mathbf{E}} \\ \bar{\mathbf{H}} \end{bmatrix} \tag{2.3}$$

where $\bar{\mathbf{D}}$ and $\bar{\mathbf{B}}$ are the electric displacement and magnetisation of the material, and $\bar{\mathbf{E}}$ and $\bar{\mathbf{H}}$ are the electric and magnetic fields, respectively. $\bar{\bar{\epsilon}}$ and $\bar{\bar{\mu}}$ are the permeability and permittivity of the material, and $\bar{\bar{\xi}}$ and $\bar{\bar{\zeta}}$ are the cross-coupling material parameters. Each material parameter is in general a complex 3×3 tensor. In this thesis only reciprocal and non-gyrotropic media wil be considered, so the material parameters, following Tellegen's notation become:

$$\bar{\bar{\epsilon}} = \begin{bmatrix} \epsilon_0\epsilon_{xx} & 0 & 0 \\ 0 & \epsilon_0\epsilon_{yy} & 0 \\ 0 & 0 & \epsilon_0\epsilon_{zz} \end{bmatrix} \tag{2.4}$$

$$\bar{\bar{\mu}} = \begin{bmatrix} \mu_0\mu_{xx} & 0 & 0 \\ 0 & \mu_0\mu_{yy} & 0 \\ 0 & 0 & \mu_0\mu_{zz} \end{bmatrix} \tag{2.5}$$

$$\bar{\bar{\xi}} = \begin{bmatrix} i\kappa_{xx}\sqrt{\mu_0\epsilon_0} & 0 & 0 \\ 0 & i\kappa_{yy}\sqrt{\mu_0\epsilon_0} & 0 \\ 0 & 0 & i\kappa_{zz}\sqrt{\mu_0\epsilon_0} \end{bmatrix} = -\bar{\bar{\zeta}} \tag{2.6}$$

where ϵ_0 and μ_0 are the permittivity and permeability of free space, and κ is the chiral material parameter. The first subscript on the relative material parameters indicates the direction of the applied fields, and the second subscript indicates the direction of the material response. In the case of isotropic media these material parameters reduce even further to complex scalars.

Solving Maxwell's equations for a monochromatic plane wave propagating in the z-direction gives rise to two elliptically polarised eigenwaves in the chiral medium. The two of Maxwell's equations that are relevant here are:

$$\nabla \times \bar{\mathbf{H}} = -i\omega\bar{\mathbf{D}} \tag{2.7}$$

$$\nabla \times \bar{\mathbf{E}} = i\omega\bar{\mathbf{B}} \tag{2.8}$$

Starting from these, we can write a wave equation inside the material

$$\nabla \times \nabla \times \bar{\mathbf{E}} = i\omega \left[\bar{\bar{\mu}}_{\mathrm{r}} \mu_0 \nabla \times \bar{\mathbf{H}} + i\frac{\bar{\bar{\kappa}}}{c} \nabla \times \bar{\mathbf{E}} \right] \tag{2.9}$$

Eliminating the $\bar{\mathbf{H}}$ field from the right side of this equation we obtain the Helmholtz equation for chiral media:

$$\nabla \times \nabla \times \bar{\mathbf{E}} = \left[k_0^2 \left(\bar{\bar{\mu}}_{\mathrm{r}} \bar{\bar{\epsilon}}_{\mathrm{r}} - \bar{\bar{\kappa}}^2 \right) \bar{\mathbf{E}} - \frac{2\omega\bar{\bar{\kappa}}}{c} \nabla \times \bar{\mathbf{E}} \right] \tag{2.10}$$

From examination we see that $\nabla \cdot \bar{\mathbf{E}} = 0$, and assuming normal incidence, $\bar{\mathbf{k}} = k\hat{x}$ and $\bar{\mathbf{E}} = E_{\mathrm{y}}\hat{y} + E_{\mathrm{z}}\hat{z}$, we can write a dispersion relation

$$\left[\bar{k}^2 - \bar{k_0}^2 \left(\bar{\bar{\mu}}_{\mathrm{r}} \bar{\bar{\epsilon}}_{\mathrm{r}} - \bar{\bar{\kappa}}^2 \right) \right] \bar{\mathbf{E}} = -\frac{2ik\omega\bar{\bar{\kappa}}}{c} \hat{x} \times \bar{\mathbf{E}} \tag{2.11}$$

The two eigenvectors are

$$\bar{\mathbf{E}}_+ = \hat{y} - i\hat{z} \tag{2.12}$$

$$\bar{\mathbf{E}}_- = \hat{y} + i\hat{z} \tag{2.13}$$

so the dispersion relation becomes

$$\bar{k_\pm}^2 \mp \frac{2\bar{k_\pm}\omega\bar{\bar{\kappa}}}{c} - \bar{k_0}^2 \left(\bar{\bar{\mu}}_\mathrm{r}\bar{\bar{\epsilon}}_\mathrm{r} - \bar{\bar{\kappa}}^2\right) = 0 \tag{2.14}$$

which gives us two elliptically polarised eigenwaves:

$$\bar{k_\pm} = \bar{k_0}\left(\sqrt{\bar{\bar{\mu}}_\mathrm{r}\bar{\bar{\epsilon}}_\mathrm{r}} \pm \bar{\bar{\kappa}}\right) \tag{2.15}$$

where k_0 is the free space wave-vector of the incident radiation, the r subscript indicates that these are the relative permeability and permittivity, and the $\pm$ subscript denotes the eigenstate for RH or LH elliptically polarised waves. These waves of opposite handedness will experience different complex refractive indices, that can be written:

$$\bar{n_\pm} = \sqrt{\bar{\bar{\mu}}_\mathrm{r}\bar{\bar{\epsilon}}_\mathrm{r}} \pm \bar{\bar{\kappa}} \tag{2.16}$$

where the $\pm$ indicates refractive indices for RH (+) and LH (-) waves. The chiral material parameter is complex, just as any other material parameter. The real part describes the difference in phase velocities of oppositely handed waves, while the imaginary part describes the difference in attenuation. These two features of a chiral material lead to two signatures of its interaction with a chiral EM wave. A difference in phase velocity between circularly polarised waves will lead to a rotation of the plane of linear polarisation, termed optical rotation. A difference in attenuation will lead to a linearly polarised wave becoming elliptically polarised upon transmission

or reflection, termed ellipticity. A measure of the difference in absorption of left- and right-handed waves is circular dichroism. This is closely related to the ellipticity and the terms are often used interchangeably. The general term for this collection of chiroptical interactions is optical activity. These will be discussed in more detail in section 2.1 4.

2.1.4 Measurements of Chirality

This section is relevant to chapters 4 and 5.

Transmission and Reflection in Circular Polarisation

As mentioned previously, there are two indicators of geometrical chirality measured through interaction with chiral EM waves of opposite handedness. The starting point is therefore defining the transmission and reflection of circularly polarised waves, as derived from linearly polarised waves. This analysis is important for the experimental results presented later in this thesis, as all measurements are performed using linearly polarised waves, and later converted into coefficients of circular polarisation.

Starting from a simple scattering matrix approach, eg.

$$\text{output} = S \cdot \text{input} \tag{2.17}$$

we can write, for a general material with a finite thickness,

$$\begin{bmatrix} E^a_{R,1}\left(k_{||}\right) \\ E^b_{L,1}\left(k_{||}\right) \\ E^a_{R,2}\left(k_{||}\right) \\ E^b_{L,2}\left(k_{||}\right) \end{bmatrix} = \begin{bmatrix} t_{11} & \bar{r_{11}} & t_{12} & \bar{r_{12}} \\ r_{11} & \bar{t_{11}} & r_{12} & \bar{t_{12}} \\ t_{21} & \bar{r_{21}} & t_{22} & \bar{r_{22}} \\ r_{21} & \bar{t_{21}} & r_{22} & \bar{t_{22}} \end{bmatrix} \begin{bmatrix} E^a_{L,1}\left(k_{||}\right) \\ E^b_{R,1}\left(k_{||}\right) \\ E^a_{L,2}\left(k_{||}\right) \\ E^b_{R,2}\left(k_{||}\right) \end{bmatrix} \tag{2.18}$$

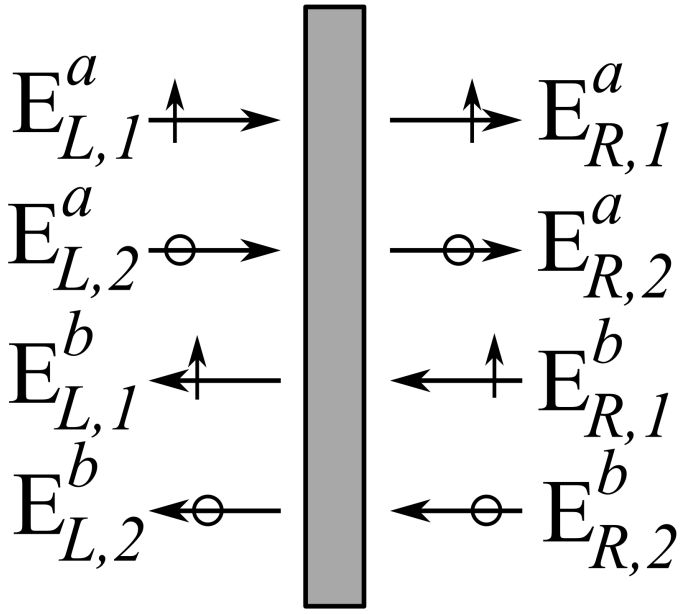

FIGURE 2.6: **Notation used in derivation of reflection and transmission coefficients for chiral medium.** The subscripts *R* and *L* indicate fields on the right and left of the medium respectively, the superscripts a and b indicate waves travelling to the right and left respectively, the subscripts 1 and 2 indicate TE and TM polarisations The subscripts R and L indicate fields on the right and left of the medium respectively, superscripts *a* and *b* indicate waves travelling to the right and left respectively, the subscripts 1 and 2 indicate TE and TM polarisations.

Figure 2.6 illustrates the notation used in the derivation. The subscripts R and L indicate fields on the right and left of the medium respectively, the superscripts *a* and *b* indicate waves travelling to the right and left respectively, the subscripts 1 and 2 indicate TE and TM polarisations, r_{ij} and t_{ij} are the reflection and transmission coefficients where the bar indicates incidence from the right rather than the left. Finally $k_{||}$ indicates the component of the wave-vector that is parallel to the surface, and depends on the angle of incidence. We can write the incident fields in the circular polarisation basis, e.g.

$$\tilde{E}^a_{\mathrm{R},+}\left(k_{||}\right) = \frac{1}{\sqrt{2}}\left[E^a_{\mathrm{R},1}\left(k_{||}\right) + iE^a_{\mathrm{R},2}\left(k_{||}\right)\right] \tag{2.19}$$

where subscript + indicates right-handed circular polarisation, and - indicates left-handed. This can be done more efficiently using the transformation matrix:

$$\begin{bmatrix} \tilde{E}^a_{\mathrm{R},+}\left(k_{||}\right) \\ \tilde{E}^b_{\mathrm{L},+}\left(k_{||}\right) \\ \tilde{E}^a_{\mathrm{R},-}\left(k_{||}\right) \\ \tilde{E}^b_{\mathrm{L},-}\left(k_{||}\right) \end{bmatrix} = \frac{1}{\sqrt{2}} \begin{bmatrix} 1 & 0 & i & 0 \\ 0 & 1 & 0 & -i \\ 1 & 0 & -i & 0 \\ 0 & 1 & 0 & i \end{bmatrix} \begin{bmatrix} E^a_{\mathrm{R},1}\left(k_{||}\right) \\ E^b_{\mathrm{L},1}\left(k_{||}\right) \\ E^a_{\mathrm{R},2}\left(k_{||}\right) \\ E^b_{\mathrm{L},2}\left(k_{||}\right) \end{bmatrix} \tag{2.20}$$

We implement this transformation in equation 2.18,

$$\begin{bmatrix} t_{++} & \bar{r_{++}} & t_{+-} & \bar{r_{+-}} \\ r_{++} & \bar{t_{++}} & r_{+-} & \bar{t_{+-}} \\ t_{-+} & \bar{r_{-+}} & t_{--} & \bar{r_{--}} \\ r_{-+} & \bar{t_{-+}} & r_{--} & \bar{t_{--}} \end{bmatrix} = \frac{1}{2} \begin{bmatrix} 1 & 0 & i & 0 \\ 0 & 1 & 0 & -i \\ 1 & 0 & -i & 0 \\ 0 & 1 & 0 & i \end{bmatrix} \begin{bmatrix} t_{11} & \bar{r_{11}} & t_{12} & \bar{r_{12}} \\ r_{11} & \bar{t_{11}} & r_{12} & \bar{t_{12}} \\ t_{21} & \bar{r_{21}} & t_{22} & \bar{r_{22}} \\ r_{21} & \bar{t_{21}} & r_{22} & \bar{t_{22}} \end{bmatrix} \begin{bmatrix} 1 & 0 & 1 & 0 \\ 0 & 1 & 0 & 1 \\ -i & 0 & i & 0 \\ 0 & i & 0 & -i \end{bmatrix} \tag{2.21}$$

Writing this in a shorthand notation

$$\begin{bmatrix} S_{++} & S_{+-} \\ S_{-+} & S_{--} \end{bmatrix} = \frac{1}{2} \begin{bmatrix} \mathbb{1}_2 & i\sigma_z \\ \mathbb{1}_2 & -i\sigma_z \end{bmatrix} \begin{bmatrix} S_{11} & S_{12} \\ S_{21} & S_{22} \end{bmatrix} \begin{bmatrix} \mathbb{1}_2 & \mathbb{1}_2 \\ i\sigma_z & i\sigma_z \end{bmatrix} \tag{2.22}$$

The reflection and transmission coefficients in the circular polarisation basis therefore transform as

$$\begin{bmatrix} S_{++} & S_{+-} \\ S_{-+} & S_{--} \end{bmatrix} = \frac{1}{2} \begin{bmatrix} S_{11} + i\left(\sigma_z S_{21} - S_{12}\sigma_z\right) + \sigma_z S_{22}\sigma_z & S_{11} - \sigma_z S_{22}\sigma_z + i\left(\sigma_z S_{21} + S_{12}\sigma_z\right) \\ S_{11} - \sigma_z S_{22}\sigma_z - i\left(\sigma_z S_{21} + S_{12}\sigma_z\right) & S_{11} - i\left(\sigma_z S_{21} - S_{12}\sigma_z\right) + \sigma_z S_{22}\sigma_z \end{bmatrix} \tag{2.23}$$

This formula can be expanded to give the circularly polarised reflection and transmission coefficients for waves incident from either side, in terms of the linear reflection and transmission coefficients.

$$\begin{bmatrix} t_{++} & r^{-}_{++} \\ r_{++} & t^{-}_{++} \end{bmatrix} = \frac{1}{2} \begin{bmatrix} t_{11} + t_{22} + i\,(t_{21} - t_{12}) & \bar{r}_{11} - \bar{r}_{22} + i\,(\bar{r}_{21} + \bar{r}_{12}) \\ r_{11} - r_{22} - i\,(r_{21} + r_{12}) & \bar{t}_{11} + \bar{t}_{22} + i\,(\bar{t}_{12} - \bar{t}_{21}) \end{bmatrix} \tag{2.24}$$

$$\begin{bmatrix} t_{--} & r^{-}_{--} \\ r_{--} & t^{-}_{--} \end{bmatrix} = \frac{1}{2} \begin{bmatrix} t_{11} + t_{22} - i\,(t_{21} - t_{12}) & \bar{r}_{11} - \bar{r}_{22} - i\,(\bar{r}_{21} + \bar{r}_{12}) \\ r_{11} - r_{22} + i\,(r_{21} + r_{12}) & \bar{t}_{11} + \bar{t}_{22} - i\,(\bar{t}_{12} - \bar{t}_{21}) \end{bmatrix} \tag{2.25}$$

$$\begin{bmatrix} t_{+-} & r^{-}_{+-} \\ r_{+-} & t^{-}_{+-} \end{bmatrix} = \frac{1}{2} \begin{bmatrix} t_{11} - t_{22} + i\,(t_{21} + t_{12}) & \bar{r}_{11} + \bar{r}_{22} + i\,(\bar{r}_{21} - \bar{r}_{12}) \\ r_{11} + r_{22} + i\,(r_{12} - r_{21}) & \bar{t}_{11} - \bar{t}_{22} - i\,(\bar{t}_{21} + \bar{t}_{12}) \end{bmatrix} \tag{2.26}$$

$$\begin{bmatrix} t_{-+} & r^{-}_{-+} \\ r_{-+} & t^{-}_{-+} \end{bmatrix} = \frac{1}{2} \begin{bmatrix} t_{11} - t_{22} - i\,(t_{21} + t_{12}) & \bar{r}_{11} + \bar{r}_{22} - i\,(\bar{r}_{21} - \bar{r}_{12}) \\ r_{11} + r_{22} - i\,(r_{12} - r_{21}) & \bar{t}_{11} - \bar{t}_{22} + i\,(\bar{t}_{21} + \bar{t}_{12}) \end{bmatrix} \tag{2.27}$$

The intensities of transmitted and reflected waves are calculated as the squares of the absolute values of the reflection and transmission coefficients given above. For example, the transmission of circularly polarised waves is widely used throughout this thesis:

$$T_{++} = |t_{++}|^2 \tag{2.28}$$

$$T_{--} = |t_{--}|^2 \tag{2.29}$$

$$T_{+-} = |t_{+-}|^2 \tag{2.30}$$

$$T_{-+} = |t_{-+}|^2 \tag{2.31}$$

Circular Dichroism and Optical Rotation

Now that we can calculate the transmission of a wave in terms of circular polarisations, we can use these to characterise the chirality of the systems under study. As mentioned in section 2.1.3, chiral media have different refractive indices for circularly polarised waves of opposite handedness (according to equation 2.16).

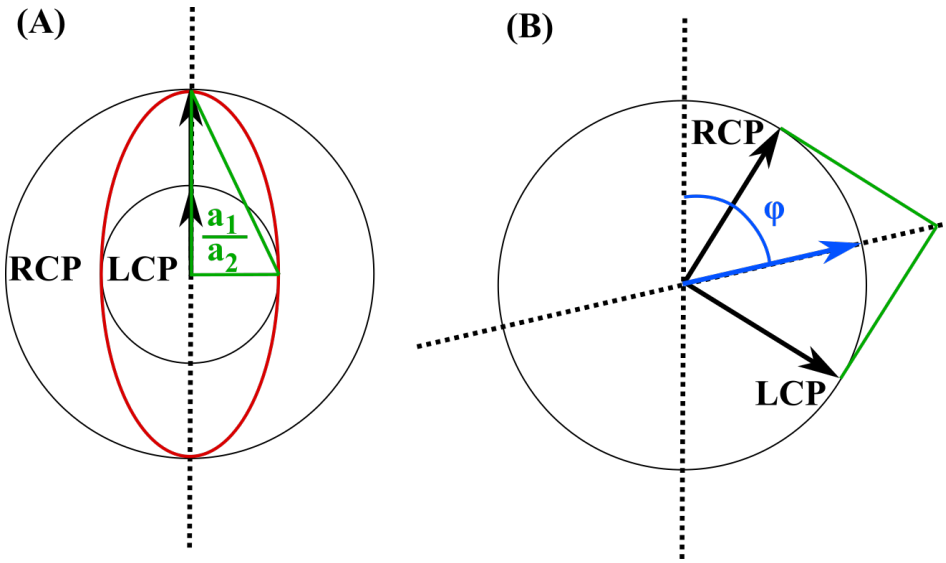

FIGURE 2.7: **Visual representation of (A) circular dichroism (CD) and (B) optical rotation (OR)**. The intensities of right- and left-circularly polarised (RCP, LCP) waves are represented by black circles, and their electric field at a certain point in phase represented by black arrows. The dotted black lines are for reference. In **(A)** the intensities of RCP and LCP waves are different, while the phases are the same, leading to an elliptically polarised wave defined by the ratio between the major and minor axes of the red ellipse. In **(B)** the intensities are equal but there is a phase shift between RCP and LCP waves, leading to a linearly polarised but rotated wave defined by the angle ϕ and represented by the blue arrow.

Circular dichroism (CD) arises from a difference in attenuation of oppositely handed circularly polarised (CP) waves. It is dependent on the imaginary part of the chiral material parameter. It is defined by the ellipticity, θ, of an output wave, as

illustrated in figure 2.7 (A). The vertical dotted line represents the linear polarisation of an incident wave, which can be broken down into two CP waves of equal intensity, represented by the black circles and matched phase, shown by the black arrows. Upon travelling through a chiral medium one CP wave experiences a higher attenuation than the other, and its intensity decreases. The resultant wave is generally elliptically polarised, represented by the red ellipse.

Often in chemistry and biology the CD is reported in units of degrees, representing the angle formed between the major and minor axes of the ellipse [22]. However, throughout this thesis the CD will be reported as the difference in transmitted intensities of RH and LH waves, with ± 1 representing RH/LH CP waves, and 0 representing linearly polarised waves. We calculate the value as

$$\theta = \frac{|T_{++}|^2 - |T_{--}|^2}{|T_{++}|^2 + |T_{--}|^2}. \tag{2.32}$$

Optical rotation (OR), or circular birefringence, arises from a difference in phase of oppositely handed circularly polarised waves, and is associated with the real part of the chiral material parameter. This effect is illustrated in figure 2.7 (B), where the RH and LH components of the incident wave emerge from the chiral material with different relative phases. This leads to a rotation of the plane of polarisation of the linearly polarised wave. This optical rotation, ϕ is defined as the angle through which the wave has rotated, and is calculated as

$$\phi = \frac{\arg(T_{++}) - \arg(T_{--})}{2}. \tag{2.33}$$

It is important to note that, for a chiral system with C_4 rotational symmetry (one which has four-fold rotational symmetry), the intensity of waves with converted circular polarisation, ie. T_{+-} and T_{-+} will be zero. This can be deduced by considering a circularly polarised wave incident on a linear polariser, where circular polarisation conversion is present in an achiral system. Therefore, when we are looking

for a measure of the chirality of the system, and not the anisotropy, these terms are ignored in calculations of CD and OR.

As well as linear birefringence in anisotropic media, and extrinsic chirality [21] as discussed in section 2.1.2, optical activity has also been shown to arise in higher diffracted orders [23], and even in disordered arrays of achiral sub-wavelength particles [24].

Kramers-Kronig Relations in Chiral Media

In general, chiral materials will have a frequency-dependent, complex chiral material parameter, and circular dichroism and optical rotation will occur simultaneously. In fact, these two phenomena are linked by the Kramers-Kronig (KK) relation [25], that can be written as:

$$[\phi(\omega)] = \frac{2}{\pi} PV \int_0^\infty \frac{\omega' [\theta(\omega')]}{\omega'^2 - \omega} d\omega' \tag{2.34}$$

$$[\theta(\omega)] = \frac{2\omega}{\pi} PV \int_0^\infty \frac{[\phi(\omega')]}{\omega'^2 - \omega} d\omega' \tag{2.35}$$

where ω is the frequency of the incident wave, ω' is the resonant frequency and PV indicates that the Cauchy principle value of the integral should be used, as the integral includes a singularity.

For simple systems, these equations indicate that the CD for a system can be derived if we know the OR, or vice versa. We can conclude that a peak in one of the values should be accompanied by a discontinuity in the gradient (kink) in the other, and that is true for most naturally occurring chiral materials. This bisignate nature of optical activity is known as the Cotton effect [26]. However the CD and OR spectra of many artificial chiral materials seem to contradict these laws, and regions of large OR can be accompanied by negligible CD (see chapter 4). When zeros in the transmission occur due to strong resonances in artificial chiral materials, the

standard form of the KK relations is no longer applicable. Considering the result of causality on the logarithm of the reflection or transmission coefficients leads to the presence of the Blaschke term [27, 28]. This term is needed to adjust the phase of the transmission and reflection coefficients when there are zeros present, and so only affects the OR according to

$$[\phi(\omega_{UC})] = [\phi(\omega)] + [\phi(\omega_B)], \tag{2.36}$$

where $\phi(\omega_B)$ is the difference in the sum of phase accumulated for each zero in the transmission of RH and LH transmission.

Both CD and OR are frequency dependent, and change sign multiple times across the frequency spectrum. Often, these sign changes occur one after the other leading to a bisignate signal. This becomes clear when we consider Kuhn's sum rule [29], that states that the value of optical activity integrated over all frequencies must be zero.

Kuhn first interpreted this rule by considering a driven mechanical system of two coupled, linear, perpendicular oscillators placed one on top of the other. Later the same principles were applied to plasmonic resonators [29–31]. A schematic showing an example of plasmonic dipoles is in figure 2.8. It was found throughout that two resonant modes can occur at different energies referred to as bonding/symmetric or antibonding/antisymmetric. The difference between these modes is the 2π radians difference in relative phase of the resonators. This leads to an opposite sign of optical activity for each mode, and a bisignate kink in the spectra. The same principles can be extended to any number of coupled resonators.

An alternative interpretation for chiral spectra is found by considering a single electron excited by a circularly polarised EM wave[22]. If the electron is present in a symmetric environment, such as a metallic sphere, it will travel along a helical

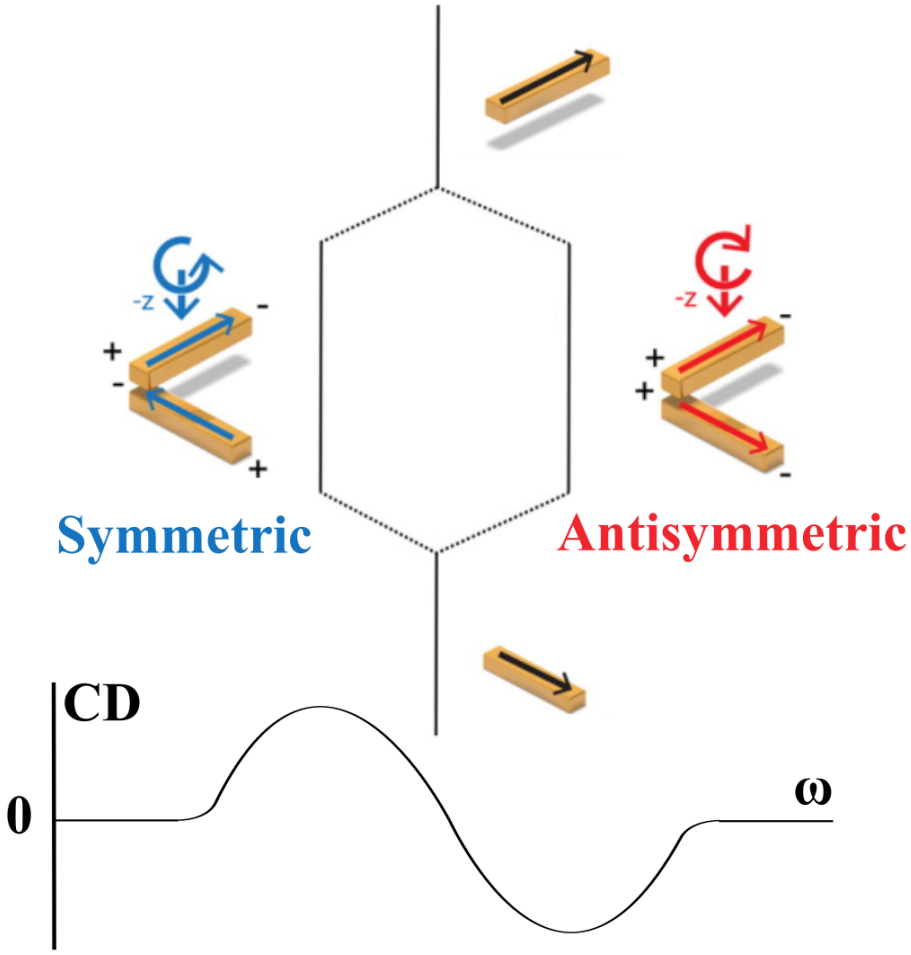

FIGURE 2.8: **Bisignate nature of circular dichroism (CD).** The resonant modes of individual rods displaced in height with different orientations, with dipoles represented by black arrows, exist at the same energy. However when two rods are arranged next to each other, the modes split into a higher energy (red) mode and a lower energy (blue) mode, defined as symmetric and antisymmetric with respect to the currents flowing in the lower rod at the illustrated point in phase. These two modes have different chiralities, as made clear by considering the handedness of wave needed to excite the different modes (the arrows above the rods). This leads to a change in sign of the CD spectrum with frequency, and the typical bisignate pattern. Adapted from [29]

path determined by the handedness of the incident wave. If the electron however is present along a helical wire, its movement will depend on whether the incident wave is of the same or opposite handedness to the helix, leading to a chiroptical signal.

Transitions in Chiral Molecules

The quantity C that defines the chirality of an EM field is closely related to the condition needed for optical activity in molecules. In a chiral transition overlapping electric and magnetic dipole moments, among others, are excited simultaneously [14]. The rotational strength of a transition from state n to state j is

$$R\left(j \leftarrow n\right) = \mathbb{I}\left(\langle n|\boldsymbol{\mu}|j\rangle \cdot \langle j|\mathbf{m}|n\rangle\right) \tag{2.37}$$

This can be used to derive the dissymmetry factor, g, which describes the ratio of circular dichroism to absorption, and is commonly used to report the strength of a molecular chiral interaction. For an isotropic sample, averaged over all orientations it is:

$$g\left(j \leftarrow n\right) = \frac{4R\left(j \leftarrow n\right)}{cD\left(j \leftarrow n\right)} \tag{2.38}$$

where D is the dipole strength of the transition:

$$D\left(j \leftarrow n\right) = \mathbb{R}\left(\langle n|\boldsymbol{\mu}|j\rangle \cdot \langle j|\boldsymbol{\mu}|n\rangle\right) \tag{2.39}$$

In the next section, higher-order transitions in chiral molecules will be studied as a possible route to enhanced chiral interactions.

2.1.5 Enhanced Chirality

The ideas presented here are of particular relevance to chapter 5.

It was long assumed that the maximum strength of a chiral interaction between EM radiation and a molecule was achieved with a monochromatic circularly polarised plane wave. However, recent work reporting enhanced chiral interactions has attracted a lot of attention, and the possibility remains a hotly debated topic. Chapter 5 of this thesis aims to address some of the issues surrounding "superchirality".

Harnessing a way to enhance the interaction between a chiral molecule and an EM field would have profound implications for the pharmaceutical industry, as well as in food and perfume production. Therefore a lot of the work in this field has been carried out at the nanoscale, using plasmonic particles and biomolecules.

The main justification given for observing these enhanced effects is usually that in these systems the paraxial approximation is not valid and we can no longer assume that chiral scatterers are infinitely small dipoles compared to the wavelength of excitation. Under these conditions the angular momentum of EM near-fields cannot be easily separated into spin (rotation of the electric and magnetic fields) and orbital (radial dependence to the phase fronts) components. The situation becomes a lot more complicated, and many of the theoretical models available today do not capture the whole picture. A range of experimental work has been performed, occasionally reporting contradictory findings, and an intuitive understanding of the route to enhanced chiral interactions is yet to be achieved.

Higher-Order Terms in Chiroptical Interactions

The groundwork set out for the study of light scattering from chiral molecules is found in the work of Barron [14]. His description of such an interaction follows that of equation 2.38, until the molecules are no longer significantly smaller than the wavelength or randomly oriented. At this point higher-order transitions in

molecules begin to play a role, notably the electric quadrupole transition becomes important [32]. For an ensemble of oriented molecules the rotational and dipole transition strengths must be generalised to

$$R_z\left(j \leftarrow n\right) = -\{\frac{1}{3}\omega_j n\left[\mathbb{R}\left(\langle n|\mu_x|j\rangle\langle j|\Theta_{yz}|n\rangle\right) - \mathbb{R}\left(\langle n|\mu_y|j\rangle\langle j|\Theta_{xz}|n\rangle\right)\right] - \mathbb{I}\left(\langle n|\mu_x|j\rangle\langle j|m_x|n\rangle\right) - \mathbb{I}\left(\langle n|\mu_y|j\rangle\langle j|m_y|n\rangle\right)\} \tag{2.40}$$

$$D_z\left(j \leftarrow n\right) = \mathbb{R}\left(\langle n|\mu_x|j\rangle\langle j|\mu_x|n\rangle\right) + \mathbb{R}\left(\langle n|\mu_y|j\rangle\langle j|\mu_y|n\rangle\right) \tag{2.41}$$

for an incident field along z, and where Θ is the strength of the electric quadrupole moment orientated along the directions indicated in the subscript. The electric quadrupole moment only contributes to the optical activity of the sample when the molecules are oriented or they themselves are large enough to extend over a significant portion of the wavelength, and in a random array of small molecules this effect will cancel [32]. In addition, when discussing optical activity from a crystalline structure with D_3 symmetry (the symmetry group of an equilateral triangle), the electric quadrupole contributions must be taken into account. The situation is complicated further, as in general, contributions from either $(\mu \cdot m)$ or $(\mu \cdot \Theta)$ interactions cannot be distinguished.

This contribution to chirality from higher order transitions (there are also contributions from magnetic quadrupoles, octupoles, but the effect decreases further with increasing order and these are usually ignored) spurred progress in research subjecting fairly large molecules (around 5 nm) to EM fields with high wave-vector components, in an attempt to induce a stronger electric quadrupole moment and enhance the chiral signal [33].

Enhancing the Chirality of a Field

The first work that reported an enhanced chiral interaction was that of Tang and Cohen, proposed in 2010 [12] and experimentally shown in 2011 [34]. In this work they did not include any contributions from electric quadrupole transitions in their calculations, as they were concerned with isotropic ensembles of molecules. Instead they focussed on enhancing the chirality of the EM field.

According to equation 2.2, a circularly polarised plane wave has a chirality of $C_{\mathrm{CP}} = \pm\omega\epsilon_0|E_0|^2/2c$, where ω is the angular frequency of the incident wave, ϵ_0 is the permittivity of free space, $|E_0|^2$ is the electric field intensity and c is the speed of light in vacuum. However it is possible to generate an evanescently decaying EM field with a value of C exceeding that of a plane wave. It can be thought of as a field that rotates through 2π radians in less than one wavelength. This kind of field is termed "superchiral".

This definition of a chiral EM field can be used to write a dissymmetry factor, g, similar to that in equation 2.38 but generalised to any incident EM field, that describes the difference in the rate of excitation of a molecule under RH and LH CP illumination.

$$g = -\left(\frac{G''}{\alpha''}\right)\left(\frac{2C}{\omega U_e}\right) \tag{2.42}$$

where G'' and α'' are the imaginary parts of the complex electric polarisability and mixed electric-magnetic polarisability, C is the chirality of the incident field as in equation 2.2, ω is the incident frequency and $U_e = \frac{\epsilon_0}{4}|\tilde{\mathbf{E}}|^2$ is the time averaged electric energy density. Note here that the magnetic polarisability of a molecule is ignored, as it is said to be small enough to be negligible. This gives a dissymmetry factor that is proportional to both the chirality of the molecule and the EM field, although these two contributions are not as easily separated as it seems here. It followed that increasing C would lead to an increase in the dissymmetry and a increase

in our ability to characterise chiral molecules.

The first experiment performed in this vein placed fluorescent chiral molecules in the nodes of a chiral standing wave, and measured an enhanced value of g in the emission [34]. However this enhancement is explained through the decreased electric energy density at the nodes of a standing wave, leading to a decrease in the ratio between chiral and achiral response [35]. As the electric energy decreases, the magnetic energy density, U_m, increases proportionally, and can no longer be considered negligibly small. The dissymmetry factor should then be written as [36]

$$g = -\left(\frac{G''}{\alpha''}\right)\left(\frac{2C}{\omega\left[U_e + \gamma U_m\right]}\right). \tag{2.43}$$

Decreasing the electric field to arbitrarily small values no longer leads to arbitrarily high dissymmetry, and the coefficient γ now sets the limit to the chiral interaction.

Despite this, much work has been performed looking at enhanced or superchiral fields (some examples are shown later in figure 2.11). One of the most simple configurations in which enhanced chirality has been reported is in surface plasmon polaritons on a flat metal sheet, excited by a chiral dipole [37]. Surface plasmon polaritons are the bound surface waves at the interface between a Drude-like metal and dielectric [38]. Finite element modelling showed that the enhancement in chirality extended over a range much outside that of the dipole itself. Superchiral fields can also be excited in non-chiral nano-structures [15, 39] due to the interaction of scattered and incident fields. Exciting chiral nano-particles with circularly polarised light allows control over the excitation of fields with enhanced local chirality [40], and such control has been used to tune the optical properties of a metasurface [41] and a cluster of nanoparticles [42].

While there is no doubt over the existence of EM fields with a value of $C > C_{\mathrm{CP}}$, the consequences for far-field measurements and interactions with molecules is yet to be fully understood. Furthermore, a lack of solid theoretical explanation for the

observed effects also inspired many theorists to tackle the issue.

Zilches, Helicity and Momenta

There is a question mark over the validity of using Lipkin's zilch as a measure of the chirality of the field. This represents the angular momentum of the curl of a field, rather than the field itself, and does not have units of angular momentum as we would expect. A more physically meaningful value is found in Noether's infra-zilches, N^{ijk} [43]. These infra-zilches exist as a set of six conserved quantities that describe the angular momentum associated with the polarisation of a wave. They are time-even, have units of angular momentum, change sign under a parity inversion, and so seem to satisfy all the conditions we need for a measure of the chirality of a field. The first of these is in fact the helicity of the wave, which is proportional to the spin of a photon, $\hbar\sigma$, but not the same physical quantity.

However Lipkin's and Noether's zilches are linked. For a monochromatic plane wave in vacuum, the first Lipkin's zilch and Noether's infra-zilch are proportional [43], which may explain why comparing experimental results to those predicted by theory was often successful. When considering circularly polarised waves in a dispersive medium Lipkin's zilch acquires a factor of the square of the refractive index, whereas the helicity becomes inversely proportional to the refractive index [44]. The spin angular momentum (SAM) is not dependent on the refractive index at all, so while these properties are related, their behaviour in media can be quite different. Assuming that chiral interactions are mediated only by the helicity of the field leads to limitations on the strength of a chiral interaction. This upper limit is reached when an object is totally transparent to fields of one helicity and scatters fields of the opposite helicity [45]. In scattering the fields, some may be converted into the opposite handedness, unless the object is reciprocal (dual symmetric) and maximally chiral.

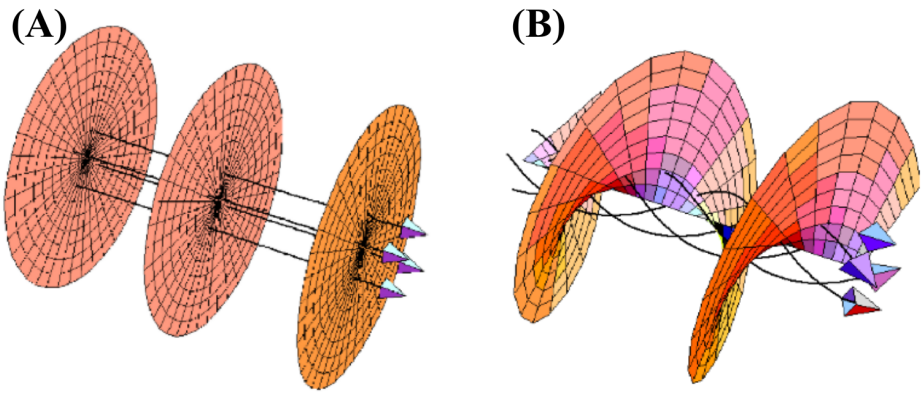

FIGURE 2.9: **Light with orbital angular momentum.** If a wave is circularly polarised, i.e. it has spin angular momentum, the electric field will spiral around the beam axis, but the phase fronts (orange planes) will be planar and perpendicular to the wave-vector (arrows) that point along the beam axis, as in **(A)**. The wave in **(B)** has orbital angular momentum with $l = 1$, so the phase fronts and wave-vector spiral around the beam axis. Reproduced from [46]

The SAM describes the rotation of electric and magnetic fields in a circularly polarised beam. It is a vector oriented along the propagation direction, and has values of ± 1. SAM is one type of angular momentum carried by a beam, the other being the orbital angular momentum (OAM), which is also aligned with the SAM and propagation. A beam will have an OAM of order $l = 0, \pm 1, \pm 2...$ if its wave-fronts have an azimuthal phase dependence of $e^{il\phi}$ where ϕ is the azimuth angle perpendicular to the direction of propagation, as illustrated in figure 2.9 (B) [46]. In a paraxial beam the SAM and OAM components of orbital angular momentum are separate and independent. However in non-paraxial fields composed of the superposition of many plane waves, OAM and SAM interact and become impossible to distinguish [47]. While not investigated in this thesis, there have been reports claiming that OAM may contribute to chiral interactions [48, 49], and recently a theoretical investigation was performed into the origins of this effect for aligned chiral molecules [50]. Manipulating the orbital angular momentum of a field could lead to new methods for the detection of chirality.

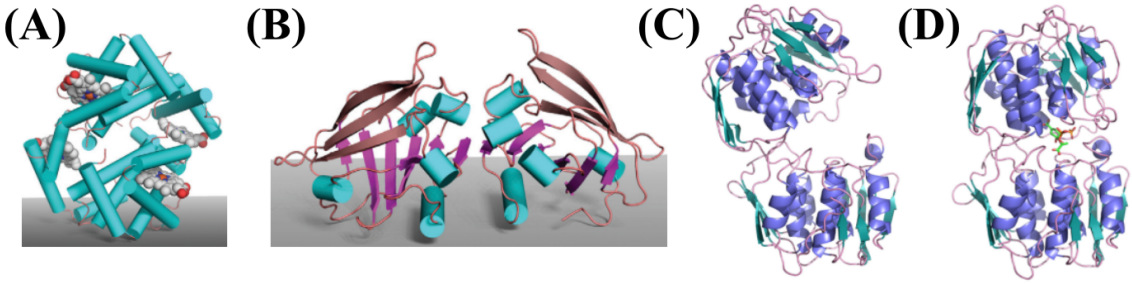

FIGURE 2.10: **Examples of chiral molecules that have been detected using enhanced chiral fields. (A)** is haemoglobin, which has a high proportion of α-helices (cyan cylinders). **(B)** shows two molecules of β-lactoglobulin, which have some α-helices and many more β-twisted sheets (purple arrows). The diagram also shows their tendency to align on a substrate, not not seen in the haemoglobin. **(C)** and **(D)** are diagrams of 5- enolpyruvylshikimate 3-phosphate synthase without and with ligands which alter their quaternary structures. In these α-helices are represented by purple helices and β-twisted sheets are cyan arrows. Reproduced from [33] and [52]

Enhanced Chiral Sensing

One of the most interesting applications of enhanced chiral fields is their potential ability to detect very small amounts of chiral molecules, which would be a huge benefit to the pharmaceutical, food and perfume industries. The problems with detection arise because most chiral transitions in molecules occur in the ultra-violet (UV) part of the spectrum [51]. Using an intense UV source to detect molecules runs the risk of denaturing the proteins and leading to an incorrect measurement. Hence most measurements are carried out at visible or infra-red (IR) frequencies, where the circular dichroism signals are small, and high concentrations of the molecules are needed.

By placing chiral molecules in the vicinity of chiral plasmonic structures that are resonant at IR frequencies, it was proposed that the superchiral field would increase the sensitivity of detection [33]. Another method used counter-propagating waves of opposite handedness [34], as discussed in earlier in this section.

Plasmonic effects have been used widely in techniques such as surface-enhanced

Raman spectroscopy (SERS) to improve the detection of molecules adsorbed on a surface [53, 54]. Such effects increase Raman scattering cross-sections by typically 10^4 - 10^6, and are due to a combination of two mechanisms. The first is due to the excitation of surface plasmons in the nano-structured metallic substrate, and the second is due to the increase in polarisability of the molecule. The intensity of Raman scattering is proportional to the square of the dipole moment induced in the molecule. This is proportional to the product of the Raman polarisability of the molecule, and the magnitude of the incident EM field, E. Localised surface plasmon resonances (LSPR) typically increase the magnitude of the electric field by a factor 10 in a local region of space, so for molecules oriented perpendicular to the surface, an enhancement of 10^4 in the scattering cross-section is predicted. This increase is also dependent on the polarisation and symmetry of the structured surface [55]. The additional 10^2 increase was put down to changes in the electronic structure of the molecule when close to a metal surface, where the molecules gain new resonant intermediate states [56].

These effects on their own will lead to an enhancement in the overall magnitudes of signals detected from chiral molecules, but at first glance they do not discriminate between right- and left-handed molecules, and therefore cannot explain an increase in circular dichroism (or other observed signature of chirality). Still, many papers have reported an enhancement in chiral molecule detection in the vicinity of super-chiral fields.

The first of these [33] studied the shift in the peak of the circular dichroism spectra of gammadion-shaped plasmonic nanoparticles (figure 2.11 (B)) in the presence of chiral molecules. It was found that this shift was in opposite directions in the presence of molecules of opposite handedness, and had a magnitude dependent on the kind of chiral structures present in the molecules, i.e. α-helices or β-twisted

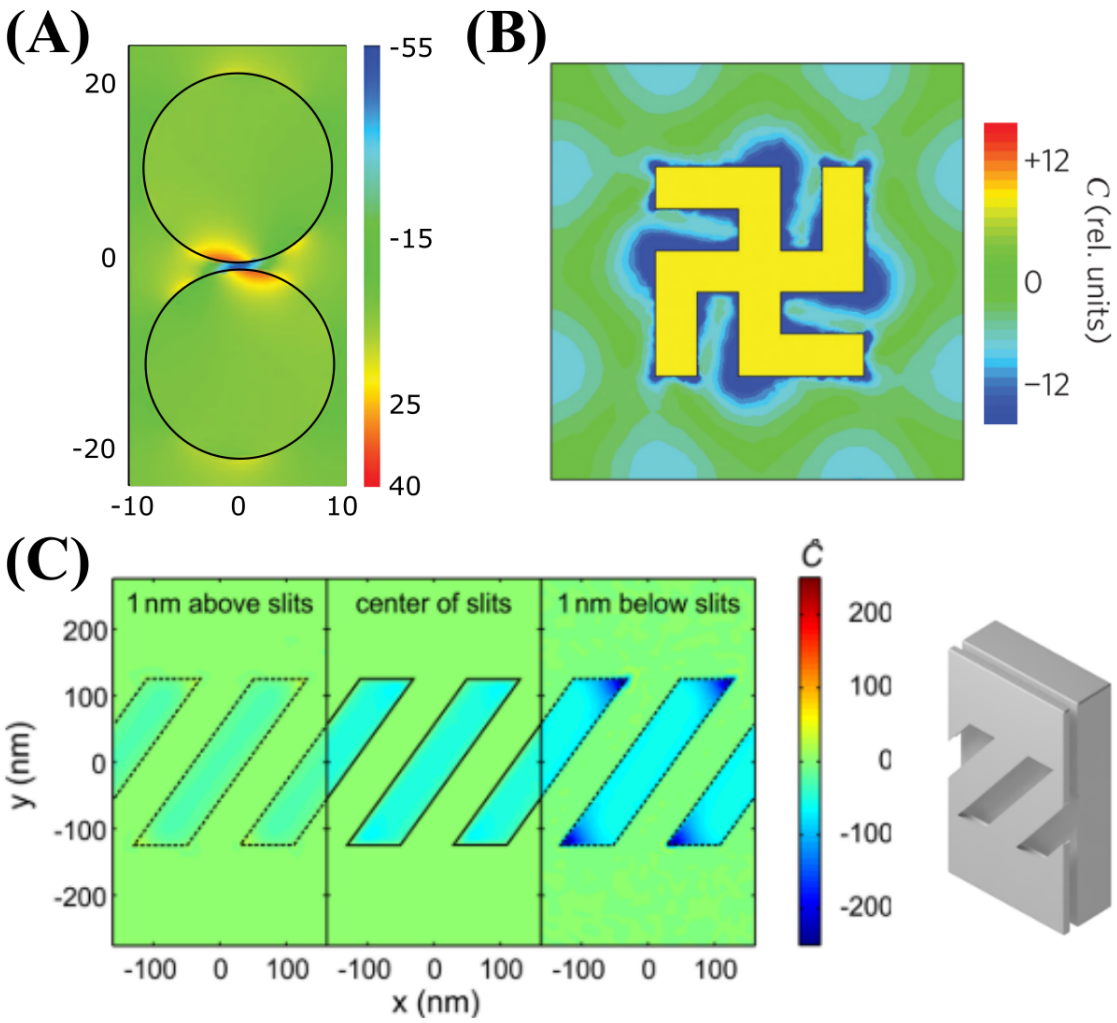

FIGURE 2.11: **Examples of chiral fields around plasmonic structures.** **(A)** shows the chirality of fields between two achiral silver spheres (black circles) excited with left-circularly polarised (LCP) light at a wavelength of 400 nm. The scale of the dimension is in nm. **(B)** is a plot of the chirality of fields around a planar-chiral gold gammadion of width 400 nm, excited with LCP light at a wavelength of around 760 nm. **(C)** shows the chirality of fields in different planes of a 3-dimensional chiral nano-structure (shown to the right), illuminated with vertically polarised light at a wavelength of 613.4 nm. Reproduced from [33, 57, 58]

sheets. Using this handedness-dependent shift as an indicator of molecular chirality led to a detection enhancement of 10^6 over traditional CD spectroscopy. The results suggested that a requirement for enhancement is large proportion of β-twisted sheets in the proteins that could lead to preferential alignment of the molecules on the substrate, such as those shown in figure 2.10 (B). Since aligned molecules will be sensitive to higher-order chiral interactions, this was evidence for the contribution.

Since then, other studies have been carried out looking at chiral molecules in chiral fields around plasmonic structures, showing detection of attomolar [59] and picogram [52] concentrations of chiral molecules. Through numerical and theoretical studies it has been suggested that there are many factors that may contribute to chiral molecule-nanoparticle interactions. Notably in the dipole approximation, where uniformly arranged molecules experience a constant electric field, there is no change in the plasmon or molecular resonances [60, 61], suggesting that non-uniform arrangements of molecules or more complex surface plasmons are needed.

Quadrupolar resonances of shuriken nanostructures have been used to probe the tertiary (overall folding of protein structures) and quaternary (arrangement of several protein chains) structure, beyond the detection of secondary structural elements (α-helices and β-twisted sheets) usually reported [52]. Examples of the molecule structures studied are shown in figure 2.10 (C) and (D). This work highlights again the influence of molecule alignment on the measured chiral signals.

A study of planar chiral nano-antennas with achiral fluorescent molecules placed on one side was conducted to probe the mechanism behind these results [62]. Studying the emission of the combined system with light incident from both faces, while the molecules remained on the same face, a change in handedness of the measured fluorescence was observed. This suggests that the presence of a chiral nano-antenna does not induce chirality in the emission from the molecule, but instead the nano-antennas split the fluorescence into LH and RH circularly polarised components on opposite faces.

A simplified version of a helical cavity (figure 2.11 (C)) was studied numerically and found to increase chiral signatures by a factor of 3 for an effective chiral medium, which suggests that some enhancement can be gained in the presence of chiral fields without the need for aligned and large molecules [58]. However this system differs to those of molecules placed on arrays, as the distribution of chiral media is not uniform and experiences only the fields in the centre of the helix. This technique is also interesting as it uses a reflection geometry, which is not possible in traditional CD spectroscopy due to the change in handedness of a wave upon reflection from a mirror.

Work has also been performed on sensing using achiral nano-structures. Strong chiral fields exist between silver or gold nano-spheres when excited with circularly polarised light (figure 2.11 (A)), and it was implied that the amplification of CD signals was proportional to the chirality of the fields rather than the intensity of the electric field [57, 63]. A similar study has also been performed using twisted stacks of nanoparticles, and the effect was found to be highly dependent on the nanoparticle spacing and not fully explained by molecule-induced chirality in the nanoparticles [64]. The importance of molecule placement in these structures has also been examined [65], and their limited suitability for practical applications highlighted.

Although all of these, and many more, report enhanced detection of chiral molecules, the importance of the chirality of the fields is not clear in any. Indeed, there have been many works that report similar enhancements in detection due to weakly chiral [66] or achiral fields. A numerical study on sensing chiral media using a plasmonic hole array concluded that the increase in detection sensitivity is mostly due to plasmonic enhancement of the near-fields, as there was no benefit to placing molecules in a chiral hole array over an achiral hole array [67]. Chiral currents induced in near-by plasmonic particles have been suggested as a mechanism behind such observations [30], supported by studies of the dependence on distance between molecule and nanoparticle [68].

In another numerical study, using only a homogeneous chiral medium placed in the hotspots of an array of nanoparticles, it was found that rods arranged in achiral patterns provided a *larger* CD enhancement than those in a chiral pattern [69]. This was explained by a change in the intensity and alignment of the electric field with respect to the chiral molecules, although the interactions between the rods themselves are also affected by changes in relative orientation.

The explicit relation between CD signal and molecule arrangement has been studied numerically [70]. It was found that different orientations of molecules with respect to plasmonic rods could give rise to different signs of CD signals, and for all molecules aligned in one direction the total magnitude of CD could be 10^6 times higher than that for randomly oriented molecules. This work also highlighted the effect of including an electric quadrupole moment to the molecules, which may increase, decrease or change the sign of CD for aligned molecules, but does not contribute to the CD of random molecules. An experimental study of molecular alignment on CD enhancement also found an order of magnitude decrease upon misaligning molecules on the surface of a plasmonic cube [71].

The origins of the enhanced strength of chiral interactions in "superchiral" fields is yet to be fully understood, but with the progress of research in this field and the flux of new results, questions are being continually answered.

2.2 Metamaterials

2.2.1 Definition of a Metamaterial

The background in this section is relevant to all chapters.

Metamaterials, as the name implies [72], offer a route to wave manipulation beyond what is possible with naturally occurring materials. They are structures comprised

of significantly subwavelength parts, or meta-atoms, where the properties of the structure are determined by the shape and arrangement of these meta-atoms, and are beyond those of the constituent materials. This definition can also be expanded to include structures on the scale of the incident wavelength, such as diffraction gratings and surfaces that support surface plasmons.

There are a range of properties that can be tuned thanks to metamaterial structure, beyond the refractive index. The permittivity and permeability can be manipulated individually, with the well-known split-ring resonator (SRR) being used to introduce artificial magnetism in a metamaterial [73]. These properties have been pushed to extremes, with long metallic wires supporting low frequency plasmons thanks to their effective negative permittivity. The combination of SRRs and long wires allowed the first negatively refracting metamaterial to be created [74]. These phenomena are often associated with the resonances of the meta-atoms, and so only exist in a narrow frequency range by nature.

This kind of control over wave propagation through a material has many applications, from super-resolution imaging [75], invisibility cloaks [76], illusion optics [77] and topologically protected waves [78]. As the definition and operating principle demands that the length scales associated with the metamaterial structure must be subwavelength, the microwave range of the electromagnetic spectrum has seen the most experimental work. However with advances in fabrication technologies, increasingly more devices are being made and studied in the Terahetz, infrared and even optical regimes.

2.2.2 Chiral Metamaterials

The information in this section is relevant to all chapters.

In addition to manipulating the permittivity and permeability, a metamaterial can

also be designed to have a chiral material parameter. This is often achieved by creating a twist in the meta-atoms, or arranging them in a twisted pattern. As discussed in sections 2.1.3 and 2.1.4, a chiral material or metamaterial will exhibit circular dichroism and optical rotation, and are therefore incredibly useful for the manipulation of the polarisation state of waves.

The first example is probably that of Lindman's work in 1920 on rotating the polarisation of light using an array of helical resonators [79]. Since then, chiral metamaterials have been studied both mathematically and experimentally. Pendry suggested chirality as an alternative route to creating a negatively refracting metamaterial, although only for waves of one circular polarisation [80]. Recently some metamaterials that are chiral have been shown to support topologically protected surface waves that are immune to back-scattering from sharp corners, due to non-trivial surface states that join energy bands with opposite chirality [78].

2.2.3 Chiral Metasurfaces

This section is relevant to all chapters.

Similar to metamaterials, metasurfaces are 2-dimensional (or of extremely subwavelength thickness) surfaces with properties dictated by their structure. Broadly, they fall into two main categories, those for controlling transmitted or reflected waves (radiative), and those for controlling waves bound to the surface (non-radiative).

The relative ease of fabrication, compared to 3-dimensional structures, means that a multitude of chiral metasurfaces have been studied. The symmetry of the array can be broken through either creating elements that are themselves chiral in 3-dimensions (eg. helices [81]) or 2-dimensions (eg. spirals and gammadions [82, 83]). Alternatively achiral elements such as crosses or split-ring resonators can be arranged to create a chiral structure through coupling [84, 85]. These two approaches

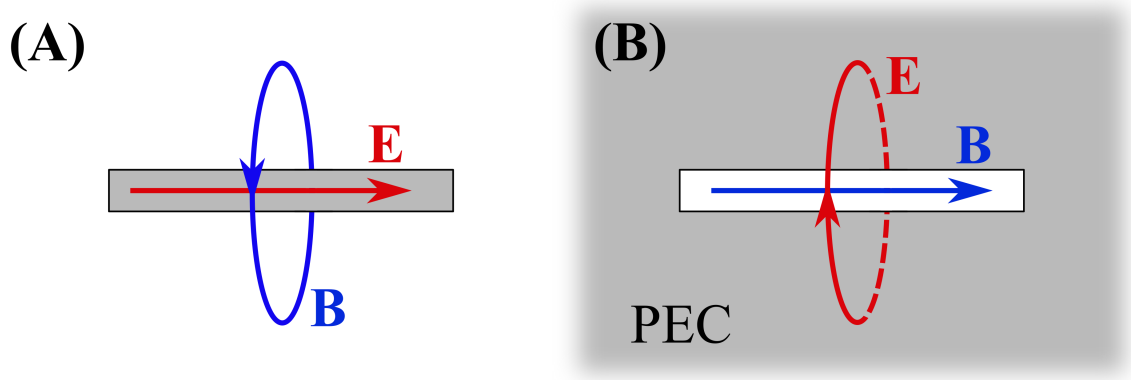

FIGURE 2.12: **Illustration of Babinet's principle.** The metallic rod (solid structure) in **(A)** has electric field (E, red arrow) pointing along the rod axis, and the current flowing in the same direction creates a loop of magnetic field (B, blue arrow) around the rod. In **(B)** the rod has been converted to a rod-shaped hole (complementary structure) in a metallic sheet, and the E and B fields swapped with a π phase change induced in the E field.

can be combined by stacking or arranging 2-dimensional chiral elements in chiral patterns [86].

Additionally, the combination of solid and complementary structures can be used, according to Babinet's principle [87]. This principle relates the scattered fields of a solid object to those of the complementary object via satisfying the condition:

$$(E^{c}_{in}, H^{c}_{in}) = (\pm Z_0 H^{s}_{in}, \mp E^{s}_{in}/Z_0) \tag{2.44}$$

where Z_0 is the impedance of free space, E_{in} and H_{in} are the incident electric and magnetic fields, and the superscripts c and s signify the case for the complementary and solid scatterer. In other words, the polarisation of electric and magnetic fields rotate by $\pi/2$ radians upon changing from a complementary to a solid scatterer, [88, 89].

Radiative

Metasurfaces may be designed to manipulate EM waves that are reflected from them or transmitted through. These are radiative metasurfaces, and control the far-field properties of plane waves. Examples convert linear to circular polarisation (CP) upon transmission [90], provide asymmetric transmission of CP waves [91, 92] and convert CP waves from one handedness to the other [18], even with dynamic switching between handedness [89]. These effects tend to be highly dispersive, as they are limited by the Kramers-Kronig relations, so achieving broad bandwidths has been the main goal in recent years.

However, broadband effects have been achieved, for example radiative chiral metasurfaces have been used to create low-profile, broadband circular polarisers by periodically arranging gold helices [81]. In other simpler structures optical rotation over a range of frequencies has been achieved through the use of complementary structures [93], sometimes coupled with their solid counterparts [85, 94], as well as significantly subwavelength structures [95].

An interesting point to note is that the control and manipulation of CP radiation is not limited to metasurfaces that have chiral unit cells. For example, a highly anisotropic metasurface will convert CP waves to linearly polarised waves. To do this it must convert some CP radiation to the opposite handedness (half if it is not lossy or diffractive). Such an effect can be measured separately from a chiral effect by looking at the transmission of both conserved and converted circular polarisations. An anisotropic, achiral metasurface will have $T_{++} = T_{--}$ but $T_{\pm} \neq T_{\mp}$, while an isotropic, chiral metasurface will have $T_{++} \neq T_{--}$ and $T_{\pm} = T_{\mp} = 0$. When transmission through anisotropic chiral metasurfaces or metamaterials is considered throughout this thesis, the converted CP coefficients are ignored and only the conserved CP parts are used in calculations.

Non-Radiative

A metasurface can also be designed to manipulate waves that have a higher momentum than a plane wave in free space, and are hence bound to the surface. They can be used for steering beams [96], for example to create 2-dimensional lenses [97]. The bound waves can also exhibit negative refraction [98].

In general a surface wave is chiral when there is hybridisation between transverse electric (TE) and transverse magnetic (TM) modes, the degree of which depends on the chirality parameter of the supporting material. There have been some theoretical investigations into surface waves supported at interfaces between chiral and achiral media [99, 100], which suggest that chiral surface plasmons have a cut-off and propagation length dependent on their chirality. Chiral surface waves that are supported by achiral materials with a defect have also been reported experimentally [101], although this surface wave only has a chirality over a very limited frequency range. It has been suggested that such waves could be used to more sensitively detect the handedness of chiral molecules or enhance the CD in emission.

Chiral Wave-Guides

The dimension can be reduced once more, and we arrive at one-dimensional wave guides. Since the 1940s [102], helical wave-guides have been studied as a means of transporting electromagnetic energy. Experimental investigations [103] were supported by theories [102, 104], most of which are reviewed in the work by Sensiper [105] in his 1955 book.

However, these wave-guides have uses beyond those envisioned last century. The very high indices that are achievable, coupled with the fact that (with careful tuning of parameters) they can be almost non-dispersive over a wide frequency range, make long helices good candidates for high index metamaterials, such as those based on Hilbert curves [106, 107]. Helically grooved wires, which are a limit

of a helix with zero spacing between adjacent turns, have recently been found to support helical plasmons in the THz [108] and act as sources of radiation with orbital angular momentum [109, 110].

2.2.4 Exciting Modes of Periodic Structures

This section is particularly relevant to chapter 6.

Coupling to Bound Modes

Typically, we describe the response of a metasurface using an energy-dispersion diagram, with the free space frequency of the incident light, ω, on the y axis and the in-plane momentum, k_x along the x axis, an example of which is shown in figure 2.13. The light line (thin grey line) indicates the dispersion of grazing incidence radiation, and is given by the equation $k_x = \omega/c$. The region to the left of the light line in blue is known as the radiative zone. This is the region where plane waves exist, with their in-plane momentum given by $k_x = (\omega/c)\sin\theta$ where θ is the angle of incidence. The region to the right of the light line, in green, is the non-radiative zone, occupied by modes with greater momenta than a free-space plane wave.

The thick dashed blue lines show a typical dispersion of a mode bound to a surface along 1-dimension. The mode lies outside the light line, so it cannot be excited with a plane wave incident from free space. One way to excite such modes is by placing a high-index dielectric prism above the structure that supports the bound wave, which increases the momentum of a plane wave and allows it to couple to the bound wave (Otto coupling [111]).

Adding Periodicity

The second method, and that used in chapter 6 of this thesis, is to introduce a periodically varying structure to the interface. The momentum of light incident from

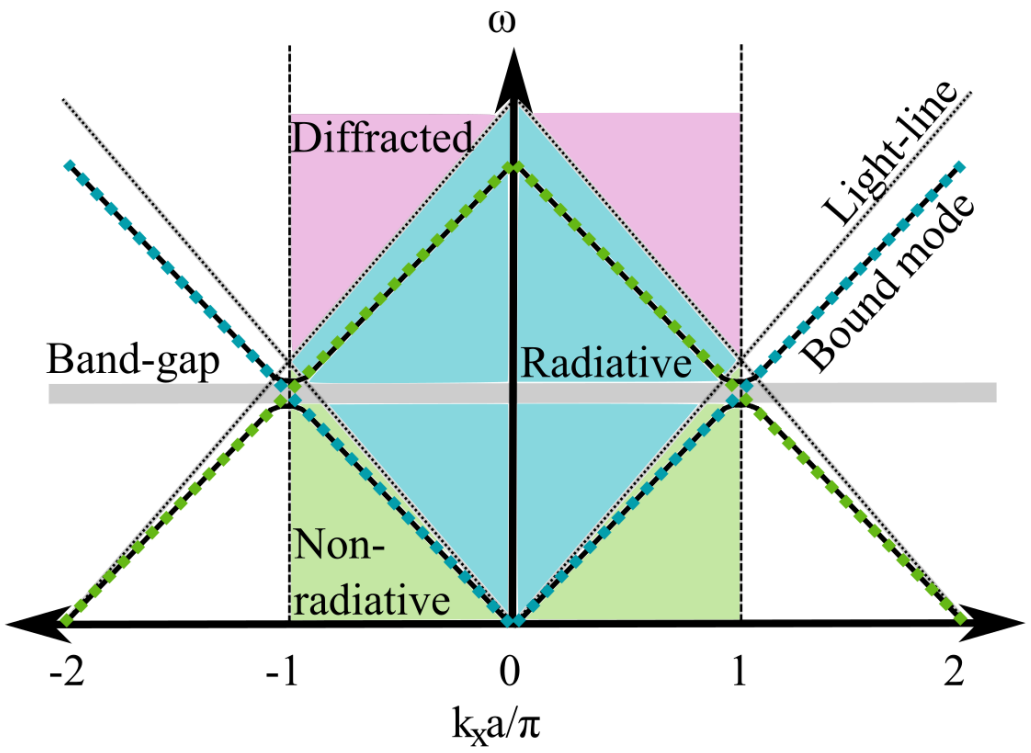

FIGURE 2.13: **Example of energy-dispersion for the mode of a periodic metasurface.** k_x is the in-plane wave-vector, a is the period of the array. Thin grey lines represent grazing incidence plane waves, and are known as light lines. The blue region is the radiative region, where all free-space plane waves can exist. The green region is the non-radiative region, where modes with momenta higher than those of plane waves exist, such as those coupled to the surface (thick black lines). The grey region shows a band-gap, where no propagating modes exist. The purple region contains diffracted modes. The dotted black lines represent the edge of the first Brillouin zone (BZ), within which all modes can be represented.

free space then increases through scattering off the features in the structure. For a structure that varies with a periodicity of a, the in-plane momentum is increased by multiples of the grating wave-vector, $k_g = 2\pi/a$, so that

$$k_x = k_0 \sin(\theta) \pm N k_g \tag{2.45}$$

where N is an integer and $k_0 = \omega/c$ is the free space wave-vector. The result of this is that the dispersion curve becomes periodic in $2k_g/\pi$ along the k_x axis. The regions bounded by the black dashed vertical lines in figure 2.13 represent the first Brillouin zone (BZ), which exists for $-\pi/a \geq k_x \geq \pi/a$. The first scattered mode, $N = 1$, is shown as the thick green dashed line starting at $k_x a/\pi = 2$, and we can see that part of this mode now lies inside the light line. It can be excited by a free-space plane wave with a given frequency and angle of incidence, and may also re-radiate into the specular (non-diffracted) wave. The interference of the diffracted modes can lead to standing waves at the points of the dispersion where they have matched frequency and wave-vector. The dispersion of the resultant mode is shown as the black line, and a band-gap where no propagating modes can exist (grey region) becomes apparent. Another important condition is that there must be some overlap in the fields of the incident wave with that of the bound mode, also known as the mode overlap.

The purple region of the dispersion plot contains modes that are above the onset of diffraction. Here, specular radiation is always accompanied by diffracted modes due to the periodicity of the structure. The interface between the radiative (green) and diffracted (purple) regions is referred to as the diffraction edge, also commonly known as one of Wood's anomalies [38].

By creating a periodic structure we now have access to part of the bound mode that falls within the radiative zone. However, we still cannot excite the bound mode at low frequencies, where the dispersion still lies within the non-radiative zone.

These can be excited using a near-field source of radiation, rather than a plane wave, as discussed in section 3.2.3.

Interpreting the Dispersion Diagram

There are two velocities defined for a wave, both of which can be deduced from the dispersion diagram. The first is the phase velocity, v_p, which is the speed at which the phase fronts progress, defined as:

$$v_\mathrm{p} = \frac{\omega}{k_\mathrm{x}} \tag{2.46}$$

This is the velocity that defines the refractive (or mode) index $n = c/|v_\mathrm{p}|$. The group velocity is the first derivative of ω with respect to k_x:

$$v_\mathrm{g} = \nabla_{k_\mathrm{x}} \omega \tag{2.47}$$

This defines the speed at which a wave can carry information, and is limited to be less than c. This velocity defines the group index $n_\mathrm{g} = c/|v_\mathrm{g}|$. The phase velocity is not limited, and can exceed values of c in media with $0 < n < 1$. The direction of power flow is determined by the group velocity, but can be opposite to the direction of the phase velocity in negative index media with $n < 0$. In media with a constant mode index, i.e. $\mathrm{d}n/\mathrm{d}k_\mathrm{x} = 0$, the group and phase velocity are equal, $n = n_\mathrm{g}$.

In figure 2.13, upon introducing periodicity we have introduced gaps in the dispersion, marked by grey zones, where no propagating modes can exist. At the BZ boundary there are two counter-propagating modes, one forward (blue line) and one that has been scattered backwards by the periodicity (green line), with the same wavelength. These overlap to produce two standing waves with zero group velocity (no gradient, no power flow). These modes have the same momentum but different energies as their charge configurations are different. This difference in the energies

of modes with the same wave-vector leads to a gap in the dispersion, the size of which depends on the charge and field configurations.

Adding Higher-Order Symmetries

So far we have looked at a dispersion diagram for a structure with simple translational symmetry along one dimension, which can be described by the translation operator, **T**:

$$\mathbf{T} = \begin{cases} x & \rightarrow & x + a \\ y & \rightarrow & y \end{cases} \tag{2.48}$$

There are various other symmetry operations that may be applied to a metasurface, such as glide symmetry. This is achieved by translating the unit cell along an axis by a distance $a/2$, where a is the period, and mirroring in a plane parallel to the translation axis. This is described in Cartesian coordinates by the operator, **G**:

$$\mathbf{G} = \begin{cases} x & \rightarrow & x + \frac{a}{2} \\ y & \rightarrow & -y \end{cases} \tag{2.49}$$

Of particular importance to the work in this thesis is screw or screw-axis symmetry, as found in helices. This is a combination of rotation around an axis of $2\pi/n$ radians and translation of a/n along the axis, where n is the order of symmetry. The screw operator, $\mathbf{S}_\mathrm{n}$, describes this symmetry operation along one direction in polar coordinates:

$$\mathbf{S}_\mathrm{n} = \begin{cases} x & \rightarrow & x + \frac{a}{n} \\ \theta & \rightarrow & \theta + \frac{2\pi}{n} \end{cases} \tag{2.50}$$

Glide symmetry can be thought of as a special case of screw symmetry of order $n = 2$ for simple geometries.

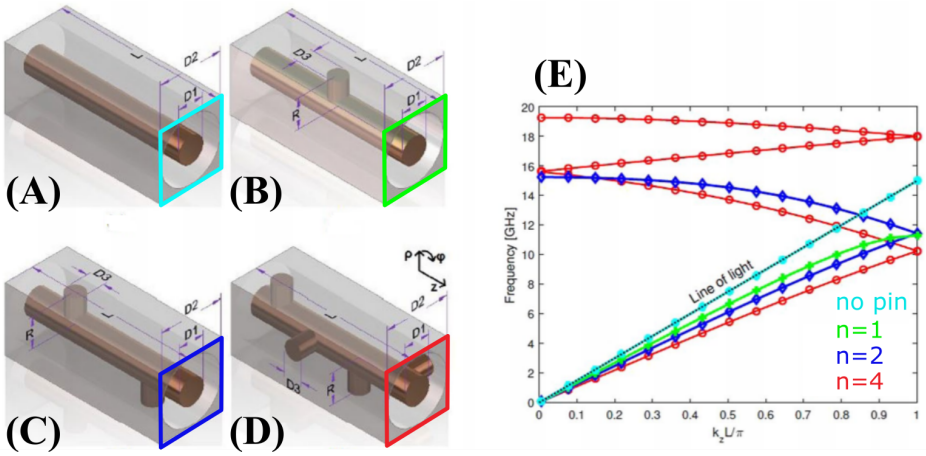

FIGURE 2.14: **Example of higher-order symmetries in a wave-guide. (A) - (D)** are schematics of coaxial-type wave-guides with various orders of screw symmetry, respectively $n = 0$ (no pin), $n = 1$ (translational symmetry), $n = 2$ (glide symmetry) and $n = 4$. **(E)** is the energy dispersion of the modes supported on each wave-guide in the reduced zone scheme, where the Brillouin zone (BZ) is defined by the length of the translational unit cell, L. The number of times a mode can cross the BZ edge without a band-gap is $n - 1$. Note that these models were performed in a cavity, hence no hybridisation of the modes with the light-line is observed. Reproduced from [112]

The presence of higher-order symmetries in an array alters the dispersion diagram. Most notably, the band-gaps at the BZ edge will close for some or all modes [113]. This is due to the mixing of even and odd modes, which are usually well-defined in translationally symmetric arrays. The nature of these modes is such that waves at $k = 2\pi/a$ with positive wave-vector are completely degenerate with those of negative wave-vector [113, 114].

This is true for the first band in the case of glide symmetric wave-guide or meta-surface [115, 116] and similar analysis can be applied to screw symmetric wave-guides [117]. A study was performed on the effect of increasing the order of screw symmetry of a coaxial-type wave-guide on the dispersion [112]. It was found that increasing the order, by adding pins perpendicular to the central wire, increased the number of times a mode could pass through the BZ edge without opening a band-gap. This is supported by previous work on reducing the symmetry order of

a helix, which has $n = \infty$, by adding dielectric rods along the length of the helix to open band-gaps [114].

This effect can be understood by the apparent enlarging of the true BZ [118]. Taking the simplest example of screw symmetry with $n = 2$, and inspecting the $\mathbf{S}_n$ and $\mathbf{T}$ operators, we see that applying the $\mathbf{S}_2$ operator twice is equivalent to applying the $\mathbf{T}$ operator once. We know from the Bloch theorem that a translationally symmetric system has a band structure that is periodic in $k_x = 2\pi/a$, so it follows that a 2-fold screw symmetric system is periodic in $k_x = 4\pi/a$. The same principle can be applied to any order of screw symmetry, with the BZ increasing with each increase in n. However in the reduced zone scheme we can still represent all modes within the translational BZ, defined as $k_x = 2\pi/a$, and is the convention that will be followed throughout this thesis.

2.2.5 Homogenisation

This section is particularly relevant to chapter 5.

It is often useful to extract effective material parameters that describe a metamaterial as a homogeneous medium. The ability to accurately make this approximation is often part of the definition of a true metamaterial.

Limits to Parameter Extraction

The very basic principle behind homogenisation is outlined in the Maxwell-Garnett mixing formula [119], which is valid for structures where the length scale of the inclusions is significantly less than the wavelength and their overall filling fraction is small. There have been many more recent advancements in homogenisation techniques, all of which are limited by the fact that the structure of the metamaterial must be on a shorter length-scale than the probing wavelength. Typically the accepted limit is $d < \lambda/10$ [120]. Recent work has shown that these predictions are

also limited by the number of meta-atoms in the material [120]. The environment of the edge meta-atoms is different to those in the bulk, and when only a few meta-atoms are studied the edge effects can significantly affect the overall response of the material.

While there are ways to theoretically predict the effective permittivity and permeability of a metamaterial based on the material parameters of its constituent parts, this is often not the most practical method. The parameters can be empirically implied via the comparison between measured (or numerically modelled) reflection and transmission coefficients, and those calculated from analytical equations that use effective parameters. This is done by testing material parameters until the difference between the measured and analytical coefficients is minimised. More details on minimisation can be found in section 3.4. Analytical expressions that describe the reflection and transmission through a layer of isotropic chiral media is outlined is section 2.1.3, and the same principles can also be applied to more complex media [121, 122].

Local and Non-local Approximations

Another limit to the effective parameter approach is of particular importance to this thesis. That is the difficulty in extracting non-local material parameters. All standard parameter extraction techniques assume that the material can be described as a collection of infinitely small point charges. This kind of effective parameter description is a local medium approximation, where the material parameters are a function only of the frequency of incident radiation.

However under some circumstances this approximation is not valid. For example, when exciting a local material at normal and off-normal incidence the permittivity and permeability remain the same (if the material is anisotropic the material parameters may be different along different axes in the material, but the tensorial

parameters themselves do not vary with changing angle of incidence). If there is some structure to the material that is on a similar length scale to the incident field, for example a one-dimensional grating, this is no longer necessarily true. The effective material parameters will now vary with the frequency and wave vector of the incident radiation, and the material must be described by non-local material parameters that reflect this.

Another case where non-local material parameters should be considered is when the incident field is not a plane wave. If a metamaterial is probed by an evanescent field with high wave vector components, the short spatial frequencies will be sensitive to structure in the metamaterial that is on a similar length scale. In this case a non-local effective medium description will be necessary. The non-local contribution to a chiroptical interaction forms the basis of chapter 5 of this thesis.

Only a simple local material description is considered in this thesis, although there are emerging techniques for the extraction of non-local material parameters in electromagnetic metamaterials [123, 124].

Application to Chiral Metasurfaces

True homogenisation is only valid when the extracted parameters are independent of the thickness of the material. In the case of a metasurface this is never true. Despite this limitation, there are many examples in the literature where extracting material parameters has provided useful insight into the behaviour of chiral metasurfaces. The general method involves finding expressions for the reflection and transmission from a layer of given thickness, in terms of the refractive index and chirality parameter. The refractive index describes the phase and amplitude of the wave at the output face of the layer, relative to those at the input face. Real transmission and reflection data can be fitted to these expressions and the material parameters

extracted. This technique can even be applied to a chiral material on a substrate [125], and has been used to confirm negative index chiral metamaterials [92, 126].

However, as described above, the effective index of a metasurface is very different to the effective index of a similar 3-dimensional metamaterial. The defining limit to this technique is that the material parameters will change if more than one layer is stacked together [92].

Chapter 3

Methods

Introduction

In this section I will outline the methods of fabrication, experimental techniques and numerical simulations used to study the topics in this thesis.

Fabrication methods used to make the samples studied in this thesis are discussed first. These include top-down (subtractive) methods, including two kinds of lithography, and bottom-up (additive) methods, such as selective laser sintering. Two kinds of experimental techniques are also discussed, both of which use vector network analysers to produce and detect GHz frequency signals. In measurements of far-field effects, horn antennas produce and collect linearly polarised waves, whereas measuring near-field effects requires electrically small sources and probes, positioned close to the structures being tested. Finite element method models are used throughout the thesis, and these will be discussed in the following section. The final section contains details on the minimisation techniques used in the analytical models, which are discussed in more detail in the following chapters.

Along the way, the chapters where the methods have been employed will be highlighted.

3.1 Fabrication

There are several kinds of sample used in the work presented in this thesis, manufactured using both top-down (subtractive) and bottom-up (additive) techniques. In chapters 4 and 5 two dimensional metasurfaces or antenna arrays are investigated. These are produced using a top-down lithography technique. Chapter 5 also deals with two-dimensional arrays of three-dimensional helices. These helices were arranged in grids made using an additive manufacturing technique by 3D Systems on Demand Manufacturing, Quickparts. This technique will be outlined in section 3.1.2 The helices were manufactured by Huidong Linglong Spring Co. Ltd, and no attempt was made to azimuthally align them when placing them in the grid.

In chapter 6 the electromagnetic waves supported on individual long helices are investigated. These were simply re-purposed long springs from inside a traditional net curtain rail.

3.1.1 Lithography

This technique was used in chapters 4 and 5.

The process of photolithography for patterning metal on a dielectric substrate is illustrated in figure 3.1.

1.6 mm thick FR4 substrates, laminates used in printed circuit board manufacturing, with a 35 μm thick layer of copper and 5 μm thick layer of positive photoresist on one side can be bought directly from Mega Electronics. Each board is selectively exposed to UV radiation through a mask. The mask is either printed on acetate in-house or purchased from JD Photodata for higher resolution (up to 5 μm) and contrast (0.001 % transmission), and is the inverse or negative of the desired pattern. After exposure under a low-powered but uniform UV beam of diameter around 40 cm for 55 minutes, the photoresist is developed in room temperature Seno Universal

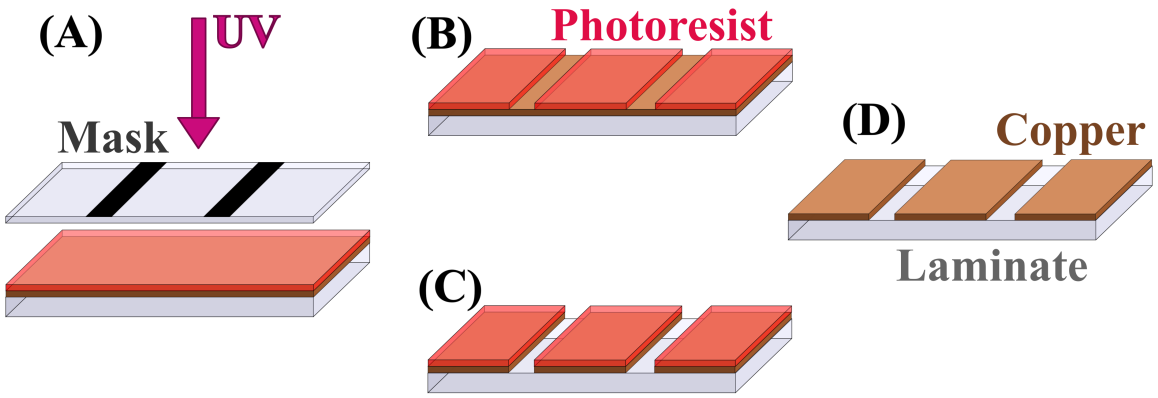

FIGURE 3.1: **Outline of lithography technique. (A)** The printed circuit board with copper and photoresist is exposed to UV radiation through a mask. **(B)** The board is developed and the unexposed regions of photoresist washed away. **(C)** The copper that is not protected by a layer of photoresist is etched away in ferric-chloride. **(D)** The rest of the photoresist is removed with acetone and the patterned copper left behind.

Developer solution for 3 minutes, removing the regions of photoresist that were not exposed to UV. The board is then etched in ferric-chloride for 20 minutes, and any regions of copper that were not protected by the photoresist are removed. Finally, the rest of the photoresist is washed away using acetone, and the copper pattern is revealed.

The limit to the resolution of this technique is set by the diffraction of the UV radiation around the edges of the mask, and second by the maximum length of polymer chain in the photoresist. All samples used in this thesis are far from either limit, but over-exposure and over-etching were persistent problems, leading to an extra 20 μm being etched away along every edge of the copper. This was taken into account in the modelling and design.

For samples requiring copper on both sides of the substrate, this process was performed by local printed circuit board company, Graphic PLC, to ensure a good match between upper and lower layers of the copper, which was impossible to achieve in-house. In this case the substrate is a 0.406 mm thick layer of Isola Tachyon printed circuit board with an 18 μm thick layer of copper on top and bottom.

3.1.2 Additive Manufacturing

This method is relevant to chapter 5.

Selective laser sintering (SLS) is one of many emerging techniques in additive manufacturing. Its popularity is due to the fact that it can be used to print a variety of materials, including dielectrics, ceramics and metals, albeit one material at a time. The pieces used for this work were manufactured by 3D Systems On Demand Manufacturing, QuickParts.

Duraform PA, used to make the samples in this thesis, is a semi-crystalline nylon polymer. In comparison to the amorphous polymers also available, these create mechanically strong, fully-filled parts, although they have a greater surface roughness. They are subject to around 3 - 4 % shrinkage during manufacturing, and also warping at high aspect ratios. These effects were taken into account during the design. The permittivity was measured using a strip-line technique, and found to be $2.73 + i0.03$ across the frequency band of interest.

The Duraform PA is placed in the machine in the form of a powder. A pulsed CO_2 laser with a central frequency of around 10.6 μm is used to selectively sinter the powder in regions dictated by a computer-aided design (CAD) drawing, causing the powder particles to stick together. The resolution of this technique is limited by the diffraction of the laser and the maximum size of particle in the powder, making the tolerance around 0.5 %, with a minimum part size of around 1 mm. At the end of the build the unsintered powder is washed away. No post-processing was carried out on the parts used in this thesis.

3.2 Experimental Techniques

3.2.1 Network Analysers

This piece of equipment was used in all chapters.

All experimental results presented in this thesis are collected using a Vector Network Analyser (VNA); a commercial piece of equipment. It is used to generate and detect GHz-frequency signals, allowing the characterisation of metamaterials and antennas. The model used is the Anritsu MS4644A. It differs to a Scalar Network Analyser in that it can record the phase of the signal as well as the amplitude.

Figure 3.2 shows a simple schematic of the workings of a VNA. Within the source a voltage controlled oscillator produces an alternating current signal that is referenced to a stable, low frequency clock. The signal is passed through phase-locking loops to ensure stability over time. Mixing two such signals, with filters to remove any unwanted harmonics, generates an output signal with any frequency between 10 MHz and 40 GHz.

A portion of the signal is split off by a directional coupler and measured before it passes through the device, to act as a reference (a1 or a2). The rest of the signal is carried to and from the device under test by coaxial cables. These are amplitude and phase stable, so that moving or bending the cables does not significantly affect the signal. However there are losses and impedance mismatches associated with the cables, and these must be removed by performing a standard short-open-load-through calibration before measuring a device.

The reflected or transmitted signals are separated from the forward travelling output signals by another directional coupler (b1 and b2). The directivity of these couplers is never perfect, and mixing with the unwanted signal leads to oscillations and noise in the measured signal.

Measured signals are down-converted to a lower frequency by a local oscillator

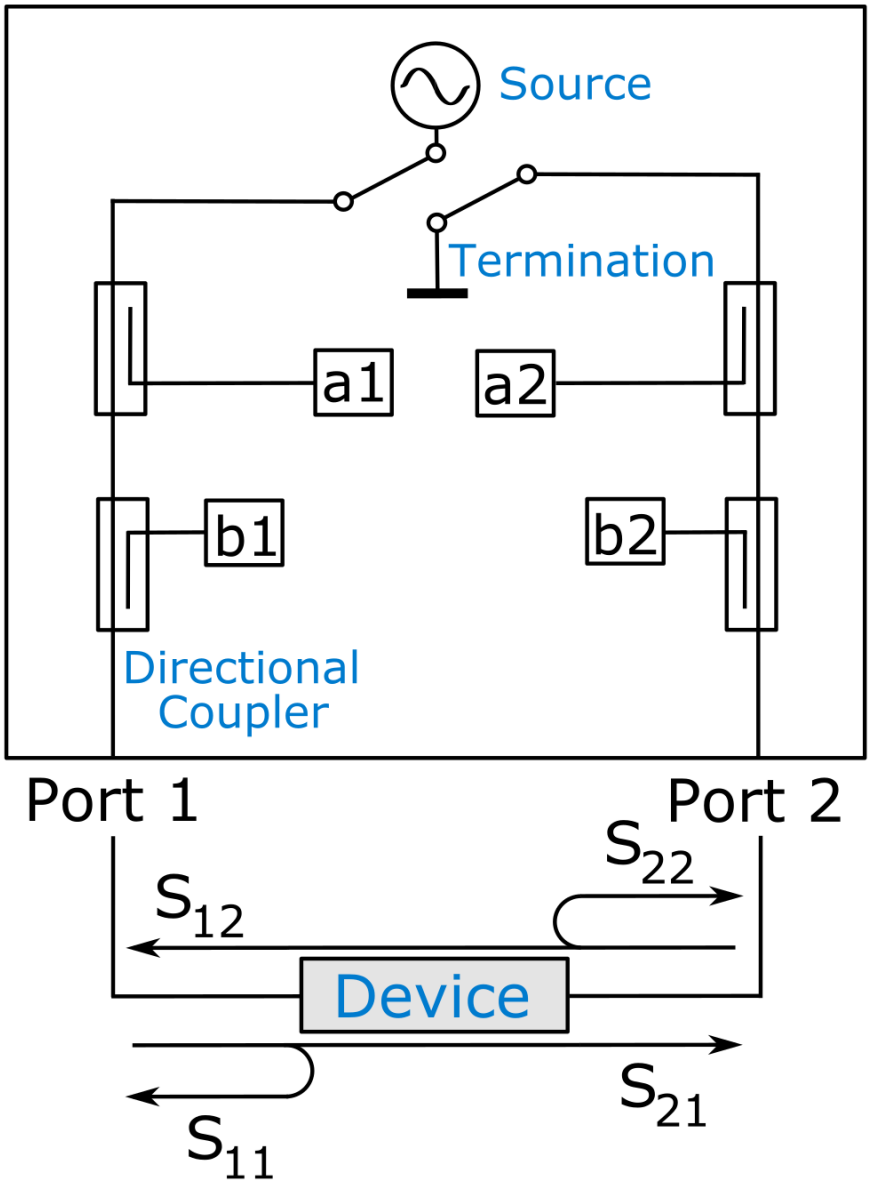

FIGURE 3.2: **Schematic to show the inner workings of a Vector Network Analyser.** An alternating current signal is produced by a pair of voltage controlled oscillators at the source. This travels through a directional coupler where a portion is collected for referencing ($a_{1,2}$). The rest of the signal passes to the device, and after the reflected and transmitted signals are separated from the outgoing waves by more directional couplers ($b_{1,2}$) and measured. The rest of the signal passes to the termination where it is absorbed, and a switch allows signals to be sent from either port.

to allow signal processing within the VNA. This method of down-conversion allows the phase information of the measured signals to be preserved. A more detailed discussion on the operation of a VNA can be found in [127].

The values that are measured from the VNA are termed scattering-parameters or S-parameters, and are calculated as ratios between the referenced and detected signals. They are labeled S_{nm} where n is the receiving port and m is the emitting port. They are calculated via:

$$\begin{pmatrix} b_1 \\ b_2 \end{pmatrix} = \begin{pmatrix} S_{11} & S_{12} \\ S_{21} & S_{22} \end{pmatrix} \begin{pmatrix} a_1 \\ a_2 \end{pmatrix} \tag{3.1}$$

where $a_{1,2}$ and $b_{1,2}$ are the reflected and measured signals indicated in figure 3.2. A VNA is able to record both the phase and amplitude of a signal, and this information is held in the real and imaginary parts of complex S-parameters. These can be plotted in either decibels (dB) or linear ratios.

3.2.2 Radiative Measurements

This measurement was used in chapters 4 and 5.

One of the concepts studied in this thesis is how the polarisation of a wave changes as it travels through a metallic patterned surface. To study this experimentally the surface is illuminated with a plane wave, and the transmitted wave measured on the far side. This is the principle of radiative measurements, as they probe the structures' responses within the radiative region of the energy-dispersion diagram in figure 2.12 of section 2.2.4.

Experimental Set-Up

Measuring the transmission through a sample is performed using the set-up illustrated in figure 3.3. A microwave signal is generated by the VNA (as described

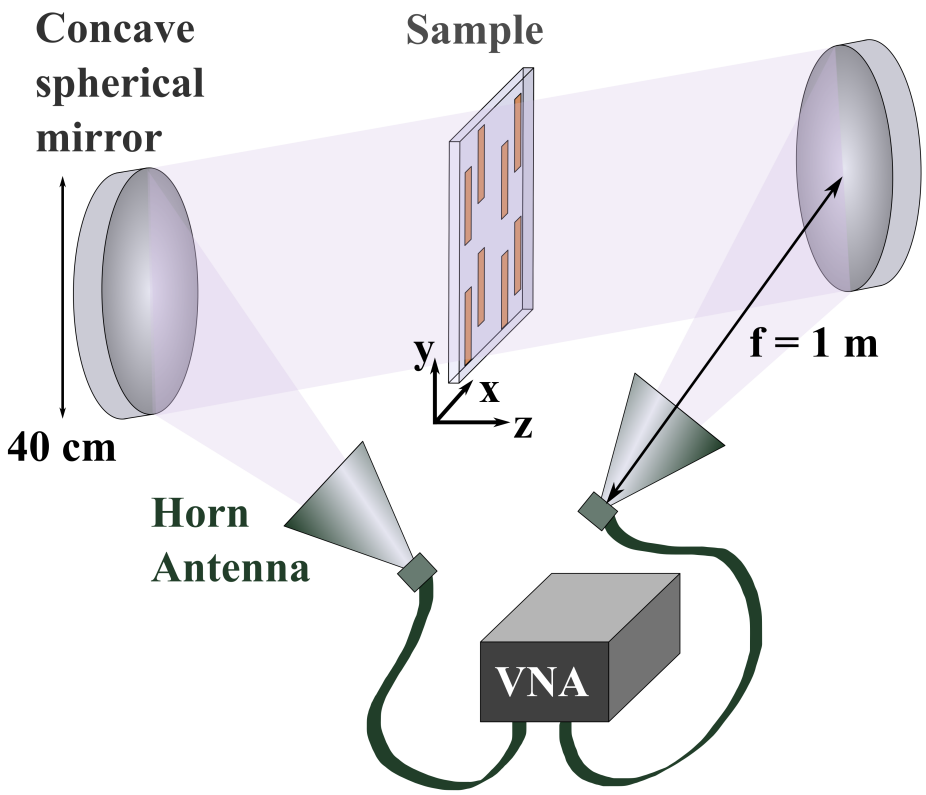

FIGURE 3.3: **Schematic of radiative experimental set-up.** A signal produced by the VNA is carried along a coaxial cable to a horn antenna that emits a hemispherical wave. This is collimated by reflection from a spherically concave mirror, passes through the sample, then is reflected off another identical mirror into another horn antenna to be measured by the VNA. The horn antennas can be azimuthally rotated to emit and collect linearly polarised waves of different polarisations.

in section 3.2.1), and travels along a coaxial cable to a horn antenna, that emits a free-space wave. This wave has almost spherical wave-fronts while still being quite directional, as shown in figure 3.4. The horn antenna is placed at the focal point of a spherically concave mirror with a radius of 20 cm and a focal length of one metre, where in the small arc approximation it can be treated as parabolic. The wave reflected from the mirror is nearly collimated, and has a beam diameter of around 200 mm. It passes through the sample, before being reflected from a second identical collimating mirror and collected by a second horn antenna one metre away.

As the diameter of the beam emitted from the horn antenna is larger than the diameter of the mirror, diffraction around the edges can be a problem. Similarly the wave can diffract around the sample if it is smaller than the beam diameter. To avoid this, pyramidal absorbing material is placed around the edges of the mirror and the sample. This is an elastomer foam loaded with flakes of graphite to create a material with a large dielectric loss tangent [128]. The side on which radiation is incident is tapered to create an index that gradually varies from that of free space to that of the absorber. The result is 99% absorption over all frequencies studied in this thesis up to an incident angle of 60°. To reduce other unwanted reflections, frames, sample-holders and other components are made from wood or perspex where possible, and covered with sheets of absorber otherwise.

Horn Antennas

The horn antennas convert the signal guided by the coaxial cable into a free-space wave. They do this with a specific linear polarisation and for a range of frequencies defined by their geometry. The coaxial cable feeds into a waveguide adaptor where the central wire acts as a dipole antenna to excite the fundamental transverse-electric (TE) mode of a rectangular waveguide. This mode propagates along the rectangular waveguide as it gradually increases in cross-section in a manner designed to match

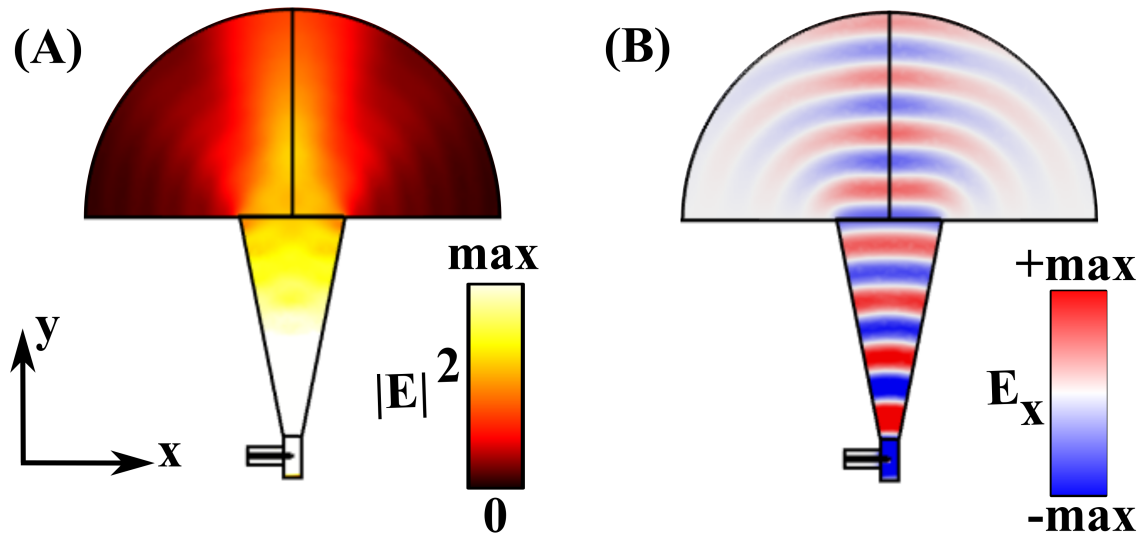

FIGURE 3.4: **Electromagnetic radiation produced by a horn antenna (triangular section) fed by a coaxial cable, emitted into free space (semi-circular section). (A)** shows the time averaged electric field intensity, illustrating the directivity of emission from the horn antenna. **(B)** shows the x-component of the instantaneous electric field along, which illustrates the curved phase-fronts of the emitted wave. In experiment, a spherical mirror is used to collimate the beam.

the impedance of free space ($Z_0 \approx 377\Omega$). The wave emitted from a horn antenna is depicted in figure 3.4. Similar to a normal rectangular waveguide, the horn antenna has a cut-off frequency that corresponds to a half-wavelength quantisation across the width of the rectangular waveguide section, a:

$$f_c = \frac{c}{2a} \tag{3.2}$$

assuming that the waveguide is filled with air and the wave travels at the speed of light in vacuum, c. The impedance of the waveguide depends on this cut-off frequency,

$$Z = Z_0 \left(1 - \frac{f_c}{f}\right)^{-\frac{1}{2}} \tag{3.3}$$

The impedance, and so the output power and directivity of the horn antenna, also varies with frequency, so narrow-band horn antennas are used in the experiments

in this thesis. The frequency bands are industry standards, and those used here are the Ku (12 - 18 GHz), K (18 - 26.5 GHz) and Ka (26.5 - 40 GHz) bands.

S-Parameters

Even within the specified frequency ranges for each horn there will be a frequency dependent spectrum that cannot be accounted for in the calibration (described in section 3.2.1). Therefore all transmission measurements are normalised to the transmission measured across the set-up without the sample in place. The normalised spectra are usually plotted on a linear scale, however if variations at small signals are to be studied, a logarithmic scale can be useful. If A is the signal measured in dB of the system with the sample in place, and B is the reference, measured without the sample, we can write the resultant normalised S-parameter as

$$S = 10^{\frac{(A-B)}{10}} \tag{3.4}$$

or

$$S_{\mathrm{dB}} = 10\log_{10}(S) = A - B. \tag{3.5}$$

The wave emitted from a horn antenna maintains the linear polarisation of the fundamental TE waveguide mode. All experiments performed in this thesis use linearly polarised incident waves. The horn antennas are mounted in such a way that each can be azimuthally rotated by 90°. This allows the collection of the four polarisation-dependent S-parameters needed to calculate the circularly polarised transmission coefficients as described in section 2.1.4.

3.2.3 Non-radiative Measurements

This kind of measurement was performed in chapter 6.

It is also possible to experimentally study waves that are trapped at the interface between two different materials. These bound waves have momenta greater than a plane wave in free space, and exist in the region outside of the radiative region in the energy-dispersion diagram (figure 2.12 of section 2.2.4). Therefore they cannot be excited or detected by plane waves, so we must use evanescently decaying electromagnetic fields to excite and probe these bound modes.

Experimental Set-Up

The aim of this experiment is to characterise a wave that is travelling along an interface. To do so, we excite the wave using a signal from the VNA that travels along a coaxial cable that has had around 1 mm of the outer dielectric and metal casing stripped away, exposing only the central pin. This is the near-field source, and can be positioned at the edge of the sample or in the centre, on the opposite side to the probe. The probe, another piece of stripped coaxial cable, is attached to the moving arm of an XYZ stage (from Aerotech and Hepco Motion). The probe is raster-scanned across the sample, and the electric field amplitude and phase measured across a frequency range at each point. A Labview code controls the stage and the VNA, automating data collection. The total available scan area is a cube with sides around 1 m in length (although this volume was not needed for the results presented here), and the smallest step-size possible is 200 μm. Figure 3.5 shows a typical set-up for measuring a surface wave on a 1D grating.

Similar to the far-field measurements, reflected and scattered waves can be a problem, so much of the equipment is made from perspex or wood, and pyramidal absorber is used to cover any reflecting surfaces in the vicinity. Often the edge of the sample reflects the bound waves, reducing the quality of the data collected. This can be somewhat mediated by placing absorber at the sample edges. However in the experiments presented in chapter 6, the long helix does not support a wave that

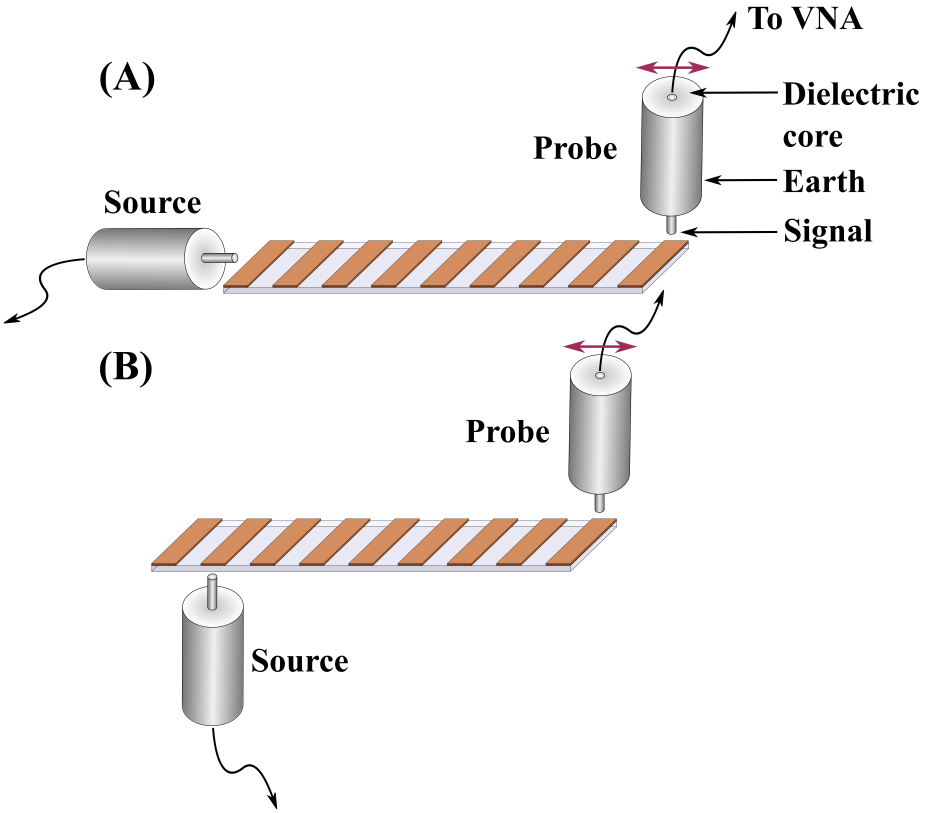

FIGURE 3.5: **Schematic of experimental set-up for non-radiative measurements using two orientations of source.** A fixed coaxial cable with a length of central pin exposed is positioned close to the structure that will support the bound wave. Another coaxial cable is held by a moving arm and scanned along the surface. A Fourier transform of the measured spatial distribution of the electric field reveals the energy-dispersion of the bound wave. In **(B)** the source and probe have the same orientation, chosen to strongly excite a TE surface mode, whereas in **(A)** the source is perpendicular to the probe reducing the cross-talk between them.

has changed handedness upon reflection, and so the issues associated with these reflections are minimal.

Near-Field Probes

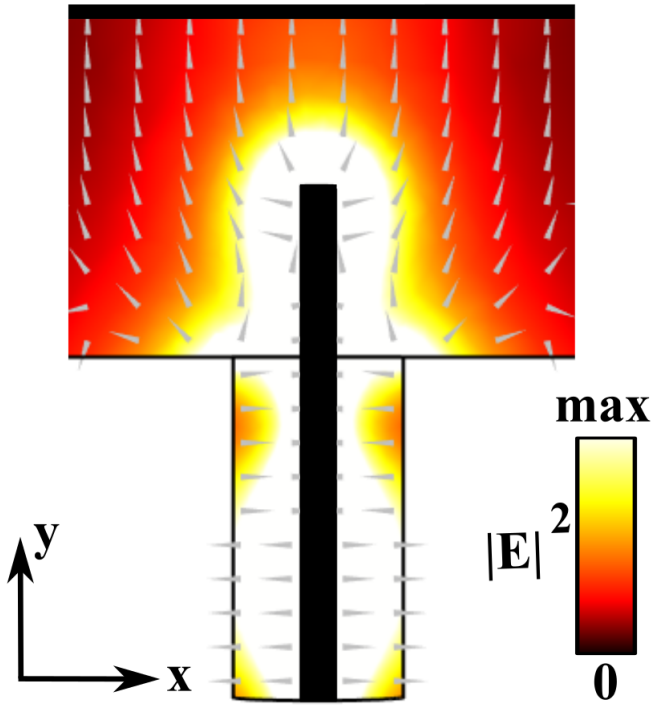

FIGURE 3.6: **Time averaged electric field intensity (colour) and direction (grey arrows) around a stripped coaxial cable above a conducting surface at 6 GHz.** These stripped cables act as sources and probes of electromagnetic near-fields in non-radiative experiments. Metallic parts of the stripped cable and conducting sheet are shown in black.

To understand fully the results collected in these measurements it is necessary to understand the behaviour of the source and detector. Figure 3.6 shows the electric field intensity around a stripped coaxial cable, just above a perfect electrically conducting (PEC) surface, calculated using a finite element method (FEM) model. We see that the field is tightly confined to the central pin, and does not readily radiate to free space. There will always be a small amount of free-space radiation produced, and the efficiency of radiation does increase with increasing frequency, as the pin approaches the regime where it is naturally resonant. For a 1 mm long stripped pin

this occurs at around 150 GHz, depending on the environment of the pin, while our frequency range of interest is up to 40 GHz.

While these stripped coaxial cables will not readily excite free space waves, they can be used to excite other waves, such as those bound to an interface between two different media. There are components in the near-field around a central pin with momentum greater than that of a plane wave (which must have momentum inside the light line $|k_{\mathrm{pw}}| \leq \omega/c$). This field then has enough momentum to excite a wave that lies outside the light-line on an energy-dispersion diagram. The field around the pin also contains a range of wave vectors, enabling us to build a full energy-dispersion from a relatively simple measurement.

Figure 3.6 shows that the electric field around the probe has some components along y and radially around the pin, but directly underneath, the E_y component dominates when close to a PEC surface. Placing the probe vertical to a PEC interface means that it will strongly excite a wave with E field perpendicular to the interface. Similarly probing the wave in this configuration means the field normal to the surface will be detected most strongly, but we will also pick up a small amount of the in-plane field. If the surface was a perfect magnetic conductor (PMC) the field distribution would be quite different, with the electric field mostly parallel to the surface. In this case, the central pins of the sources and probes can be twisted into loops to increase the strength of excitation.

Another problem to be minimised is that the probe will pick up a small amount of field from the source that is not bound to the interface. Positioning the source and probe on opposite sides of the sample or with perpendicular polarisations when possible reduces this. We must also consider that the presence of the source and probe slightly perturbs the fields we wish to detect. However, provided they are small compared to the wavelength and the periodicity of the structure, this effect is small.

Reciprocal Space

Using this near-field scanning technique we measure the amplitude, E_0, and phase, ϕ, of the (predominantly) normal component, z, of the electric field for a range of frequencies, at a series of positions above the structure we are testing. These are combined to give the instantaneous electric field following:

$$E_{\text{inst}} = \mathbb{R}\left(E_0 \exp\left[i\phi\right]\right) \tag{3.6}$$

An example of the collected data is shown in figure 3.7. Due to the finite length of the sample, the electric field is complicated by waves reflected from the edges of the sample and unbound waves propagating through free space. This becomes particularly clear in the phase plots in figure 3.7 (C) and (D), so it is difficult to extract any useful information from these. We can take a 2-dimensional Fourier transform (FT) of this data, shown in figure 3.7 (E) and (F). This plot shows the wave-vectors along x and y directions of the surface wave, along with the corresponding weighting factor, the Fourier amplitude. The iso-frequency contour associated with a mode at a particular frequency becomes clear. Grazing incidence radiation that is not bound to the structure is indicated by the red circle in the centre, while modes that are bound and have more momentum appear outside this light-circle.

We can repeat this analysis over a range of frequencies, and build up a 3-dimensional energy-dispersion plot as a function of the two wave-vectors and frequency. Free-space radiation appears as a cone, and bound-modes appear as surfaces outside this. Taking slices through this plot at either $k_{\text{x}} = 0$ or $k_{\text{y}} = 0$ produces the typical energy-dispersion diagram, as in figure 2.12 of section 2.2.4.
The real space co-ordinates are a sequence of N values:

$$\left[0, \Delta x, ..., \left(N-1\right)\Delta x\right] \tag{3.7}$$

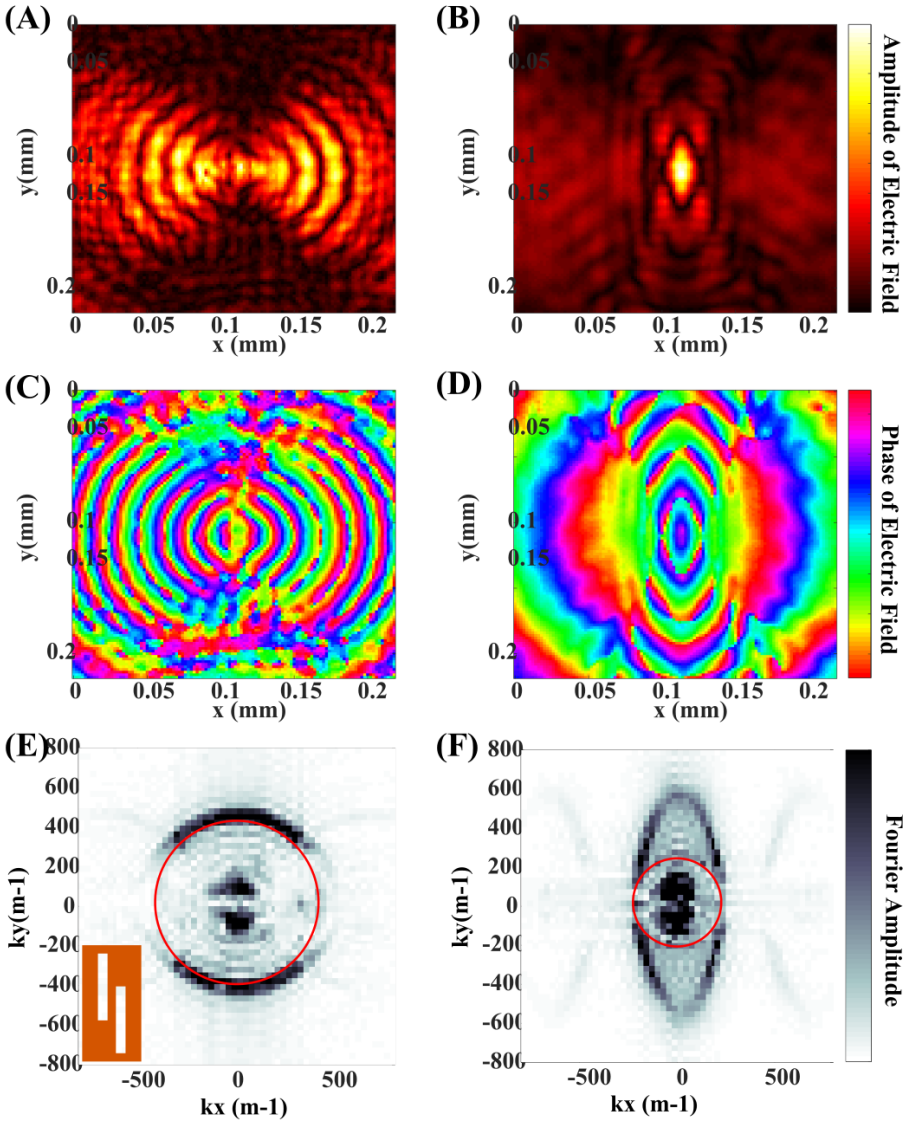

FIGURE 3.7: **Experimentally measured electric field and iso-frequency contours of a surface wave on the periodic staggered-slot array. (A)** and **(B)** show the amplitude of the electric field normal to the surface of the array at two different frequencies. **(C)** and **(D)** show the phase of the electric field at the same two frequencies. **(E)** and **(F)** show the iso-frequency contours, found by taking a two-dimensional Fourier transform of the instantaneous electric field, where the red circle is the light-circle. **(F)** shows the presence of an anisotropic surface wave, also seen as "beaming" of the surface wave in **(B)** and **(D)**. Inset in **(E)** is a schematic of a unit cell of the staggered-slot array, with dimensions similar to the rod-array studied in chapter 5.

where Δx is the step size and $(N-1)\,\Delta x = L$ is the total length of the sample. The coordinates in reciprocal space are given by:

$$[-k_{\max}, -k_{\max} + \Delta k, ..., 0, ..., k_{\max}] \tag{3.8}$$

for even N, and

$$\left[-\left(k_{\max} - \frac{\Delta k}{2}\right), -\left(k_{\max} - \frac{\Delta k}{2}\right) + \Delta k, ..., 0, ..., \left(k_{\max} - \frac{\Delta k}{2}\right)\right] \tag{3.9}$$

for odd N, where

$$k_{\max} = \frac{\pi}{\Delta x} \tag{3.10}$$

and

$$\Delta k = \frac{2\pi}{L + \Delta x} \tag{3.11}$$

are the maximum wave-vector and resolution in wave-vector space of the resulting Fourier transform. We see from these that the maximum wave-vector is determined by the step size in real space, but the resolution of the wave-vector relies mostly on the total length of the sample. If we wish to plot an energy-dispersion that covers the first two Brillouin zones, at least two measurements per unit cell must be made, and the scan should cover as many unit cells as possible to achieve a high resolution energy-dispersion plot.

3.3 Modelling

Numerical simulations of the systems studied in this thesis provide insight beyond what we can achieve experimentally. They are also useful for performing initial

tests of structures and refining geometries for specific frequency bands. Two commercial softwares are used throughout the work, ANSYS® HFSS™ and Comsol Multiphysics®, which both implement the finite element method (FEM). Each software has particular strengths and weaknesses, in particular Comsol allows for easy manipulation of the wave equation, while HFSS has superior meshing capabilities. Two types of models are used, grouped into 'driven' and 'eigenmode' types. In driven models, electromagnetic waves are launched and detected by ports, whereas in the eigenmode models there are no incident waves, and the software simply computes the resonant frequencies of the system.

The principles of both of these types of models are outlined below, as well as a description of how the software finds the solutions, and the limits to accuracy that are always present.

3.3.1 Finite Element Method

This technique was used in all chapters.

As the name suggests, this method creates a mesh to break up a geometry into discrete elements, most commonly tetrahedra. The software then solves Maxwell's equations at each vertex and at the mid-point of the edge of each mesh element. The results are interpolated between these discrete points to produce a solution for the entire geometry.

Solutions of Maxwell's equations are found through implementing the weak formulation. This involves writing a differential equation for the conservation of the flux of a physical quantity (e.g. electric field) in a finite region of space. This is written as an integral and solved for a set of boundary conditions using a sampling technique. The integration leads naturally to a Neumann boundary condition, where the flux of the physical quantity is zero at the boundaries. Another approach will satisfy a Dirichlet boundary condition, where there is a fixed value of flux at the

boundaries. In reality, this calculation is performed via a matrix, where most of the matrix elements are zeros, creating a sparse matrix that can be efficiently solved by a computer.

This is how the weak formulation is implemented in one region of space. However in FEM the geometry itself is broken down into discrete mesh elements, and the solution found inside each one. We define a set of basis functions Ψ, where there are two basis functions (for a simple one-dimensional model as in figure 3.8) in each mesh element. These can have a linear or higher order dependence on space. In general choosing a lower order dependence requires a more dense mesh, but reduces the computation time per element. Usually a linear or quadratic function is chosen based on the gradient of the electric field and density of the mesh. The shape functions are assigned a coefficient, a so that they approximate a function that represents the true solution, ensuring the solution is continuous across all boundaries.

Since it is these shape elements that approximate the real solution, the more densely packed these functions are, the better the approximation. However only an infinitely dense array of shape functions, and infinitely small mesh elements, will give us the exact true solution. Therefore the quality of the mesh in any model is of high importance, and convergence testing is carried out to ensure the mesh density is high enough to find a solution that reflects the real system. In convergence testing, the model is solved for an initial mesh at a high frequency, and a parameter, for example S21, calculated. The mesh is refined, particularly in areas where the gradient of the field is strongest, and the model solved again. This process is repeated until the change in the parameter is below a user defined limit, and the model has converged, as illustrated in figure 3.9.

3.3.2 Boundary Conditions and Excitations

This section is relevant to all chapters.

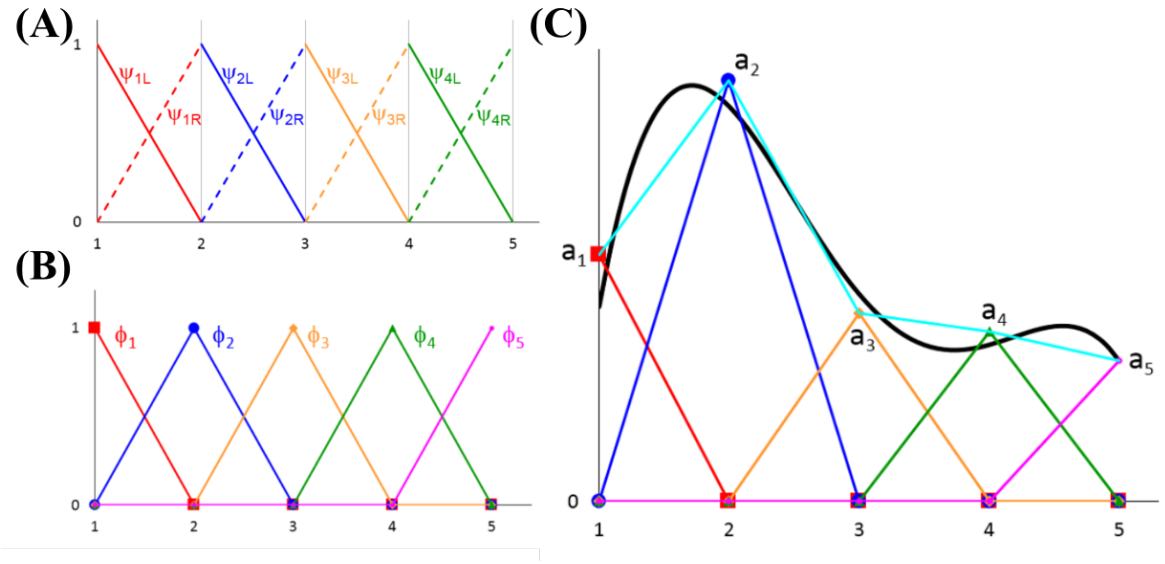

FIGURE 3.8: **Implementation of the weak formulation in finite element method models.** In **(A)** a simple one-dimensional space is broken into 4 sections, or mesh elements, bound by 5 nodal points, with each mesh element described by two basis functions, Ψ. These are forced to match at each of the nodal points and simplified to a set of triangular-shaped linear functions, Φ, shown in **(B)**. These functions are used to approximate a black curve, in **(C)**, which represents the 'real' solution of the problem (black line). The result (cyan line) is not a good approximation in this case, as the mesh is not dense and the functions are linear instead of quadratic. Image reproduced from the Comsol Multiphysics® user manual.

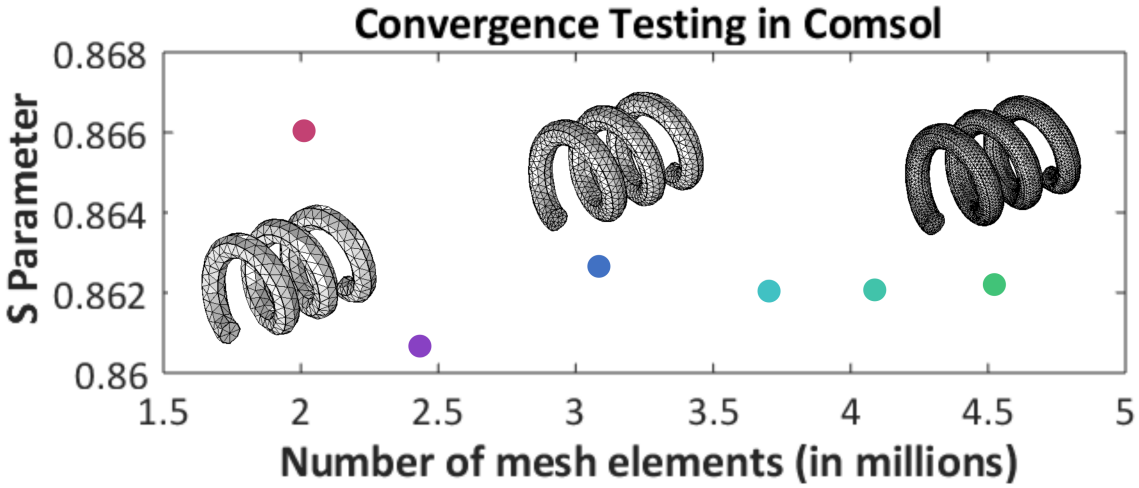

FIGURE 3.9: **Effect of meshing on model convergence.** A test parameter, in this case an S-parameter, is found for the same model with increasing number of mesh elements until further changes to mesh elements do not significantly change the S-parameter.

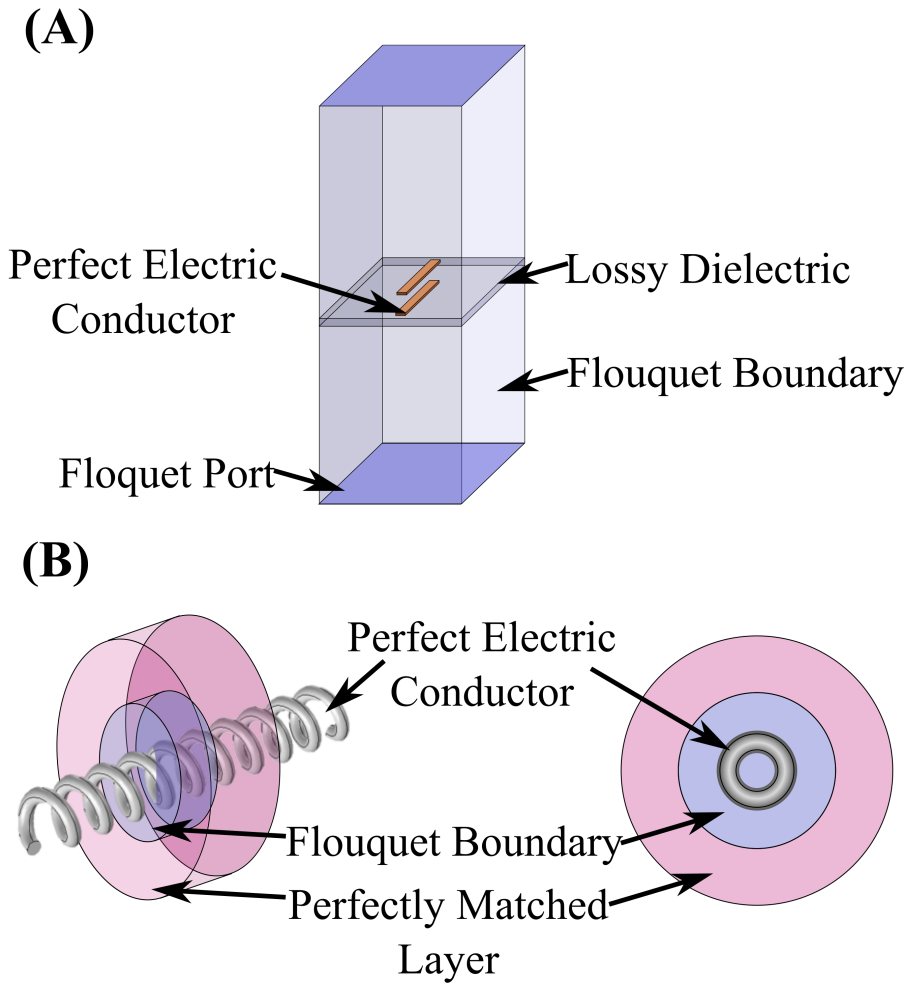

FIGURE 3.10: **Basic set-up of some finite element method models. (A)** shows an example of a driven model, with Floquet boundary conditions (BC's) on the vertical faces, and Floquet ports on the horizontal faces. **(B)** shows an example of an eigenmode model of an infinitely long helix. Floquet BC's intersect the helix, taking one full turn inside the model. A PML surrounds the unit cell, and no ports are included. All dielectrics are defined by a complex refractive index, and metals are treated as perfect electric conductors.

The structures studied in this thesis are often arrays of repeating elements. The most efficient way to simulate an array is by building a model of only one unit cell and applying periodic boundary conditions (BC's) known as Floquet BC's to the surfaces perpendicular to the array plane. These replicate an infinite array by setting up an appropriate phase difference between opposite faces of the unit cell, according to Bloch wave theory.

The faces of the model that are parallel to the array can be used to launch and detect plane waves in a driven model. This requires a Floquet port that, when used alongside Floquet periodic BC's, will launch a plane wave with infinite extent across the periodic array, and a specific polarisation and angle of incidence, and similarly detect one. This allows us to find the reflection and transmission S-parameters to compare to experiment.

For an eigenmode model, where incident excitations are not needed, a different BC must be applied to the parallel faces. A perfectly matched layer (PML) can be used to approximate an absorber. These regions gradually absorb incident radiation over a length of space without any reflection, for a given angle of incidence.

In general all metallic elements studied in this thesis are modelled as perfect electric conductors (PEC), as at microwave frequencies metals are almost perfectly conducting with negligible skin-depth. The empty regions in the models are air, and any dielectrics are defined via their complex refractive index.

3.3.3 Chiral Media

This technique was used in chapter 5.

When modelling an effective chiral material in a FEM model, simply adjusting the material parameters in a region of the model is not adequate. It is necessary to adjust the wave equation in one domain of the model to take into account the cross terms in the constitutive relations (equation 2.3 in section 2.1.3). These models were

created and solved in Comsol Multiphysics®. New definitions for the polarisability are set to take care of the contribution to polarisation from the incident magnetic field according to:

$$P_x = \epsilon_0 \left(\epsilon_{xx}E_x + \epsilon_{xy}E_y + \epsilon_{xz}E_z - E_x\right) - \frac{i\kappa_{xx}H_x}{c}, \tag{3.12}$$

$$P_y = \epsilon_0 \left(\epsilon_{yx}E_x + \epsilon_{yy}E_y + \epsilon_{yz}E_z - E_y\right) - \frac{i\kappa_{yy}H_y}{c}, \tag{3.13}$$

$$P_z = \epsilon_0 \left(\epsilon_{zx}E_x + \epsilon_{zy}E_y + \epsilon_{zz}E_z - E_z\right) - \frac{i\kappa_{zz}H_x}{c}. \tag{3.14}$$

The magnetisation from the incident electric field is included by adjusting the time derivative of the magnetisation,

$$\frac{dH_x}{dt} = \left(\frac{dB_x}{dt} + k_0\kappa_x E_x\right)\left(\mu_0\mu_{xx}\right)^{-1}, \tag{3.15}$$

$$\frac{dH_y}{dt} = \left(\frac{dB_y}{dt} + k_0\kappa_y E_y\right)\left(\mu_0\mu_{yy}\right)^{-1}, \tag{3.16}$$

$$\frac{dH_z}{dt} = \left(\frac{dB_z}{dt} + k_0\kappa_z E_z\right)\left(\mu_0\mu_{zz}\right)^{-1}, \tag{3.17}$$

and defining the magnetisation of the material based on these equations leads to:

$$H_x = \frac{dH_x}{dt}\left(i\omega\right)^{-1}, \tag{3.18}$$

$$H_y = \frac{dH_y}{dt}\left(i\omega\right)^{-1}, \tag{3.19}$$

$$H_z = \frac{dH_z}{dt}\left(i\omega\right)^{-1}. \tag{3.20}$$

In the above equations, $P_{x,y,z}$ and $B_{x,y,z}$ are the polarisation and magnetic induction of the material along the direction specified in the subscript respectively. $E_{x,y,z}$ and $H_{x,y,z}$ are the electric and magnetic fields acting on the material along the directions in the subscript respectively. ϵ_0 and μ_0 are the permittivity and permeability of free space. k_0 and ω are the free space wave-vector and angular frequency of the incident wave. ϵ_{nm}, μ_{nm} and κ_{nm} are components in the relative permittivity, permeability and chirality tensors of the material, where n specifies the direction in which the exciting field acts, and m is the direction of the material response, as defined in equations 2.4 - 2.6 in section 2.1.3.

The wave equation is calculated based on the modified polarisation and magnetisation, and applied to a region of the model to replicate a chiral medium. The material parameters vary with frequency, but not wave-vector, and can be easily loaded into the model in table form.

3.4 Minimisation

This technique was used in chapters 5 and 6.

Minimisation of a function is used in several instances throughout this thesis. In chapter 5 effective material parameters for layers of chiral media are presented. To find these, analytical predictions of reflection and transmission coefficients for a chiral medium are compared to the reflection and transmission taken from a FEM model, and the difference between these two data sets minimised to find the material parameters. Later in chapter 6, the energy dispersion of a wave on an infinitely long helix is found from the minimisation of a transcendental equation.

There are many methods of minimisation, each with strengths and weaknesses. Typically, we must sacrifice computational time for increased accuracy. Two methods have been used in this thesis - a non-linear least-squares fitting where a global

minimum was easy to find, and simulated annealing for more robust fitting in a large parameter space.

3.4.1 Non-Linear Least Squares Minimisation

We start by considering a set of data $m(x, y)$ that can be described by a function $f(x, \beta)$ that depends on the variable, x, and an unknown parameter, β. We wish to find the value of β for which the function f fits the data set m. We find the residual error between the function and the data set to be $r = m(x, y) - f(x, \beta)$. We minimise the function $S = r^2$ to ensure the value is always positive. When m and f are vectors, this process can be repeated several times for each value of x allowing, for example, dispersive material parameters to be found.

To begin with, a test value of $\beta_{k=1}$ is provided and S is calculated. This test value is adjusted slightly to $\beta_{k+1} = \beta_k + \Delta\beta$ and another value of S is found. A convergence criterion is set to test the minimisation and to determine the end-point:

$$\left| \frac{S_k - S_{k+1}}{S_k} \right| < t \tag{3.21}$$

where t is a specified maximum tolerance and k is the iteration number. This process is repeated until the convergence criterion is satisfied.

This basic technique will work well for simple functions. However in some cases S may begin to diverge rapidly and a solution will not be found without some protection being in place. One method of avoiding divergence, and the method employed throughout this thesis, is the implementation of the Levenberg-Marquardt algorithm. This works by adjusting both the direction and length of the shift vector, $\Delta\beta$, according to the Marquardt parameter, γ. Increasing γ decreases the length of $\Delta\beta$ and points it towards the direction of steepest descent, ensuring that a minimum in S is found.

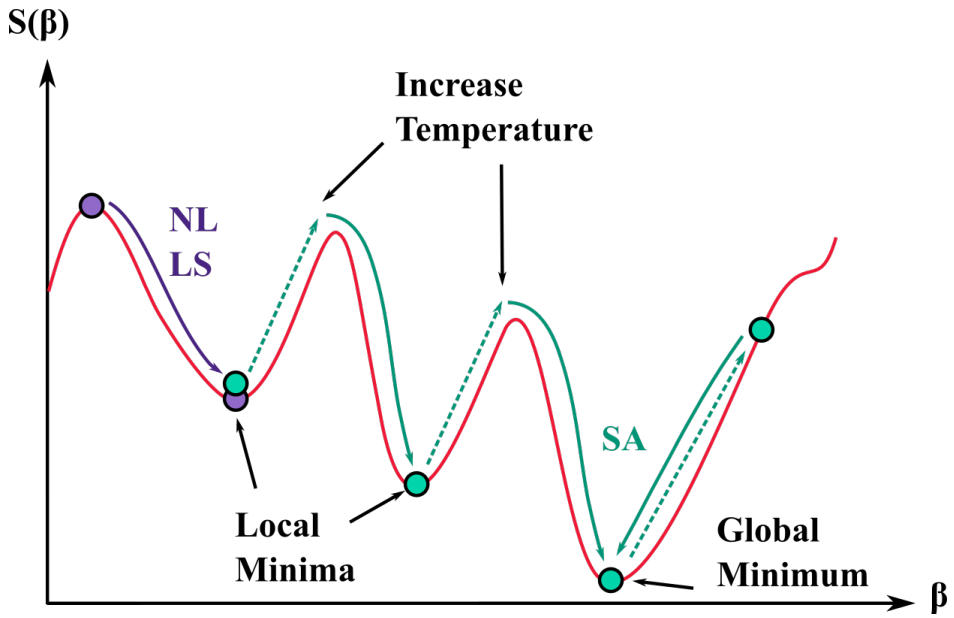

FIGURE 3.11: **Minimising a function using two methods.** A function $S(\beta)$ is to be minimised by selecting the correct value of β. A non-linear least squares method (NL LS, purple) finds a local minimum, however a simulated annealing (SA, teal) is able to escape local minima to find the global minimum thanks to an increase in 'temperature' that causes an increase in the probability of accepting a 'worse' value of β.

3.4.2 Simulated Annealing Minimisation

Unfortunately, finding a minimum of a function is often not enough to really find a solution - we must be sure that it is the global minimum, and not a shallower local minimum. This common problem is illustrated in figure 3.11. A standard non-linear least-squares technique, as described above, is generally not sufficient to find a global minimum unless the initial parameter is very close to the real one. Therefore I have also used a simulated annealing algorithm in some cases.

The method employed is similar to the cooling of atoms in a material into a particular arrangement of the lowest energy. The algorithm accepts an initial guess of the unknown parameter $\beta_{k=1}$, then chooses the shift vector $\Delta\beta$ based on a probability distribution with a scale depending on an input parameter called the temperature, T. It then determines whether the new trial point is better than the last by calculating S. If β_{k+1} is better and S is lower, it becomes the new current value,

as in the non-linear least-squares approach. However, if S is larger there is still a probability that β_{k+1} will be accepted anyway, based on the acceptance function A,

$$A = \frac{1}{1 + \exp\left(\frac{S}{\max(T)}\right)}. \tag{3.22}$$

The probability is smaller for lower temperatures and larger S. The temperature decreases as the algorithm continues to run with a user-specified cooling speed. At set intervals, the temperature is increased, replicating the annealing method used to make the distinctively hard steel in Japanese katanas. The solution is found when the convergence criterion is reached.

This method is more computationally intensive than the standard least-squares minimisation, as many more iterations are carried out. However, by occasionally accepting values that are worse than the current one, the probability of becoming trapped in a local minimum is greatly reduced. This outcome is still possible, and care is taken when interpreting results found from fitting. An added precaution is to ensure that the initial guess sent to the algorithm is close to the correct value, if possible. For example, for smooth functions such as frequency dependent material parameters, the extracted value at one frequency point is used as the initial guess for the following, thus encouraging continuity.

Chapter 4

Pure Optical Rotation from a Twisted-Cross Metasurface

The experimental data presented in this chapter were collected by Ben Tremain at the University of Exeter, and contributed to a chapter in his thesis. The data analysis, simulations, and interpretation were performed by the author.

Introduction

In this chapter the far-field manipulation of chiral electromagnetic waves is studied. The chapter contains a study of the response of twisted-cross metamaterials that provide near dispersionless optical rotation across a broad range of frequencies. Two distinct geometries are compared: first, a bilayer structure comprised of arrays of metallic crosses where the crosses in the second layer are twisted about the layer normal; in the second geometry the lower layer is replaced by an array of cross-shaped holes. Through simulation and experimentation the origin of optical rotatory effects in these two structures are determined. The results are analysed by considering the overlapping electric and magnetic dipoles in the near-fields of the structure, which lead to the observed optical activity in the far-field. This interpretation allows the prediction of the dependence on layer separation.

4.1 Background

Optical rotation is the rotation of linearly polarised radiation associated with the intrinsic chirality of objects [129], and is a phenomenon with important applications in analytical chemistry, biology, and crystallography [82]. Electromagnetic interactions in chiral media can be described by an infinite series of multipolar terms, but in the simple dipole approximation optical rotation arises when electric and magnetic dipole moments (μ_{e} and μ_{m} respectively) of a resonator are parallel and out of phase [14], described by:

$$\Phi \propto \mathbb{I}\left(\mu_{\mathrm{e}} \cdot \mu_{\mathrm{m}}\right) \tag{4.1}$$

and $\mathbb{I}$ indicates the imaginary part of the equation. For optically active molecules, this coupling between the electric, μ_e, and magnetic, μ_m, dipoles is usually very weak, due to a mismatch between the length scales of the molecules and the wavelength of light [14].

Recently, new possibilities have emerged using chiral metamaterials (CMs). The most common embodiment of CMs is a regular array of subwavelength elements ("meta-atoms"), but pairs or groups of achiral elements arranged in a handed configuration to make a "metamolecule" which is chiral have also been considered [129]. Due to their interdependent electric and magnetic responses, these materials can exhibit different refractive indices for right and left circularly polarised radiation, leading to a splitting of transverse modes in the dispersion (which are otherwise degenerate for appropriate geometries). Since this discovery, CMs have attracted a lot of attention as an alternative to the traditional combination of split-ring and dipole resonators for negative refractive index materials [80] and can be used for the design of perfect lenses [130]. Whereas a single layer of 3D chiral elements will intrinsically demonstrate circular dichroism, 2D elements need to be stacked to produce a bulk metamaterial with a similar response. Circular dichroism

and optical rotation can be optimised by modifying the geometry of the meta-atoms forming each layer of the CM, and are typically orders of magnitude stronger than for molecular chiral materials [82]. Several layered structures exhibiting large optical rotation have been proposed that have differing designs: e.g. rosettes [82], gammadions [83] or U-shaped resonators [84] that can be designed for GHz and optical frequencies. One of the simplest cases is a bilayer system with twisted crosses, which shows strong optical rotation and negative refractive index [131–134]. However, the optical activity of all of these designs relies on evanescent coupling between the meta-atoms to yield metamolecules, which typically leads to a highly dispersive optical behaviour [94, 135].

While broadband pure optical rotation is commonly seen in natural media, e.g. sugar solution, thin metamaterials provide much larger optical rotation per wavelength in the material. Recent studies have reported dispersionless optical rotation over a broad frequency range between resonances in studies of bilayer structures formed from arrays with twisted crosses coupled to their complementary cross (c-cross) [85], as well as chiral geometries based on 3D metallic helices [81]. This structure has the added advantage that optical rotation occurs over a frequency range that also exhibits high transmission. Hannam et al demonstrated the optical rotation of a cross coupled to its c-cross embedded in a circular wave-guide [94], while Zhu et al computationally modelled arrays of twisted crosses and c-crosses [85]. While all of these studies found large optical rotations (note that Zhu et al reported an optical rotation of $\sim 164^\circ$, which is equivalent to a rotation of polarisation of $180^\circ - 164^\circ = 16^\circ$), the most striking feature is the broadband nature of the effect. However, a thorough explanation of this phenomenon is currently missing from the literature.

This chapter presents a combined experimental and computational study of optical rotation in different types of twisted cross metamaterials in free space, in order to better understand the phenomenon. Two distinct structures are compared.

Firstly, a bilayer structure comprised of square arrays of metallic crosses separated by a thin dielectric sheet, where the crosses in the second layer are twisted with respect to the layer normal is studied, followed by a second structure where the lower layer is instead an array of twisted c-crosses. It is found that the optical rotation in the cross/cross metamaterials can be understood by considering coupled electric dipole resonances between the two layers that give rise to an operational bandwidth that is strongly dependent on layer separation. In the cross/c-cross structure, meanwhile, the optical rotation occurs in a region between the dipolar mode and a higher order resonance of the cross element. Since modes defining the periphery of the region of optical rotation in the cross/c-cross structure appear intrinsic to the cross layer alone, the bandwidth of optical rotation is found to be relatively independent of layer separation. This gives rise to a broad region of pure, near dispersionless optical rotation, spanning a range from 19.0 GHz to 37.7 GHz, and coinciding with a peak in transmission.

4.2 Cross/Complementary-Cross Metasurface

The schematic of a unit cell of the cross/c-cross chiral bilayer under investigation is shown in figure 4.1 (A), and is similar to that reported in [85]. The metamaterial consists of a double-sided, copper-clad dielectric sheet etched to produce a square array of copper crosses on one side, and an array of cross-shaped holes on the other. The elements in the latter have almost identical dimensions, are aligned with and arranged on the same lattice as the first, but the individual elements are each rotated in the plane about their centre. Etching inconsistencies during fabrication resulted in a discrepancy between the dimensions of the cross and c-cross elements of around 0.05 mm, which has been taken into account in the finite element method (FEM) model. This results in a small shift of resonant frequencies compared to the ideal case described later in section 4.4. The dimensions of the cross/cross bilayer

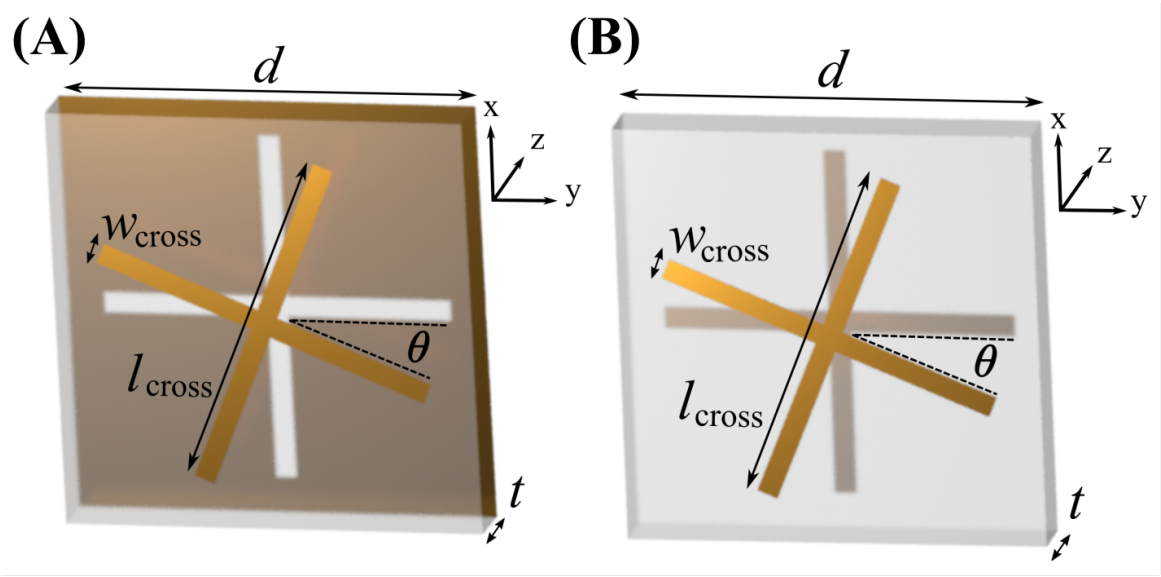

FIGURE 4.1: **Schematics of the unit cells of the two metasurfaces. (A)** shows a unit cell of the cross/complementary-cross metasurface, and **(B)** shows a unit cell of the cross/cross structure. The dimensions are the same for both structures, and are $d = 7.5$ mm, $t = 406\mu$m, $l_{\text{cross}} = 6.60 \pm 0.05$ mm, $w_{\text{cross}} = 0.375 \pm 0.05$ mm and $\theta = 22.5°$.

sample, shown in figure 4.1 (B), and discussed section 4.3, are identical to those of the cross/c-cross, and the effects of over-etching are neglected. The thickness of the dielectric is 0.406 mm with permittivity, $\epsilon_d = 3.02(1 + 0.02i)$. The lattice spacing is $d = 7.5mm$, the length and the width of the crosses are $l_{cross} = 6.60 \pm 0.05mm$ and $w_{cross} = 0.375 \pm 0.05mm$, and the rotation angle is $\theta = 22.5$ deg. The sample is formed by 50 unit cells in the x-direction and 50 in the y-direction, although in the FEM model the array is assumed to be infinite in both directions.

The circularly polarised transmission coefficients are obtained by measuring the four linear, complex transmission coefficients (t_{xx}, t_{xy}, t_{yy}, and t_{yx}). In the experimental set-up, linearly polarised microwave radiation impinges at normal incidence upon the sample from a rectangular waveguide horn antenna, and the transmitted beam is collected by a second rectangular horn. Both antennas are connected to a vector network analyser and can be azimuthally rotated by 90° to permit the polarisation-dependent measurements required. More details on the experimental

technique can be found in section 3.2.2. The simulations are performed using a FEM model (ANSYS® HFSS™) with one unit cell and periodic conditions in the x- and y-directions. Floquet ports are employed in the model, and the complex transmission coefficients are obtained from these ports. For more details on the simulation see section 3.3.2. The circular transmission amplitude coefficients for each polarisation can be calculated from the complex linear transmission coefficients [134] using

$$T_{+/-} = \frac{t_{xx} + t_{yy} \pm i\left(t_{xy} - t_{yx}\right)}{2} \tag{4.2}$$

where the subscript on denotes right (+) or left (-) circular polarisations, which correspond to the + or – sign in the expression respectively. The optical rotation, ϕ, and the ellipticity, η, are defined respectively as

$$\phi = \frac{\arg\left(\tau_{+}\right) - \arg\left(\tau_{-}\right)}{2} \tag{4.3}$$

and, assuming there is no polarisation conversion,

$$\eta = \frac{|\tau_{+}|^2 - |\tau_{-}|^2}{|\tau_{+}|^2 + |\tau_{-}|^2} \tag{4.4}$$

In figure 4.2 (A) the experimental amplitudes of the left and right circular polarisation transmission coefficients (green and blue circles) are compared with numerical simulation (black line). Good agreement between theory and experiment is observed, with a maximum transmission coefficient of 0.86 at 9.8 GHz. A second maximum occurs at 24.0 GHz, bounded by two transmission minima at 17.2 GHz and 34.2 GHz. Figure 4.1 (B) shows the predictions of the ellipticity of transmitted radiation from the FEM model. The extrema in ellipticity arise from the small difference between the left and right circularly polarised transmission intensities near the transmission minima (arrows in figure 4.1 (A)). Note that the experimental

results for ellipticity are not plotted, as the signal to noise ratio is poor when measuring near zero transmission close to a resonance. An important point to note is that when losses are removed from the permittivity of the dielectric layer the peaks in ellipticity disappear, as ellipticity arises from a difference in absorption for right- and left-circularly polarised (R/LCP) radiation, which vanishes when losses are removed.

The optical rotation, obtained via the phase measurements using equation 4.3 is shown in figure 4.2 (C). In the frequency region between the transmission minima there is a region of broad, near dispersionless optical rotation, marked as the shaded regions. This is a key result that will be considered in the remainder of the chapter. As discussed in [85, 134], broadband optical rotation accompanied by near-zero ellipticity is rather unusual. Moreover, the region of dispersionless optical rotation ($\sim 19^{\circ}$) is bound by the transmission minima associated with two resonances of the system (marked by arrows in figure 4.2 (A)). It is the nature of these resonances, and how they define the behaviour of the structure, that will be analysed in the discussion below.

4.3 Cross/Cross Metasurface

In order to determine the underlying mechanism behind the broadband optical rotation, the optical rotation arising from a more conventional twisted cross/cross array is first considered. Figure 4.3 (A) shows the transmitted intensities of LCP and RCP radiation through a metamaterial comprised of left-handed metamolecules (defined as having an anticlockwise rotation from top to bottom crosses), calculated using a FEM model. Two resonant modes are present at 22.5 GHz and 24.6 GHz. These resonant frequencies are defined by transmission minima, as expected for an array of unconnected metallic antennas [136]. Each resonant dip in the transmission leads

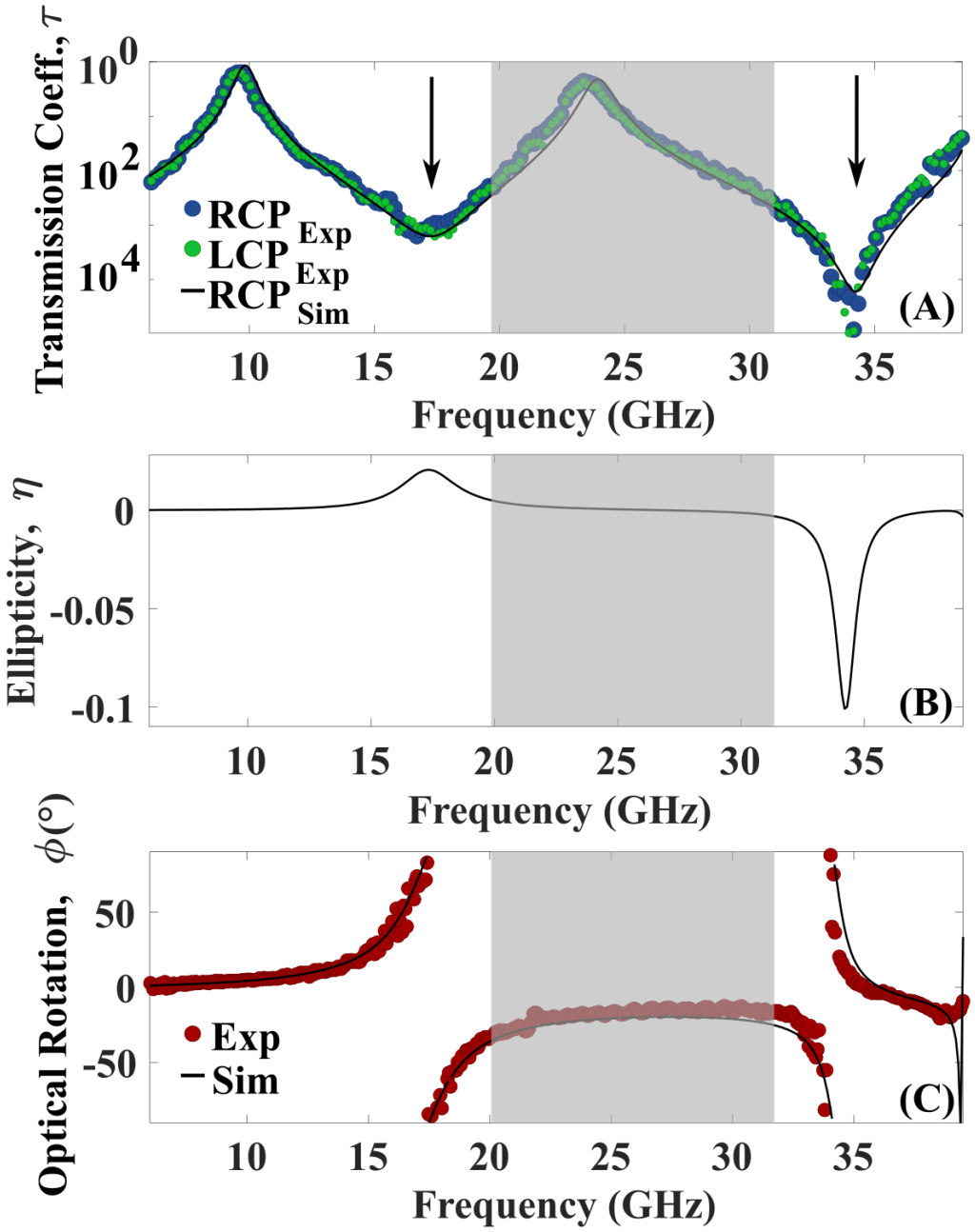

FIGURE 4.2: **Experimental measurement of the cross/complementary-cross structure.** **(A)** shows the experimental transmission of right and left circularly polarised waves through the array (blue and green circles), compared to the simulated transmission for right circularly polarised waves (black line). It almost perfectly overlays the left circularly polarised, except at the resonant transmission minima indicated by black arrows.**(B)** is the simulated ellipticity. The measured ellipticity is not included as the transmission intensity is too low to give reliable experimental results. **(C)** is the measured (red circles) and simulated (black line) optical rotation. The grey shaded region highlights the frequency range where pure optical rotation is observed away from regions of large ellipticity.

to a peak in the optical ellipticity in figure 4.3 (B) and optical rotation in figure 4.3 (C).

It is possible to characterize the nature of these resonant modes by considering the currents flowing in the arms of the crosses at these frequencies. The currents found from a FEM model at the two resonant frequencies are plotted in figure 4.4. Strong currents flow in the cross arms that are parallel to the incident electric field, indicated by the black arrow. For the two different resonant frequencies the currents have a single maximum at the mid-length of the arms. This is characteristic of an electric dipole resonance of a cross. For the lower frequency mode, the current direction at any point in the phase cycle is the same in the upper and lower cross (i.e. the currents are in phase.), while for the upper frequency mode, the currents in the two layers point in opposite directions (i.e. they are out of phase). The resonances can be referred to as the symmetric (22.4 GHz) and antisymmetric (24.6 GHz) resonances of the coupled cross system.

Chiral interactions such as circular dichroism and optical rotation arise due to multipolar interactions normally dominated by the alignment of magnetic and electric dipole moments (equation 4.1) [84]. From the classical viewpoint this means that the electric field of the incident radiation can induce a parallel magnetic dipole moment in the structure, and the magnetic field of the incident radiation can induce a corresponding parallel electric moment. While the materials that form the cross/cross meta-atoms are themselves non-magnetic, an effective magnetic dipole can be generated by the coupled electric dipoles in the top and bottom layers, giving rise to a current loop (completed by displacement currents in the dielectric). These current loops are illustrated in figure 4.4 (C) and (D).

For the higher frequency, antisymmetric dipole resonance, the origin of the magnetic dipole moment is relatively easy to understand, and is illustrated in figure 4.4 (D). Following the interpretation of Kenanakis et al [137], the displacement fields link the ends of the upper cross arm with the ends of the lower cross arm, forming

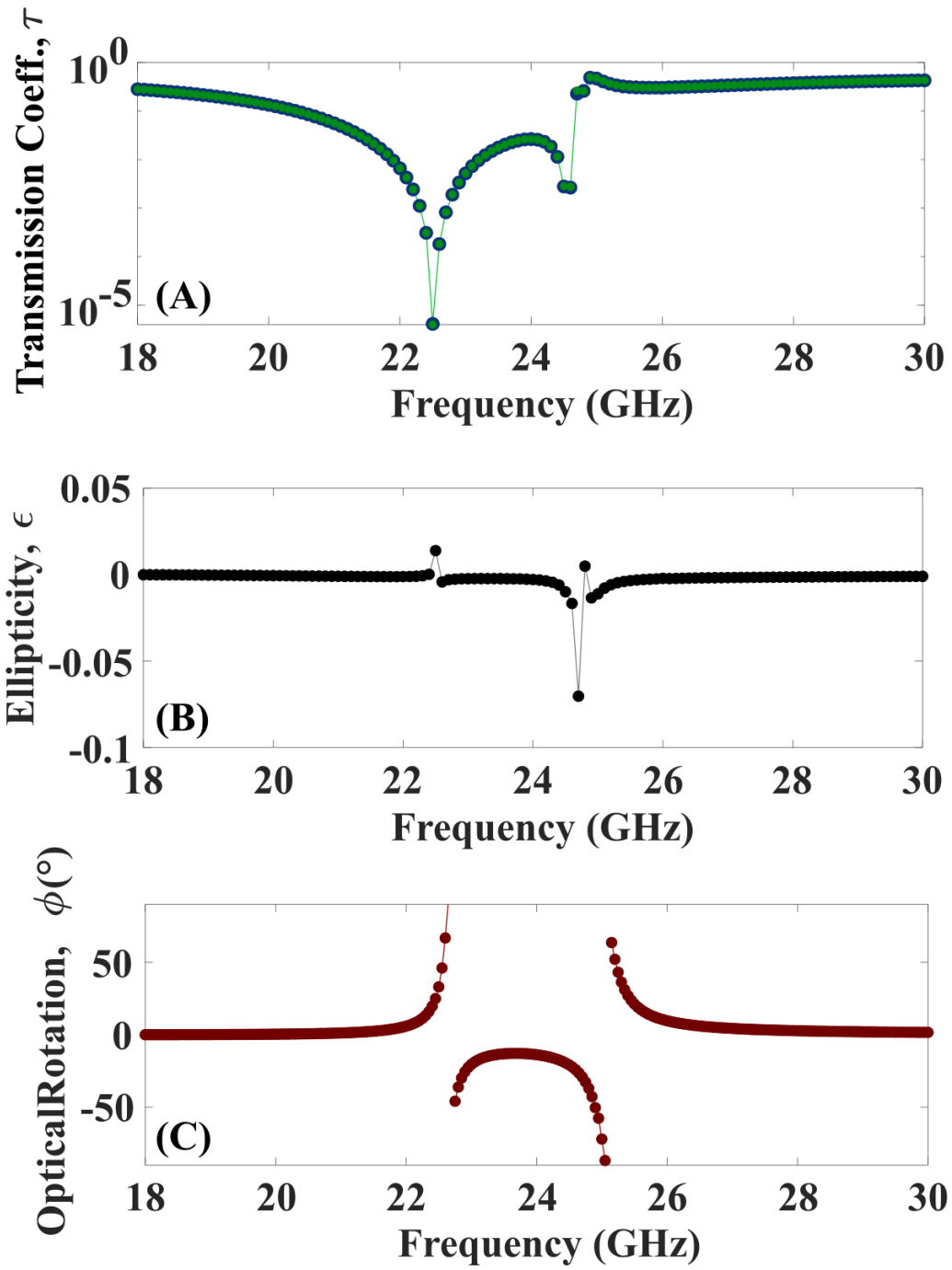

FIGURE 4.3: **Simulated demonstration of pure optical rotation from a cross/cross metasurface.** **(A)** shows the transmission of circularly polarised waves through the array on a logarithmic scale. Resonant modes are seen at 22.4 GHz and 24.6 GHz. **(B)** is a plot of the ellipticity and **(C)** is the optical rotation of the transmitted wave.

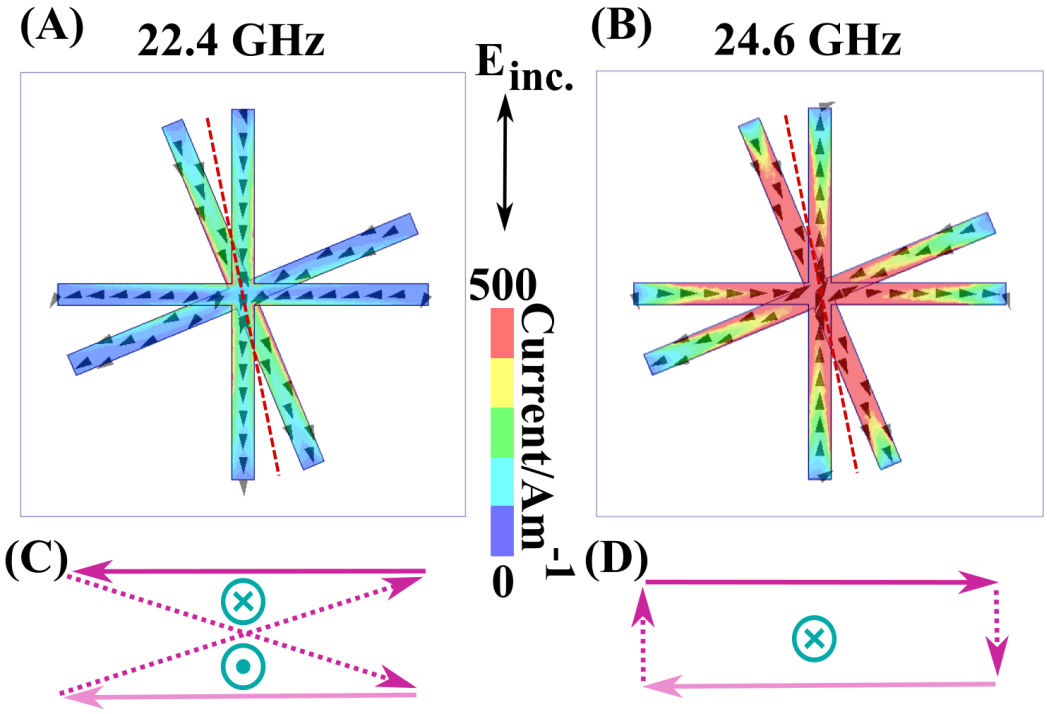

FIGURE 4.4: **Currents in a unit cell of the cross/cross array. (A)** shows the simulated current density (colour) and direction (dark grey arrows) at the first resonant frequency under vertically polarised illumination. **(C)** is a simplified illustrative schematic of the electric dipoles (solid pink arrows), magnetic dipoles (teal arrows) and displacements currents (dotted pink arrows) found in the vertical arms of the top (darker arrows) and bottom (lighter arrows) cross, in a plane showing a cross-section through the structure, with the top of the plane indicated by the dashed red line in **(A)**. **(B)** and **(D)** show the same plots for the higher resonant frequency. These plots of the currents and dipoles show the symmetric and antisymmetric natures of the first and second resonances respectively.

current loops. This gives rise to a single magnetic dipole moment with a direction lying in the plane of the sample. In un-rotated cross/cross structures (which have mirror symmetry) this magnetic dipole lies perpendicular to the electric dipoles of the crosses, and, according to equation 4.1, optical rotation due to this mode will be zero. However, when one cross is twisted with respect to the other, partial alignment of the electric and magnetic dipoles occurs, leading to the onset of optical rotation. For the symmetric (lower frequency) mode, one might expect no optical rotation, since the currents are parallel in the arms of the two crosses. However figure 4.3 (C) shows that there is optical rotation resonance associated with this mode. Here, displacement currents between upper and lower crosses create a figure-of-8 current loop (see figure 4.4 (C)), which can be thought of as two counter-rotating loops, each with an associated magnetic moment. Without a twist between upper and lower crosses these magnetic moments are anti-parallel and hence cancel. However, a rotation of one cross with respect to the other results in a net magnetic dipole moment which is parallel to the net electric dipole moment, again satisfying equation 4.1, and resulting in optical rotation. The net magnetic moments are illustrated in the 3-dimensional schematics in the bottom panels of figure 4.4 (C) and (D).

In each case, the sign of optical rotation is determined by the sign of the phase difference between electric and magnetic moments, i.e., if the electric moment leads the magnetic moment in phase, the optical rotation will be positive or right-handed in nature, while if the magnetic moment leads the optical rotation will be negative and described as left-handed. On approaching the symmetric, lower frequency resonance, the optical rotation is positive. At the resonance, the transmission drops to almost zero and the currents in the top and bottom arms of the cross undergo a sharp 180° phase change; the handedness of the optical rotation reverses, as now the magnetic moment is leading the electric moment by 90°. However, as seen in figure 4.3, the sense of optical rotation and ellipticity are reversed at the upper and

lower frequency modes, meaning that the direction of polarisation rotation is reversed. This gives rise to a frequency band between the two resonances where the optical rotation does not change sign. This observation provides a key insight into the conditions necessary in such a system for pure optical rotation (i.e., without ellipticity) to be observed. In the following section the reasoning outlined above will be applied to the complementary case of a cross/c-cross structure.

4.4 Discussion

4.4.1 The Origins of Pure Optical Rotation

Replacing the lower cross layer with its complement (cross shaped holes in a continuous metal sheet) has been shown to result in similar dispersionless optical activity [94]. While one might expect the underlying mechanism behind this optical rotation to be the same as that for the cross/cross structure, the pair of resonances involved are of a fundamentally different nature.

In figure 4.5 (A) the circularly polarised transmission spectra for the cross/c-cross structure are plotted. In addition to transmission minima associated with resonances of the crosses, marked by vertical dark grey lines, there are now also transmission maxima at the frequencies marked by the vertical light grey lines. For ease of interpretation, the discrepancy in upper and lower element size due to fabrication errors is neglected in this model. Transmission maxima are a characteristic feature of arrays of apertures in a conducting sheet [138], and are therefore primarily associated with resonances of the complementary cross layer. Figure 4.5 (B) shows the transmitted phase of LCP and RCP radiation through the double layer system in the

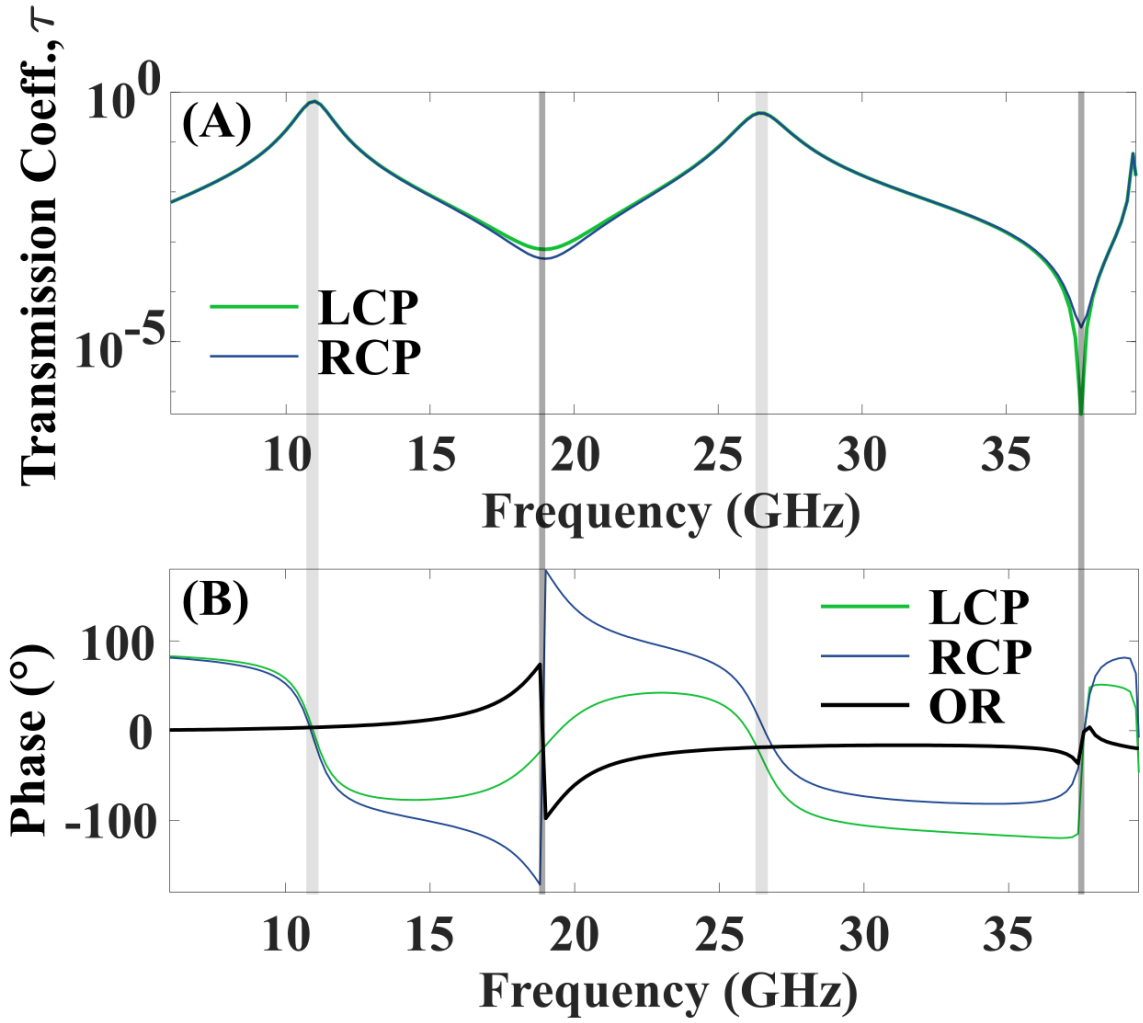

FIGURE 4.5: **Investigation into wideband pure optical rotation on a cross/complementary-cross structure. (A)** shows the transmission of circularly polarised waves, and in **(B)** the phase of the corresponding waves is plotted in thin coloured lines. The thick black line is the optical rotation of the wave upon transmission through the array, which is the difference in phase of left and right circularly polarised waves. Vertical light grey lines indicate resonant peaks in transmission and dark grey lines indicate resonant transmission dips.

thin blue and green lines. Similarly to the cross/cross system, the band of dispersionless optical rotation in figure 4.4 (B) is bound by two resonant minima, each rotating the polarisation plane in opposite directions. It should be noted that discontinuities in phase near transmission minima is a phenomenon widely observed in optics and plasmonics [139]. However, phase discontinuities at transmission minima play a particularly important role in chiral media: Gorkunov et al. recently showed that transmission minima in chiral metamaterials can give rise to very strong circular dichroism and optical rotation, which must be accounted for in Kramers-Kronig relations by including so-called Blaschke terms [27].

Currents found from the FEM model at the dips in transmission can be used to characterise these resonances. Figure 4.6 (A) shows that the lower frequency resonant minimum is associated with the dipolar excitation of the upper cross. However, because we have removed the second cross from the unit cell, replacing it with the complementary layer, one does not expect a higher frequency antisymmetric dipole resonance, as was the case for the cross/cross above. Instead, the second minimum in transmission is associated with a higher order excitation of the cross, as seen in the current plots in figure 4.6 (B). This is the linear quadrupole moment of the arm of the cross aligned to the incident polarisation.

4.4.2 Comparison of Solid and Complementary Structures

One of the major differences between the cross/complementary-cross structure, and the cross/cross, is the presence of the lower conducting layer. The image currents in this layer, which always are out of phase with the current in the upper cross, result in an "antisymmetric" nature to the current distributions at all resonances of the cross/c-cross structure, as seen in figure 4.6. In analogy to the cross/cross system, these distinct current distributions lead to the formation of current loops

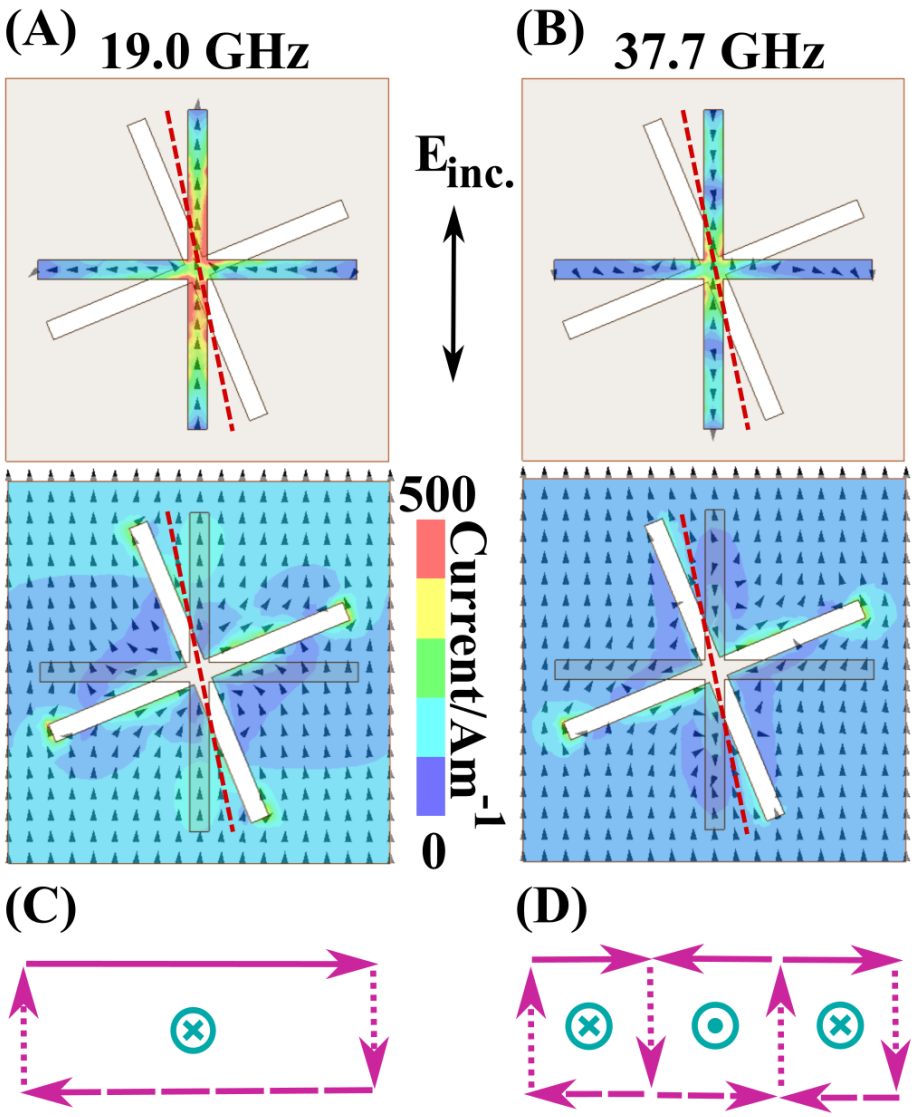

FIGURE 4.6: **Currents and dipoles in the cross/complementary/cross structure.** **(A)** and **(B)** show the surface current density (colour) and direction (dark grey arrows) in the top surface at the first and second resonant dips in transmission. Beneath are the equivalent plots for the bottom surface of the array. **(C)** and **(D)** are illustrative schematics of the electric (pink arrows) and magnetic (teal arrows) dipole moments in a plane showing a cross-section through the structure, with the top of the plane indicated by the dashed red line in **(A)** and **(B)**. Dotted pink arrows represent the displacement currents in the dielectric, and dashed arrows indicate image dipoles in the bottom conducting surface.

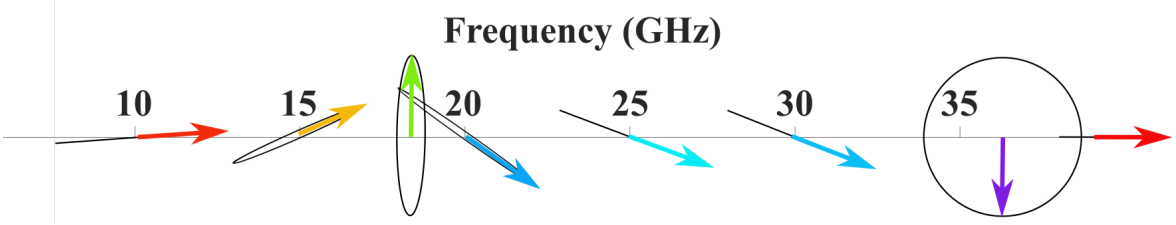

FIGURE 4.7: **Polarisation ellipses for the beam transmitted through the cross/complementary-cross array as a function of frequency.** Black ellipses represent the degree of ellipticity in the transmitted beam, multiplied by 10 for the purposes of clarity. Straight black lines mean a linearly polarised wave. Arrows represent the angle of polarisation, with an un-rotated beam being horizontal. The colours of the arrows also show the degree of optical rotation.

between upper and lower elements and their associated magnetic moments, illustrated in figure 4.6 (C) and (D). In rotated cross/c-cross structures, the presence of the c-cross in the lower sheet perturbs the image currents, yielding rotated fields, and resulting in electric and magnetic moments with parallel components, thus satisfying the condition for optical rotation. Similar to the cross/cross system, there is competition between resonances that act to rotate the plane of polarisation in opposite directions, giving rise to the region of pure optical rotation between the resonant minima. The pure optical rotation coincides with a region of high transmission that is narrower than the band of rotation, however this is still a marked improvement on the cross-cross structure where the transmission is much lower across the band of pure OR. Figure 4.7 shows the polarisation ellipses associated with the wave transmitted through the cross/c-cross array, which illustrates the interaction between resonances of opposite handedness. In contrast to the cross/cross case, this region of pure optical rotation coincides with a resonant maximum in transmission. This highlights a distinct advantage of the cross/c-cross geometry over those studied in [84, 131–133], the latter intrinsically characterised by enhanced reflection (and reduced transmission) associated with the closely spaced resonances of the disconnected bilayer arrays.

4.4.3 Dependence on Separation

We have seen that the optical rotation in cross/cross and cross/c-cross metamaterials has fundamentally different origins. To summarize: in the cross/cross system, electric dipoles in the upper and lower crosses couple together, forming a symmetric and an antisymmetric pair that define the two transmission minima. In the case of the cross/c-cross, the transmission minima are characterised by the dipolar and linear quadrupolar modes of the cross. Since the transmission minima in the cross/c-cross structure appears intrinsic to the cross layer alone, and not based on the strong coupling between resonances in top and bottom layers, the bandwidth of optical rotation should be relatively independent of layer separation.

In order to examine this effect further, numerical modelling of the optical rotation from both systems as a function of layer separation (figure 4.8 (A) and (B)) was carried out. Figure 4.8 (C) illustrates the frequencies of the asymptotes in optical rotation for cross/cross (filled) and cross/c-cross (unfilled) structures with various thicknesses of dielectric. It is clear that the bandwidth of the pure optical rotation for the cross/cross is significantly smaller than that of the cross/c-cross for most separations. Only for very small separations do they become comparable. The magnitude of optical rotation, shown in figure 4.8 (D), for the cross/c-cross is also considerably larger, except for the largest layer separations. In this case the large optical rotation for the cross/cross system with large layer separation is somewhat artificial, as the bandwidth is so narrow leading to a frequency overlap of the resonance modes and strong dispersion in the optical rotation. For the cross/c-cross, the magnitude of optical rotation is less dependent, in relative terms, on layer separation. Moreover, the bandwidth of the cross/c-cross is only weakly dependent on separation. Although the interaction between the upper cross and the lower conducting sheet is necessary for the presence of optical rotation, it clearly plays a minor role in determining the resonant frequencies of the modes. In the end it is the resonant

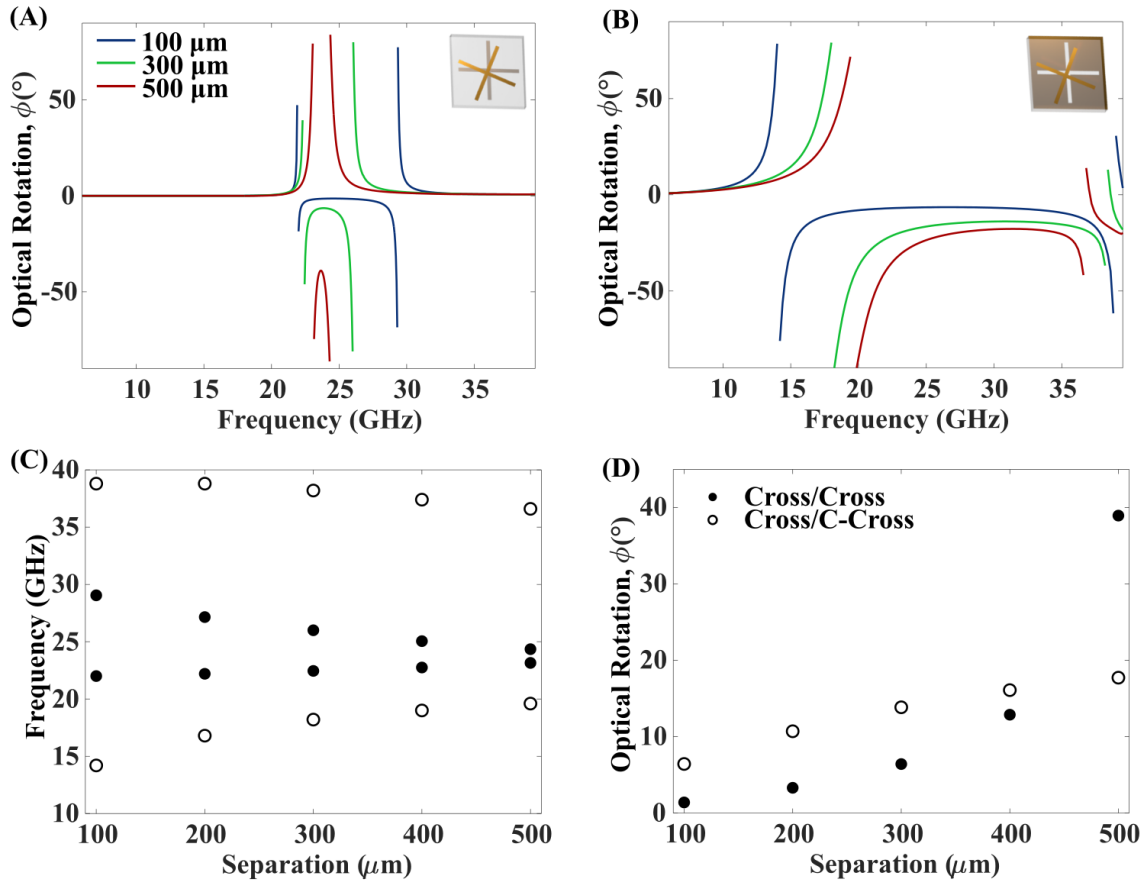

FIGURE 4.8: **Simulated demonstration of the change in optical rotation on increasing the separation of top and bottom layers. (A)** is the simulated optical rotation for a cross/cross array (inset) with dielectric thicknesses of 100 μm to 500 μm. **(B)** shows the simulated optical rotation for the cross/complementary-cross (inset) for equivalent thicknesses of dielectric. **(C)** is a plot of the upper and lower frequencies of the asymptotes in optical rotation for cross/cross (filled) and cross/complementary-cross (unfilled) arrays. **(D)** shows the minimum pure optical rotation within the asymptotes given by the cross/cross (filled) and cross/complementary-cross (unfilled) arrays for a range of separations.

frequencies that determine the bandwidth of the effect. Overall, this gives rise to chiroptical behaviour of the cross/c-cross which is much less sensitive to changes in the separation between upper and lower layers. These differences in the behaviour of the two systems highlight the diverse origins of the pure optical rotation exhibited by both. In addition, this insight provides useful information for the selection of parameters for a variety of applications. If moderate optical rotation is required over a wide range of frequencies, the cross/c-cross is the most appropriate structure; however to achieve very large values of optical rotation a cross/cross structure is more suitable, although compromises in the bandwidth and transmitted intensity must be made.

4.5 Conclusions

In summary, the optical rotation in twisted cross metamaterials has been studied, and two distinct cases compared: a bilayer structure comprised of arrays of metallic crosses where the crosses in the second layer are twisted (cross/cross), and the case where the second layer is instead an array of complementary crosses (cross/c-cross). In both structures, pure optical rotation occurs in a frequency band between two transmission minima, where alignment of electric and magnetic dipole moments occurs. In the cross/cross metamaterial, the transmission minima occur at the symmetric and antisymmetric resonances of the coupled crosses. In contrast, the optical rotation region in the cross/c-cross structure is bounded by transmission minima associated with the dipole and quadrupole modes of the cross. Since the frequencies of transmission minima in the cross/c-cross structure appear intrinsic to the cross layer alone, the bandwidth of optical rotation is found to be relatively independent of layer separation. In the transmission through a cross/c-cross bilayer, a broad region of pure, near dispersionless optical rotation spanning a range from 19.0 GHz to 37.7 GHz is found in a region of maximum transmission. These results highlight

that chiral metamaterials that also include the complement to the conducting element in the unit cell (such as the cross/c-cross structures) are better candidates for optical rotatory materials in the transmission geometry.

Chapter 5

Probing Chiral Media with Chiral Electromagnetic Near-Fields

The sample fabrication, experimental measurements, data analysis, simulations and interpretation presented in this chapter were performed by the author.

Introduction

This chapter focuses on evanescent chiral near-fields, and their interaction with chiral materials where multipolar interactions are allowed or suppressed. The idea of "superchiral" fields is investigated through a microwave analogy to a chiral plasmonic bio-sensor. An array of small metal helices replicate the chiral molecules, and GHz range planar-chiral antennas act as a source of evanescent chiral electromagnetic fields. The interaction between the fields and the helices is measured, and compared to the interaction with an effective medium approximation. The dependence on separation between antennas and helices is also studied.

5.1 Background

Throughout nature there are countless objects and systems that are chiral; from simple amino acids, to the complex proteins they constitute. These objects can exist in two states (enantiomorphs) of opposite handedness, where one enantiomer is the mirror image of the other. Handedness is fundamental in determining how a molecule will interact with its environment, and there are numerous examples of biologically inert or beneficial molecules with an "evil twin" [51]. The ability to distinguish between different enantiomers is therefore of paramount importance, for example, for safe and efficient drug production.

One of the few ways to distinguish enantiomers is through their differing chiroptical interactions with chiral electromagnetic (EM) fields, such as in circular dichrosim (CD). These investigations become particularly interesting in regions outside the dipolar regime, i.e., when one can no longer assume that molecules are sub-wavelength and act as dipoles under plane wave excitation. Several recently published papers report a large enhancement (up to 6 orders of magnitude) in the strength of chiroptical interactions involving biomolecules on chiral plasmonic structures [33, 59, 60, 140] and in the nodes of chiral standing waves [34]. It has been proposed that these strengthened interactions are mediated by "superchiral" fields, and allow more sensitive detection and efficient selection of chiral molecules, and even indicate their hierarchical structure [52]. However, the nature and origin of this enhancement remain difficult to decipher [60, 62, 141] because many factors come in to play in these complex systems, and spin and orbital angular momenta are not well defined [47, 142, 143]. There are also several measures of chirality that may be employed [144–146], further complicating analysis.

One proposed interpretation of the observed chiral enhancement in the vicinity of nanoparticles has its origins in multipolar contributions to the chiroptical interaction [33], originating from spatial gradients in the electric field [32]. Normally

multipolar contributions can be ignored, as they are origin dependent and average to zero within the random dipole approximation (where the constituent molecules are small and randomly oriented). However, for a surface composed of resonant plasmonic antennas, which give rise to very large spatial gradients in the fields, the contribution from such terms to the strength of a chiral interaction with adsorbed molecules remains unclear [13, 35, 36, 61]. A more complete discussion of this topic can be found in section 2.1.5.

In this chapter I investigate how chiral EM near-fields interact with helical "meta-molecules". The chiral fields are generated by illuminating a staggered pair of rod antennas with GHz radiation [147], while very subwavelength metallic helices act as the molecules. It is thought that multipolar, non-local contributions can be significant when the EM field changes on a length scale comparable to the size of the chiral element [148, 149], as is the case in the strongly evanescent chiral near-fields studied here. The experiment is designed to test whether contributions to the chiral interactions exist that are not predicted by models that assume an effective homogeneous chiral medium, i.e., one where there are no discrete chiral elements of a size comparable to the wavelength scale. However it is discovered that the strength of this chiral interaction can be predicted using an effective medium approximation, describing the helical layer with wave-vector independent permittivity, permeability and chirality material parameters. This indicates that multipolar chiral effects do not contribute significantly to the chiroptical interaction in the near-field.

5.2 Chiral Near-Field Antenna Array

Throughout this work the definition of EM chirality introduced by Tang and Cohen [12] will be followed. Here they define the chirality of a time varying EM field as the time-even pseudo-scalar (i.e. the direction reverses under parity inversion but not time reversal, but otherwise acts as a scalar),

$$C = -\frac{\epsilon_0 \omega}{2} \mathbb{I}\left[\tilde{\mathbf{E}}^* \cdot \tilde{\mathbf{B}}\right] \tag{5.1}$$

where $\tilde{\mathbf{E}}$ and $\tilde{\mathbf{B}}$ are complex electric and magnetic fields respectively, and ω is the angular frequency. In other words, the chirality of a field is proportional to the product of parallel components of the electric and magnetic fields that have a $\pm\frac{\pi}{2}$ phase difference. The chirality of a circularly polarised wave, assuming unit intensity, is therefore $C_{\mathrm{CP}} = \pm\omega\epsilon_0|E_0|^2/2c$, where the $\pm$ correspond to right and left handed waves. This definition is used to design antennas that generate chiral fields on resonance.

5.2.1 Experimental and Simulated Spectra

Consider the fundamental resonance of a half wavelength rod antenna: on resonance, a current maximum (and corresponding maximum in magnetic field) is found at its mid-length, while the electric field is concentrated at both ends of the rod. Though rod antennas do not possess chiral symmetry by themselves, one can arrange them in two-dimensional chiral ensembles by staggering them [147]. To obtain a strong overlap between the electric and magnetic field regions, they can be arranged in pairs as shown in figure 5.1 (A): for this arrangement, and because of the fixed ($\pm\frac{\pi}{2}$) phase relationship between electric and magnetic fields of the eigenmodes of the staggered geometry, a chiral EM field is generated at the centre of the unit cell. The nature of this field differs from that of circularly polarised waves, in that the EM chirality decays quickly in space. This is illustrated in figure 5.1 (A), which shows the chiral density of the EM field above and below one unit cell of the array as calculated using equation 5.1. This large spatial gradient in the field, in principal, should allow coupling to multipolar modes of an object in the vicinity of the field, as it contains high wave-vector components.

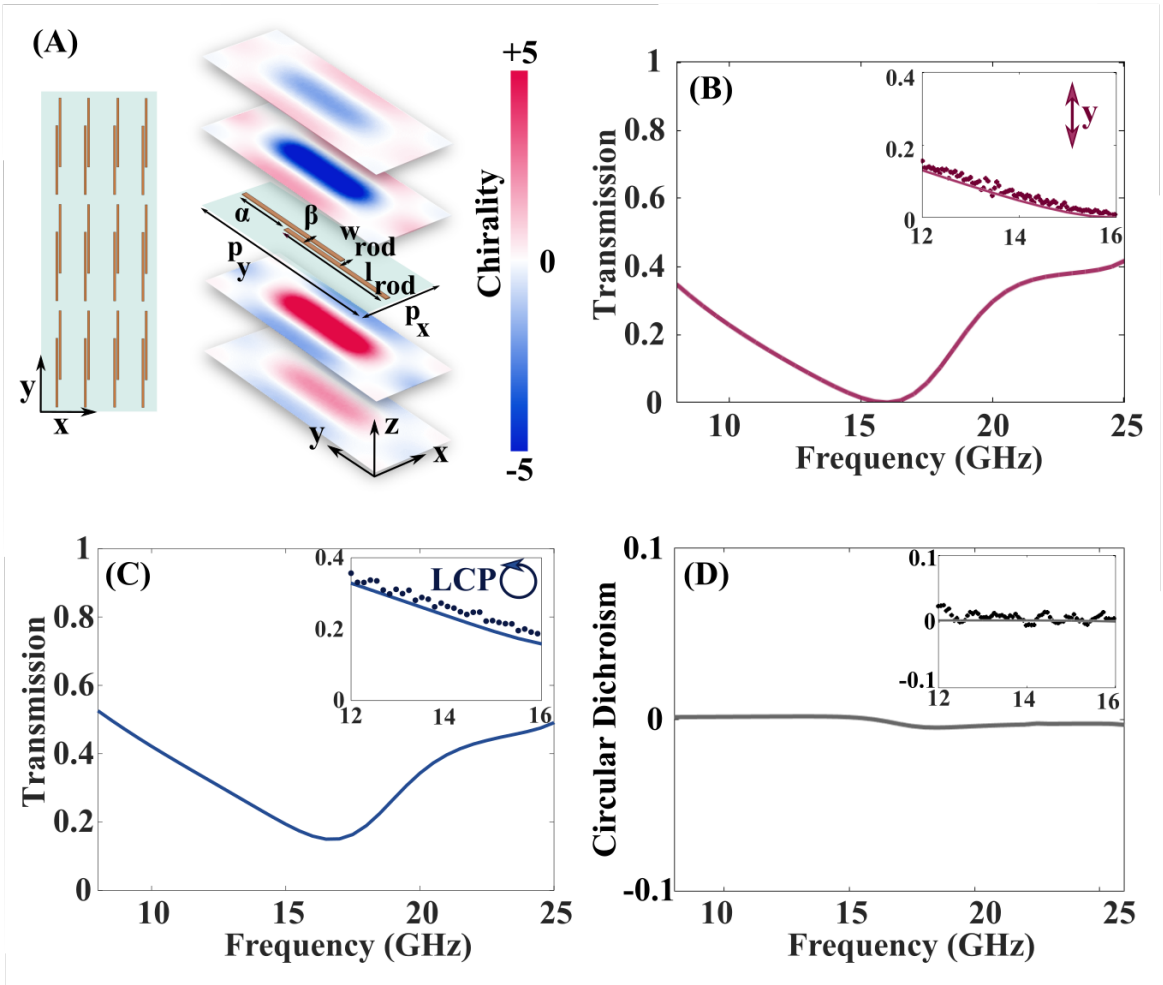

FIGURE 5.1: **Simulated and experimental spectra of the staggered-rod array. (A)** Schematic of the staggered-rod antenna array, with surface plots on the right illustrating the chirality of the modelled fields 0.4 mm and 0.8 mm above and below a unit cell at the resonant frequency of 16 GHz, normalised to a circularly polarised plane wave; dimensions are $\alpha = 2.6$ mm, $\beta = 300$ μm, $p_x = 3$ mm, $p_y = 9.1$ mm, $l_{rod} = 6.4$ mm, $w_{rod} = 200$ μm; the rods have a thickness of $\beta = 35$ μm. **(B)** Finite element method (FEM) model predictions of the transmission of linearly polarised radiation through the staggered rod array, with polarisation along the rod axis (y-polarised); inset shows comparison between experimental (circles) and simulated (line) transmission in the frequency region of interest. **(C)** FEM modelled transmission of left circularly polarised radiation through the staggered rod array; inset shows the comparison between experimental (circles) and simulated (line) transmission in the frequency region of interest. **(D)** FEM predictions of the circular dichroism (CD) of the staggered rod array; inset shows the comparison between experimental (circles) and predicted (line) CD in the region of interest.

Figure 5.1 (B) shows the transmission spectrum of the staggered-rod array; both experimental data and the results of a finite element method (FEM) model (calculated using COMSOL Multiphysics®). (Note the frequency range of the presented data is limited by the parameter extraction technique, explained below.) A resonant dip in the intensity of transmission at 16 GHz, where the wavelength is roughly equal to twice the length of one rod, is evident when the polarisation of the incident electric field is parallel to the major rod axis. At this resonance the fields around the antennas satisfy the definition in equation 5.1 and the chirality of the near-fields is strong. Hence it is this region (and below, as the resonance shifts to lower frequencies upon placing a higher index material next to the antenna array) that will be the focus of the rest of this chapter. The circular transmission coefficients τ can be calculated from the four complex linear transmission coefficients t, using the equations,

$$\tau_{\pm\pm} = \frac{t_{xx} + t_{yy} \pm i\left(t_{xy} + t_{yx}\right)}{2}, \tag{5.2}$$

$$\tau_{\pm\mp} = \frac{t_{xx} - t_{yy} \mp i\left(t_{xy} - t_{yx}\right)}{2}. \tag{5.3}$$

The first subscripts on τ and t denote incident polarisation (right (+) and left ($-$) handed circular polarisations, or x and y linear polarisations), the second subscript is the detected polarisation. These are used in the calculation of circular dichroism (CD). Since circular polarisation conversion is a signature of anisotropy, not chirality, these contributions are ignored and only the conserved circular polarisation components in the calculation are considered:

$$CD = \frac{|\tau_{++}|^2 - |\tau_{--}|^2}{|\tau_{++}|^2 + |\tau_{--}|^2}. \tag{5.4}$$

Figure 5.1 (D) shows the CD of the staggered-rod antenna array obtained from both

the FEM model and the experimental measurements. With the extremely subwavelength thickness (35 μm) of the antenna array, its CD is small but non-zero due to the presence of the substrate that breaks the out-of-plane symmetry.

5.2.2 Helical Fourier Transform

The hypothesis presented here is based on the fact that the chiral fields generated by the staggered rod antennas contain high wave-vector components. Taking the Fourier transform (FT) of these fields shows the spread in wave-vector of the evanescent field when excited at a particular frequency. It is possible to decompose the results of this analysis to show the wave-vectors with right and left circular polarisation (R/LCP), as plotted in figure 5.2. The derivation of the equations used in this decomposition can be found in appendix A.

Figure 5.2 (A) and (B) show the Fourier amplitude as a function of wave-vector of the electric field in a plane 0.1 mm above a unit cell of a right-handed staggered-rod antenna array with no substrate. Several conclusions can be drawn from studying these plots. Firstly, the fields that are scattered perpendicular to the rods have much higher wave-vector components than those along the major axis of the rods, as expected. Secondly, the FT of the fields shows the same 2-fold rotational symmetry as the rods themselves. Comparing the LCP components of the FT to the RCP components, there is a net EM chirality in the fields. The difference between RCP and LCP FT components (the FT dissymmetry), plotted in figure 5.2 (C), illustrates this clearly. In figure 5.2 (D) the FT dissymmetry is plotted in a plane 0.1 mm below the staggered-rod array, and shows that the net EM chirality of the field is equal and opposite on opposite sides of the array. The most important thing to note is that, as suggested by the plots of EM chirality in figure 5.1 (A), the fields around the rods have some chiral components with high wave-vectors. These components have been proposed to contribute to higher order terms in the description of a chiral

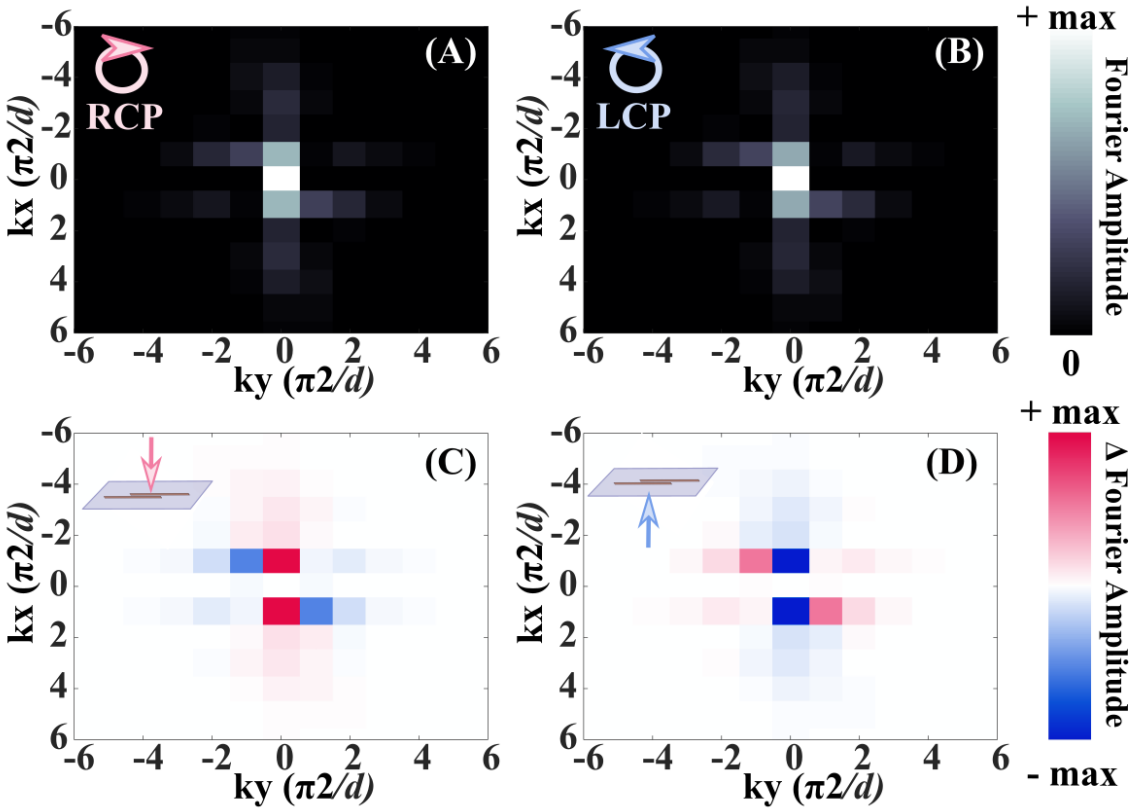

FIGURE 5.2: **Helical Fourier transforms (FT) of chiral near-fields. (A)** and **(B)** show the Fourier amplitude as a function of wave-vector along x and y directions of right- and left-circularly polarised (R/LCP) waves respectively. The complex fields have been extracted from one unit cell of an antenna array in an eigenmode finite element method model, at the resonant frequency of 16 GHz, in a plane 0.1 mm above the array. **(C)** is the difference between RCP and LCP Fourier transforms, the FT dissymmetry, in a plane 0.1 mm above the top of the antenna array. In **(D)** the FT dissymmetry is plotted for the same antenna array but in a plane 0.1 mm below the bottom surface of the array, as illustrated by the arrow in the inset diagrams.

interaction, and are investigated here as a potential route to enhanced chiroptical interactions.

5.3 Helical Array

5.3.1 Experimental and Simulated Spectra

A planar rectangular array of steel helices is used to probe the chiral near-fields generated by the array of staggered-rod antennas. The helices each have three turns, and dimensions (illustrated in figure 5.3 (A)) such that they are subwavelength across the investigated frequency range and can be considered to be perfectly electrically conducting. The pitch of the array was also chosen to mismatch that of the staggered-rod antenna array, so that on average the relative positions of individual helices and antennas will not contribute to the measurements, i.e. any origin-dependent effects are eliminated. The major axes of all the helices are aligned in the same direction, making the array anisotropic as well as chiral, hence ensuring that any contributions to the chirality of the interaction from spatial gradients in the near-fields are probed. The helices are placed into an array of rectangular-cross-section indentations in an additive-layer printed dielectric plate (relative permittivity of $2.73 + i0.03$ across the frequency band of interest, determined from strip-line measurements). A thin layer of paraffin wax was used to secure the helices in place and included in the simulation, as this could be polished to a flat and smooth surface.

The transmission and CD of the helix array *in isolation* are measured using the approach described for the staggered-rod antennas (equations 5.2, 5.3 and 5.4). The results are shown in figure 5.3 (B) and (C). When the incident radiation is polarised along the major axis of the helices, the resonant dip in transmission occurs for a wavelength equal to roughly twice the length of the wire in the helix. Importantly

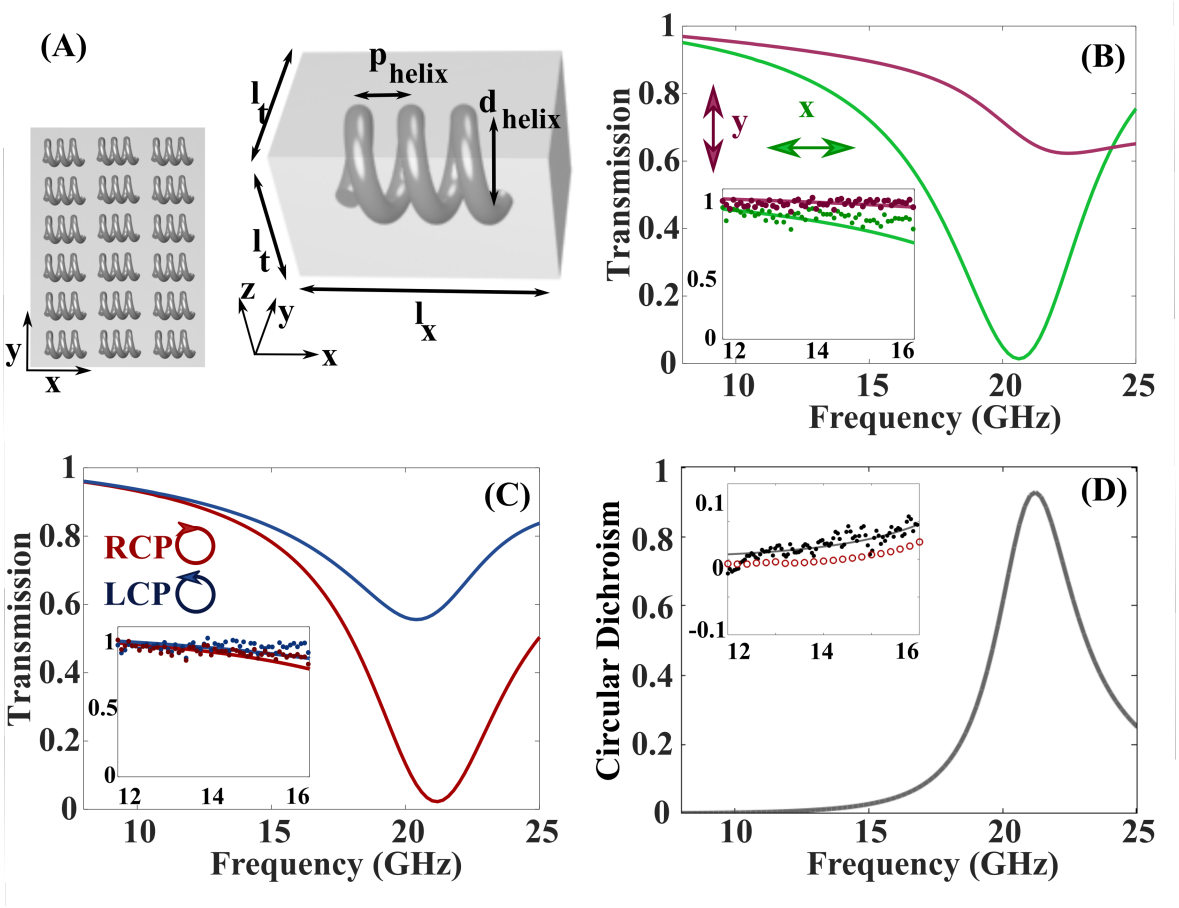

FIGURE 5.3: **Simulated and experimental spectra of the helical layer.** **(A)** Schematic of the helical layer with an enlargement of one unit cell; dimensions are $p_{\text{helix}} = 0.4$ mm, $d_{\text{helix}} = 0.72$ mm, $l_x = 2.0$ mm, $l_t = 1.4$ mm. **(B)** Simulated transmission of linearly polarised radiation through this layer with the polarisation indicated by the coloured arrows; inset shows the comparison between experimental (circles) and simulated (line) transmission in the frequency region of interest (i.e., around the resonance of the staggered rod array, figure 5.1 (B), and reliable parameter extraction). **(C)** Simulated transmission of circular transmission coefficients, with the handedness indicated by the inset arrows; inset shows the comparison between experimental (circles) and simulated (lines) transmission in the region of interest. **(D)** Simulated circular dichroism for this layer; inset shows comparison between the circular dichroism of the array of helices extracted from a full finite element method (FEM) model with a helix unit cell (line) using the unit cell in (A) above, a FEM model using an effective medium description of the array (empty red circles), and experimental data (filled black circles).

the CD of the helix array in the frequency range where the staggered-rods are resonant is relatively small, shown in the inset in figure 5.3 (C). Working below the fundamental resonance of the helices is reminiscent of typical biosensing experiments [51], and provides the opportunity to enhance the CD in a spectral region where it is not already large.

5.3.2 Effective Medium Description

Since the helices in the layer are very subwavelength, one can assume a homogenised description of the helix array may be sufficient. However the effective medium approximation, by definition, assumes that the elements comprising the material are infinitely small compared to the wavelength, hence this model will not encompass any multipolar contributions to the chiral interaction. It should be noted that, as there is only a single layer of helices, the system is best described as a metasurface, rather than a bulk metamaterial. This is evident because the values of extracted parameters will change with the addition of subsequent layers. However an effective medium description of a metasurface of this kind has proven useful in various other systems [92, 126].

The inset in figure 5.3 (D) shows the CD of the effective (i.e. homogenised) medium (red empty circles) compared to the experimental results and full (helix unit-cell) FEM model. The agreement between all three methods is good, so the effective medium model predicts the chirality of the helical array accurately under plane wave excitation. In the following sections the means of extracting the effective parameters will be outlined.

The Homogeneous Chiral Medium

A chiral medium is described by a tensorial permittivity, ϵ, permeability, μ, and chirality, κ, which characterise the electromagnetic response of the system under

plane wave excitation. The constitutive relations for a such a material are described in section 2.1.3. In general the material parameters are 3×3 tensors that may have off-diagonal components. However this array of aligned helices is assumed to be uniaxially anisotropic, and the permittivity and permeability take the form

$$\bar{\bar{\epsilon}} = \begin{pmatrix} \epsilon_x \epsilon_0 & 0 & 0 \\ 0 & \epsilon_t \epsilon_0 & 0 \\ 0 & 0 & \epsilon_t \epsilon_0 \end{pmatrix} \tag{5.5}$$

and

$$\bar{\bar{\mu}} = \begin{pmatrix} \mu_x \mu_0 & 0 & 0 \\ 0 & \mu_t \mu_0 & 0 \\ 0 & 0 & \mu_t \mu_0 \end{pmatrix}, \tag{5.6}$$

where the subscript t denotes the direction transverse to the major helix axis, equivalent to both y and z. ϵ_0 and μ_0 are the permittivity and permeability of free space respectively. A further simplification that can be made is that the material only has chirality, κ, along one direction (the major helix axis, x), and so the cross-coupling parameters have the form

$$\bar{\bar{\xi}} = \begin{pmatrix} -i\kappa\sqrt{\mu_0\epsilon_0} & 0 & 0 \\ 0 & 0 & 0 \\ 0 & 0 & 0 \end{pmatrix} \tag{5.7}$$

and

$$\bar{\bar{\zeta}} = \begin{pmatrix} i\kappa\sqrt{\mu_0\epsilon_0} & 0 & 0 \\ 0 & 0 & 0 \\ 0 & 0 & 0 \end{pmatrix}. \tag{5.8}$$

The small chiral response perpendicular to the helix axis, due to the finite number

of turns in each helix, is ignored. Analytical reflection and transmission coefficients are found by deriving the wave equation in a material with constitutive relations as given in section 2.1.3, and eliminating the electric displacement, $\bar{D}$, magnetisation, $\bar{B}$, and electric field, $\bar{H}$, keeping only the electric field, $\bar{E}$:

$$\begin{aligned} &\bigtriangledown \times \left(\bar{\bar{\mu}}^{-1} \cdot \bigtriangledown \times \bar{E}\right) + i\omega \left[\bigtriangledown \times \left(\bar{\bar{\mu}}^{-1} \cdot \bar{\bar{\xi}} \cdot \bar{E}\right) - \bar{\bar{\zeta}} \cdot \bar{\bar{\mu}}^{-1} \cdot (\bigtriangledown \times \bar{E})\right] \\ &+ \omega^2 \left(\bar{\bar{\zeta}} \cdot \bar{\bar{\mu}}^{-1} \cdot \bar{\bar{\xi}} \cdot \bar{E} - \bar{\bar{\epsilon}} \cdot \bar{E}\right) = 0 \end{aligned} \tag{5.9}$$

Solving this wave equation for the case of a plane wave propagating in the +z direction yields the wave numbers of two elliptically polarised modes for the material:

$$k_{1,2}^2 = \omega^2 \left[\frac{\epsilon_x\ \mu_t + \epsilon_t \mu_x}{2} \pm \sqrt{\left(\frac{\epsilon_x \mu_t - \epsilon_t \mu_x}{2}\right)^2 + \epsilon_t \mu_t \zeta \xi}\right] \tag{5.10}$$

Considering a plane wave normally incident on the material from the -z direction the incident, reflected and transmitted electric fields are defined. These are used to find the reflection and transmission coefficients for waves co- and cross-polarised to the incident wave polarisation.

$$R_{co} = \frac{E_{co}^r e^{-ik_d z_{in}}}{E_0 e^{ik_d z_{in}}} \tag{5.11}$$

$$R_{cr} = \frac{E_{cr}^r e^{-ik_d z_{in}}}{E_0 e^{ik_d z_{in}}} \tag{5.12}$$

$$T_{co} = \frac{E_{co}^t e^{ik_d z_{out}}}{E_0 e^{ik_d z_{in}}} \tag{5.13}$$

$$T_{cr} = \frac{E_{cr}^t e^{ik_d z_{out}}}{E_0 e^{ik_d z_{in}}} \tag{5.14}$$

where $k_d = \omega\sqrt{\mu_d \epsilon_d}$ is the wave-vector in the dielectric medium surrounding the

helices, z_{in} is the plane of the material where the plane wave is incident and z_{out} is the plane of the material through which the wave is transmitted.

By matching the tangential E and H fields at the two boundaries of the material the analytical description for the reflection and transmission coefficients in terms of the material parameters is found to be:

$$\begin{bmatrix} R_{\text{co}} \\ R_{\text{cr}} \\ T_{\text{co}} \\ T_{\text{cr}} \end{bmatrix} = \left(\bar{\bar{N}} - \bar{\bar{M}}_2 \cdot \bar{\bar{M}}_1^{-1} \cdot \bar{\bar{N}}\right)^{-1} \cdot \left(\bar{W} + \bar{\bar{M}}_2 \cdot \bar{\bar{M}}_1^{-1} \cdot \bar{W}\right) \tag{5.15}$$

where each of the matrices are:

$$\bar{\bar{N}} = \begin{bmatrix} \sin\phi & -\cos\phi & 0 & 0 \\ \cos\phi & \sin\phi & 0 & 0 \\ 0 & 0 & \sin\phi & \cos\phi \\ 0 & 0 & -\cos\phi & \sin\phi \end{bmatrix}, \tag{5.16}$$

$$\bar{W} = \begin{bmatrix} \sin\phi \\ \cos\phi \\ 0 \\ 0 \end{bmatrix}, \tag{5.17}$$

$$\bar{\bar{M}}_1 = \begin{bmatrix} \frac{-ik_t^2 k_0 \kappa}{k_1} & \frac{ik_t^2 k_0 \kappa}{k_1} & \frac{-ik_t^2 k_0 \kappa}{k_2} & \frac{ik_t^2 k_0 \kappa}{k_2} \\ k_x^2 - k_1^2 & k_x^2 - k_1^2 & k_x^2 - k_2^2 & k_x^2 - k_2^2 \\ \frac{-ik_t^2 k_0 \kappa e^{-ik_1 d}}{k_1} & \frac{ik_t^2 k_0 \kappa e^{ik_1 d}}{k_1} & \frac{-ik_t^2 k_0 \kappa e^{-ik_2 d}}{k_2} & \frac{ik_t^2 k_0 \kappa e^{ik_2 d}}{k_2} \\ \left(k_1^2 - k_x^2\right) e^{-ik_1 d} & \left(k_1^2 - k_x^2\right) e^{ik_1 d} & \left(k_2^2 - k_x^2\right) e^{-ik_2 d} & \left(k_2^2 - k_x^2\right) e^{ik_2 d} \end{bmatrix} \tag{5.18}$$

and

$$\bar{\bar{M}}_2 = \frac{k_t \eta_d}{\eta_t} \begin{bmatrix} ik_0\kappa & ik_0\kappa & ik_0\kappa & ik_0\kappa \\ \frac{k_1^2-k_x^2}{k_1} & \frac{k_x^2-k_1^2}{k_1} & \frac{k_2^2-k_x^2}{k_2} & \frac{k_x^2-k_2^2}{k_2} \\ -ik_0\kappa e^{-ik_1 d} & -ik_0\kappa e^{ik_1 d} & -ik_0\kappa e^{-ik_2 d} & -ik_0\kappa e^{ik_2 d} \\ \frac{\left(k_1^2-k_x^2\right)e^{-ik_1 d}}{k_1} & \frac{\left(k_x^2-k_1^2\right)e^{ik_1 d}}{k_1} & \frac{\left(k_2^2-k_x^2\right)e^{-ik_2 d}}{k_2} & \frac{\left(k_x^2-k_2^2\right)e^{ik_2 d}}{k_2} \end{bmatrix} \tag{5.19}$$

ϕ is the angle of incident polarisation, k_0 is the free space wave-vector of the incident radiation, $k_{1,2}$ are the wave-vectors in the material as defined in equation (5.10), $k_t = \omega\sqrt{\mu_t \epsilon_t}$ is the wave-vector transverse to the direction of the chirality, $\eta_t = \sqrt{\frac{\mu_t}{\epsilon_t}}$ is the impedance in this direction, $k_x = \omega\sqrt{\mu_t \epsilon_x}$ is the wave-vector along the direction of the chirality, $\eta_d = \sqrt{\frac{\mu_d}{\epsilon_d}}$ is the impedance of the dielectric medium in which the helices are embedded, and $d = z_{in} - z_{out}$ is the thickness of the material. A more complete derivation of these equations can be found in [27].

Fitting and Parameter Extraction

The effective parameters describing the chiral material are derived through fitting the complex reflection and transmission spectra predicted from a full FEM model to these analytical predictions. For this extraction, a non-linear least-squares algorithm was employed to minimise the difference between co- and cross-polarised reflection and transmission coefficients taken from the FEM model, and those calculated from equation (5.15). This was performed for a single frequency at a time, for 4 angles of incident polarisation (ϕ), equally spaced across 2π radians. This gave 16 input parameters in total (co- and cross-polarised reflection and transmission for 4 incident polarisations), used to extract 10 material parameters (real and imaginary parts of 5 material parameters), ensuring that the system was not under-sampled. By starting at very low frequencies, where the chirality is almost zero and the permeability

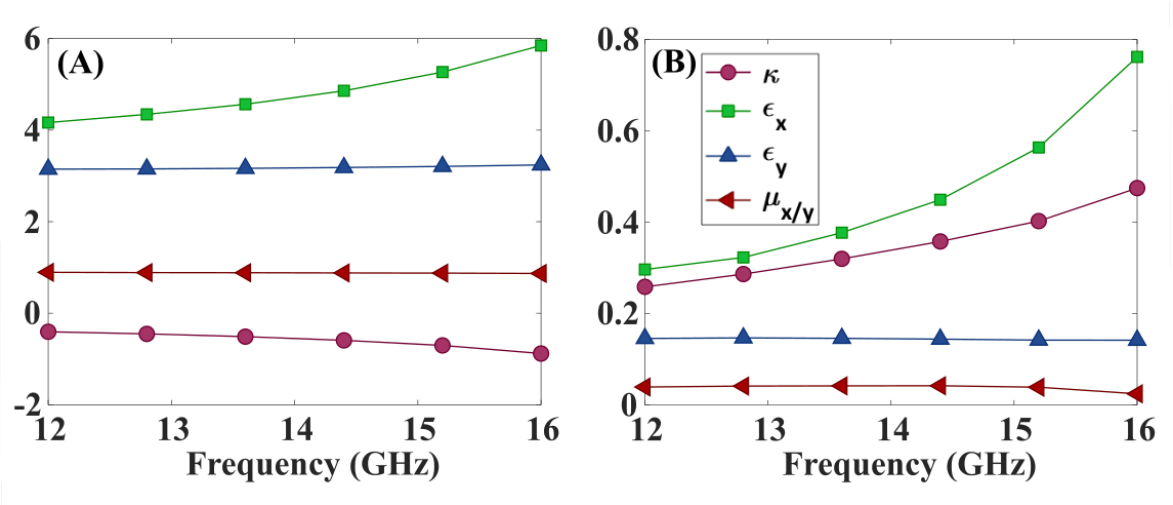

FIGURE 5.4: **Effective parameters for the helical layer.** Real **(A)** and imaginary **(B)** parts of the relative material parameters: chirality (κ), which acts only along the x-axis, equivalent to the major helix axis, permittivity (ϵ) along x- and y-axes, and permeability (μ) which is the same along both x- and y-axes.

is almost 1, a simplified model based on Fresnel reflection and transmission coefficients from a finite layer, was used to extract only the permittivity. This gave a starting point for the initial value in the fitting algorithm. The frequency was progressed, and the parameters extracted at the previous frequency were used as the initial guess for the next. In this way the global minimum of the function was found at each frequency.

However, the extraction becomes increasingly difficult as the frequency is further increased towards the resonant frequency of the helices. Once the thickness and index of the material become such that more than one wavelength fits inside the layer, the extracted parameters are no longer representative of the material. The extracted, frequency-dependent parameters are presented up to 16 GHz in figure 5.4. It should also be noted that, close to the helix resonance, the meta-atoms are no longer significantly sub-wavelength, and the reliability of any local effective parameter approximation reduces greatly. A more detailed discussion of the fitting technique can be found in section 3.4. The range covered does include the resonant frequency of the staggered-rod antennas, and so is acceptable for this work.

The material parameters obtained through this fitting technique are then used to describe a layer of chiral material in a FEM model. This cannot be achieved by inputting only the material parameters, as the wave equation itself must be manipulated to describe a chiral medium. The methods for achieving this are outlined in section 3.3.3.

5.4 Chiral Antenna Dichroism

5.4.1 Definition of Chiral Antenna Dichroism

The response of the combined system will now be considered: the helical layer placed on one face of the rod antenna array. To define the strength of interaction between the chiral fields generated by the staggered-rod antennas and the helical layer, it is necessary to introduce a new quantity, which will be called chiral antenna dichroism (CAD). As a near-field analogy of circular dichroism, where field handedness is generated by the symmetry of the antenna, CAD is a measure of the difference in intensity of the radiation transmitted through the combined system when the handedness of the antenna (staggered rod array) is switched, normalised to the sum of the two measurements:

$$CAD = \frac{|\tau_{\mathrm{LH}}|^2 - |\tau_{\mathrm{RH}}|^2}{|\tau_{\mathrm{LH}}|^2 + |\tau_{\mathrm{RH}}|^2} \tag{5.20}$$

where the subscript on τ represents the handedness of the antenna array (as seen from the side closest to the helices). A non-zero value of CAD is expected only when a chiral material is within the near-fields of the antennas, indicating a difference in coupling between RH and LH antennas. Figure 5.5 (A) shows the experimentally measured CAD when the helices are parallel and perpendicular to the major axis of the rods. It is clear that, since the CAD is non-zero, this is a measurement of the

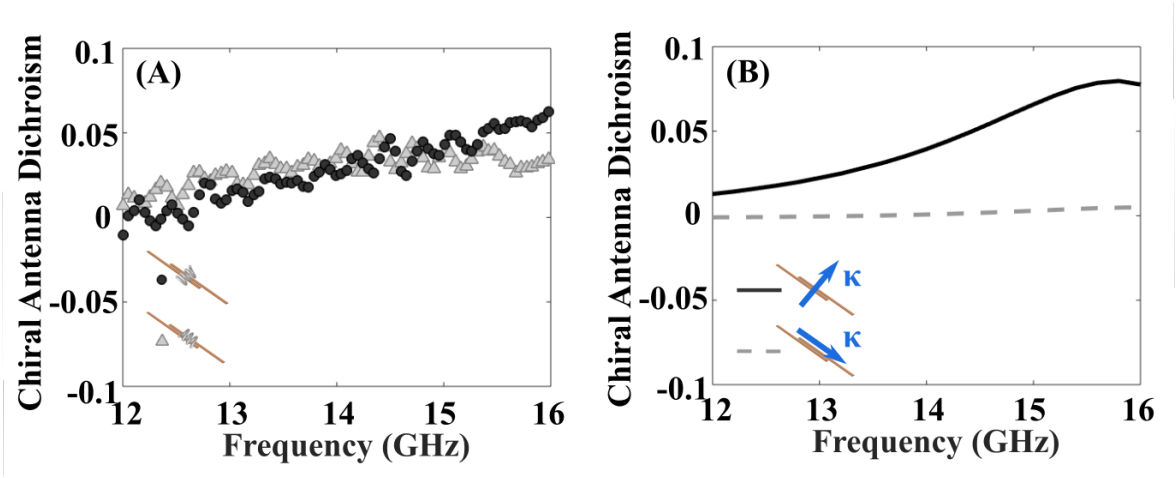

FIGURE 5.5: **Experimental and simulated chiral antenna dichroism.** **(A)** Experimental chiral antenna dichroism (CAD) of the helix layer, for helices oriented parallel (grey triangles) and perpendicular (black circles) to the major rod axis. **(B)** Simulated CAD using an effective medium representation of the helical array with the chirality material parameter, κ, oriented parallel (grey dashed line) and perpendicular (black solid line) to the major rod axis.

chiral interaction between the antenna array and the helical array, similar to that in [33].

5.4.2 Experimental Measurement

At this point, the nature of this chiral interaction is considered. It is interesting to note that the CAD (figure 5.5 (A)) of the helical array is of a similar magnitude to the circular dichroism (Figure 5.3 (C)) in the same frequency range. This suggests that any enhancement in the interaction due to the presence of rapidly decaying near-fields is too small to contribute significantly to the measurement.

Furthermore, the measured CAD of helices oriented parallel and perpendicular to the rod axis are very similar. This indicates that the helical array is not especially sensitive to the spatial variation of the chiral near-fields around the staggered-rod antennas.

5.4.3 Effective Medium Model

It is time to question whether any evidence of non-locality in the chiral interaction is observed, i.e., whether the spatial gradients allow coupling to multipolar modes, and whether this affects the observed CAD. If a non-local contribution is significant, a completely local description of the helical material, as described in section 5.3.2, would be inadequate to describe the interaction. Instead, a non-local description of the helical metamaterial would be necessary, where the material parameters are a function of both the frequency and wave-vector. To determine if this is indeed the case, figure 5.5 (B) shows the CAD calculated from a FEM model where the arrays of helices has been replaced by an equivalent effective medium, described by $\epsilon(\omega)$, $\mu(\omega)$ and $\kappa(\omega)$. Results are shown for the chiral material parameter, κ, oriented both parallel and perpendicular to the major rod axis. (Note that a good agreement with experiment, figure 5.5 (A), is not expected for the parallel chirality case, due to approximations made in the analytical description [121].) The pivotal point is that the orders-of-magnitude enhancements predicted in previous works [33, 52, 60] are not observed here. Considering that the model does not take into account the discrete size of the helices or their interactions, it is remarkable that, although the exact frequency dependence of the spectra are not perfectly replicated, the sign and magnitude closely resemble that of the experimentally measured CAD. This suggests that non-local effects and multipolar enhancements do not contribute significantly to the CAD measurement - the array of helices is essentially behaving as a local material. Indeed, it is clear that the contribution to the chiral interaction from multi-polar components in the field is minimal.

5.4.4 Dependence on Separation

To further understand the interaction between the helices and the evanescently decaying fields close to the staggered-rod array, a study of the separation dependence

of the CAD was carried out. The experimental results in figure 5.6 (A) show a slightly counter-intuitive result. Assuming that the CAD is a near-field effect, as the helices are moved out of the near-fields the CAD should decrease exponentially. However figure 5.6 (A) shows that the CAD actually *increases* with increasing separation. This can be explained as a Drexhage-like effect [150]. When the helical material, comprised of discrete scatterers, is close to the rod array (which acts like a poor mirror), image currents and image polarisations in the mirror act to cancel the field scattered by the helices [151]. These "image" helices are of the opposite handedness to the helices in the real helical material, so it is no surprise that the CAD is small when the helices and rod array are close to each other [152]. As the separation is increased, but still less than one wavelength, the "image" helices become weaker and the CAD increases. This effect is also seen when the electric field intensity is measured just above the rod array using a dipole antenna. If the separation is increased beyond one wavelength, the characteristic oscillations of the Drexhage effect are also observed.

However this effect is not seen in the case of the effective medium model, as here there are no discrete scatterers, which are necessary to generate image currents of opposite handedness in the reflecting sheet. Therefore the CAD decays with increasing separation. This decay follows well the decay of the electric field intensity away from the centre of one unit cell in the antenna array that is extracted from the FEM model so as to remove the effects of the presence of an antenna, as in the experimental measurement. This is plotted in figure 5.6 (B).

From these data it is clear that the presence of discrete chiral elements in the helical array does influence the CAD as a function of the separation between the helical material and antenna array. Still, no significant enhancement is present over the effective medium approximation. It also highlights the fact that interactions between chiral materials and structured surfaces are more complicated than it appears at first glance, and the full details of the mechanisms behind such interactions have

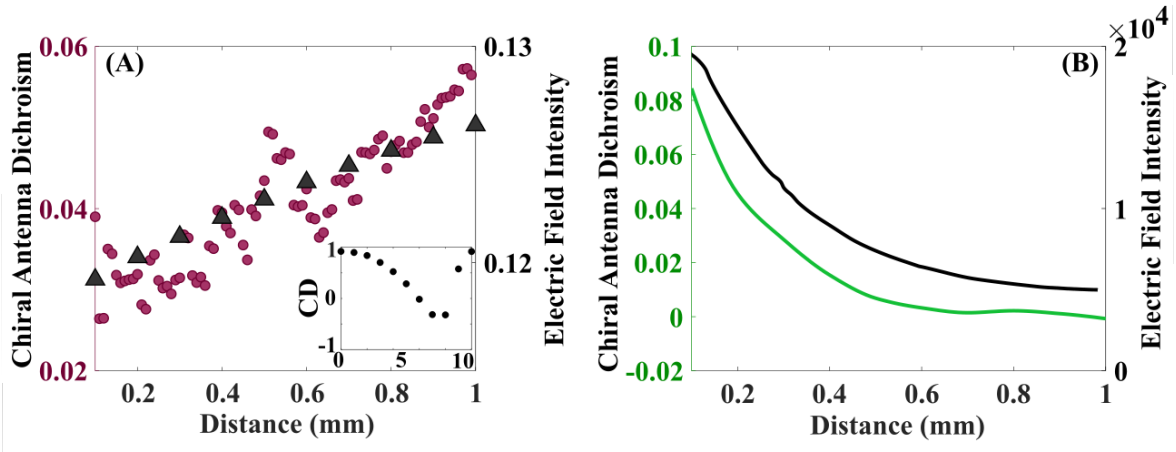

FIGURE 5.6: **Separation dependence of chiral antenna dichroism. (A)** Experimentally measured chiral antenna dichroism (magenta circles, corresponding to left y-axis) as a function of the distance between helices and antennas, for helices perpendicular to the major rod axis at 16 GHz. The black triangles (corresponding to right y-axis) show the electric field intensity measured experimentally by a small dipole antenna as a function of its distance from the rod array, also at 16 GHz.Inset in **(A)** shows the circular dichroism (CD) measured in reflection from the helices next to a perfectly electrically conducting mirror at 16 GHz as a function of distance. **(B)** Simulated chiral antenna dichroism of the effective medium (green line, corresponding to left y-axis) at 16 GHz as a function of separation; electric field intensity (black line, corresponding to right y-axis) extracted from a finite element method model from the centre of a staggered-rod unit cell, as a function of distance from the rod array at 16 GHz.

yet to be fully understood. A means for further investigation into this phenomenon is suggested in section 7.2.

5.5 Conclusion

In this chapter, the chiral electromagnetic (EM) near-fields generated by an array of staggered-rod antennas were investigated using an array of metallic helices as a probe. The chiral antenna dichroism (CAD) was used as a measure of the interaction strength between the chiral near-fields and helices. This was measured experimentally, and compared to a model of an equivalent homogeneous medium. It was found that the CAD of the helical array could be predicted fairly accurately by approximating it as a homogeneous chiral material. It is therefore clear that the non-local contribution to the chiral interaction is minimal.

However, there are a number of important differences that may account for discrepancies between this experiment and those of [33]. Firstly, the frequency of radiation used in this report is much lower than reported in [33]. As a result the contribution to the interaction from the plasmonic behaviour of the antennas is not included. It is well accepted that the concentrated electric fields around plasmonic particles can increase the excitation rate of molecules, increasing the sensitivity with which they are detected in general [53]. Recent works have also claimed large enhancements in the circular dichroism measured from chiral molecules placed on achiral plasmonic structures [57, 65], proposing that the enhanced circular dichroism is due to strong absorption in the metal at the plasmon frequency with the chiral plasmonic response induced by the handedness of the chiral molecules [67]. In such circumstances the plasmon-exciton interaction is key, and the spatial structure of chiral evanescent fields around the particles themselves plays little, if any, role in measurements of CD and optical rotation [67]. Another important factor may be the alignment of molecules adsorbed on a surface in [33]. The orientation of molecules

with respect to the electric field vectors in the vicinity of the plasmonic particles has been shown to play an important role in the magnitude of CD signals in [71], and also suggested in [69, 70]. Once again this effect seems to rely on plasmonic enhancement through a Purcell type effect, and not directly on the spatial structure of chiral evanescent fields. In any respect, it is clear that the origin of the signal enhancement in [33] demands further investigation.

Chapter 6

Broadband Dispersionless Slow Waves on Long Helices

The experimental data presented in this chapter were collected by Gareth Ward at the University of Exeter. The data analysis, simulations, theoretical calculations and interpretation were performed by the author.

Introduction

In this chapter the behaviour of an electromagnetic wave bound to a periodic chiral structure - an "infinitely long" metal helix - is investigated. The helix has infinite-fold screw symmetry, which leads to some interesting features in the energy-dispersion of the waves, such as a lack of band-gap at the Brillouin zone edge, and regions of zero dispersion. The effect of this symmetry is discussed, and the limitations to the bandwidth of the dispersionless region are highlighted and explained in terms of the evanescent fields around the helix. A suggestion for modifying the geometry to obtain a larger bandwidth while maintaining the screw-symmetry is given in the final section.

6.1 Background

6.1.1 Slow Waves

Structured media, such as metamaterials and photonic crystals, can be used to control the flow of electromagnetic waves - both the direction and the speed. Many structures have been proposed that control the direction [96, 97], but control of the velocity of waves is also useful. A wave with a group velocity significantly less than the speed of light is called a "slow wave", and their study has been a topic of great interest since the first experimental discovery of slow light in 1999 [153]. Many applications have been suggested that can benefit from waves travelling at much slower velocities, including enhancing non-linear interactions [154], manipulation of small particles [155], increased efficiency of solar cells [156], more sensitive Raman spectroscopy [157], compact data storage [158], and studying fundamental light-matter interactions [159]. Many of these applications take advantage of the fact that by allowing light to travel more slowly, it interacts more strongly with the surrounding media, without the need to increase the intensity. These concepts can equally be applied in the microwave regime [160, 161].

Slow wave wave-guides are most often created by overlapping media that have negative and positive refractive indices [162]. The result is that the wave travels a little forwards, then a little backwards, then a little forwards again, so that the average velocity is very slow, similar to walking up a steep icy hill in inappropriate foot-wear. The most pressing challenges currently in the field are the need for broad bandwidths and low losses. As many applications involve the slowing of pulses, which must contain many frequencies if they are to be spatially restricted, the operational bandwidth of slow wave wave-guides is particularly important.

6.1.2 Higher-Order Symmetries

In the 1960's and 1970's higher-order symmetries in periodic surfaces were investigated, primarily glide (or glide-plane) and screw (or screw-axis) symmetries. A full definition of higher-order symmetry is given in section 2.2.4. It was found that waves supported on structures with glide and screw symmetry crossed at the Brillouin zone boundary in reciprocal space without the presence of a band-gap, and were dispersionless over a wide frequency range [114], thanks to the degeneracy in energy of the field configurations of the modes. This analysis, based only on symmetry arguments, was backed up by experimental results [163] and more complete theoretical studies [113, 117, 164].

This work has inspired many more recent investigations into the implications of higher-order symmetries on the dispersion of waves. Recently it has been shown that periodic structures possessing glide-symmetry can be used to create dispersionless metasurfaces [115, 165] and wave-guides [116, 166]. These are particularly useful for constructing leaky wave antennas [167, 168], non-dispersive broadband lenses [169, 170], and shields for integrated wave-guides [171].

In this work, an "infinitely" long helix is investigated as a structure capable of supporting a non-dispersive slow wave over a large frequency range. A helix possesses screw symmetry of order $n = \infty$, and so is a promising candidate for high index, broadband, tunable wave-guides. There are, however, some limiting factors that reduce the bandwidth of a wave supported on a long helix. In this chapter the origins of the features in experimentally measured dispersions will be explained using numerical and analytical models. The limitations to bandwidth and index will be addressed, and a suggestion for how to minimise the effects that limit bandwidth will be presented.

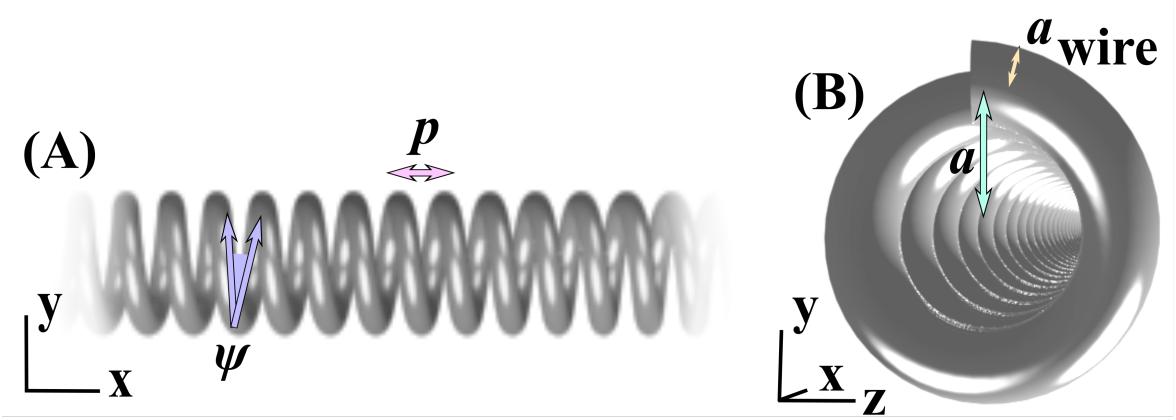

FIGURE 6.1: **Schematic of long helices. (A)** is a side view of the helix and **(B)** is view of a cross-section. In the simulations and theory, the helix is assumed to be infinitely long, however the helix used for the experimental measurement is 247 cm long, with roughly 2500 turns. For all helices the wire radius $a_{\text{wire}} = 0.351$ mm. The measurements of the short pitch helix (before stretching) are $\psi = 6.94°$, $p = 0.922$ mm and $a = 1.206$ mm. The long pitch helix (after stretching) dimensions are $\psi = 7.35°$, $p = 0.980$ mm and $a = 1.205$ mm.

6.2 Dispersion of the Wave on a Long Helix

6.2.1 Experimental Measurement

Using the technique outlined in section 3.2.3 the dispersion of the wave on a long helix is measured experimentally. This involves placing a source at one end of the helix, and scanning a probe along its length, detecting the complex electric field as a function of position and frequency. A diagram and further explanation of the experimental set-up can be found in section 3.2.3. The Fourier transform of this matrix of data is taken, and the dispersion found. The helix is assumed to be infinitely long, as the ratio of diameter to length is around 2×10^{-4}, making the end-effects negligible, and the self-resonance frequency (due to the total length of wire in the helix [172]) very low.

In the case of the experiment, the intensity of the wave measured depends on the coupling between the bound wave, the source and the probe. When collecting the data in figure 6.2 the source was located at one end of the helix and the probe

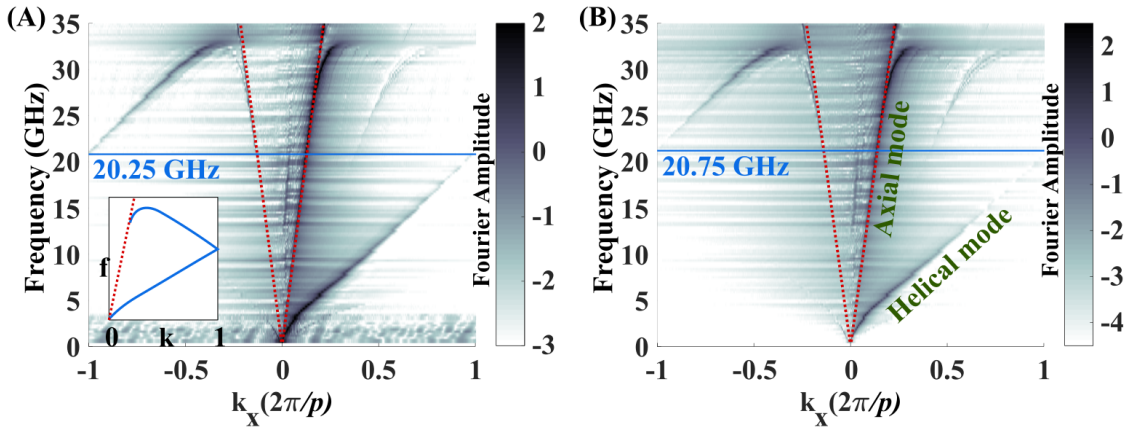

FIGURE 6.2: **Experimental measurements of the dispersion of two helices with different dimensions.** The colour plot shows the Fourier amplitude of the wave as a function of wave-vector along the helix axis and frequency. The red dashed line represents the light line. Only waves with a positive direction of propagation are detected in this measurement, and the inset in **(A)** shows the shape of the dispersion without this complication. The helical and axial modes are labelled in **(B)**. The helix in **(A)** has dimensions $\psi = 6.94°$, $p = 0.922$ mm and $a = 1.206$ mm, and the helix in **(B)** has been stretched to $\psi = 7.35°$, $p = 0.980$ mm and $a = 1.205$ mm. The blue horizontal lines point out the slight difference in gradient of the two helical modes, and the frequencies at which the mode reaches the first Brillouin zone edge.

was scanned in one direction away from the source. This means that waves with only positive group velocity will be detected. In order to see the full dispersion of the wave when it crosses over the first Brillouin zone (BZ) and is diffracted back, the negative and positive halves of the dispersion must both be plotted. Without the added complication of coupling efficiency, the positive and negative propagating waves would both be represented in the first positive BZ, as illustrated by the schematic dispersion in the inset of figure 6.2 (A).

The dispersions of waves on two different helices are presented in figure 6.2, where helix (A) has a shorter pitch than helix (B). In fact, helix (B) is helix (A) after it has been stretched. The exact dimensions for both helices are stated in the figure caption. In each case two modes are detected - one that travels along the light line with an index determined by the surrounding medium (air in this case). This will be

referred to as the axial mode. A high index mode is also seen, which will be referred to as the helical mode. There is an additional faint mode that appears in both plots, that only becomes visible at high frequencies. This mode is an artefact produced by the measurement technique, and will not be discussed further.

For both helices the wave disperses linearly over a wide frequency range, and no band-gap forms at the edge of the BZ. The linear mode index (i.e. effective refractive index) and zero band-gap are common features in systems with screw symmetry [117, 164]. The lack of band-gap is due to the fact that the BZ is defined by the translation symmetry of the helix. This unit cell is the smallest section from which the rest of the structure can be built by translating it along an axis, as described by the translation operator in section 2.2.4. In this case, it is one turn of the helix. However, this unit cell can be reduced further by using the screw symmetry operator, which is also described in section 2.2.4. The screw symmetry unit cell of a n-order screw symmetric system is n times smaller than the translation symmetry unit cell of the same system. In reciprocal space the BZ will be n times larger. In the case of the helix, $n = \infty$, and it is not practical to plot an infinitely large BZ. It is common to represent the band structure of a metasurface using the reduced-zone scheme, where all bands lying outside the first (translation symmetry) BZ are folded back into the first. Doing this results in no loss of information as the waves are reciprocal. This is the representation that will be used throughout this chapter.

The waves on both helices are very similar, but the wave on the short pitch helix (A) crosses the BZ edge at 20.75 GHz, whereas the wave on the long pitch helix (B) crosses at 20.25 GHz, as highlighted by the blue horizontal lines in figure 6.2. This small difference in the dispersion of waves becomes much clearer when looking at the mode indices. For the forwards propagating wave, a mode index can be extracted from the experimental results. This is shown in figure 6.3. In order to find the mode index, the dispersion must first be extracted. This is done by selecting

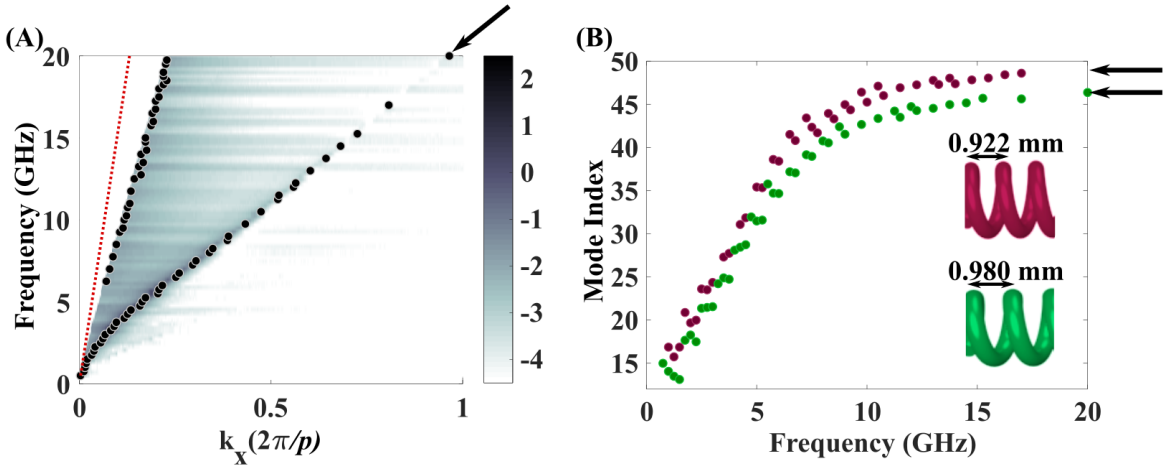

FIGURE 6.3: **Experimental mode index of the helical wave. (A)** shows the experimental dispersion of the longer pitch helix from figure 6.2 (B), with the data close to the light line (red dashed line) removed. Black circles highlight the points on the dispersion used to calculate the mode index in **(B)**. The mode indices as a function of frequency are plotted for both of the helices. Black arrows indicate the regions of linear dispersion that leads to the constant index, that shows a decrease in index of 3 at high frequencies, due to a 6% stretch.

the maximum Fourier amplitude at each frequency, and recording the corresponding wave-vector. The light line, still represented by the dashed red line, has been removed from the data to make this extraction easier (the large white region at low wave-vectors). As can be seen by the points in figure 6.3 (A), the desired points are not always selected. Nevertheless, the technique allows for enough points to be extracted to find a reliable plot of the mode index, figure 6.3 (B).

The most compelling feature of this graph is the region of constant mode index at high frequencies, highlighted by the black arrows. The mode indices achieved here are extremely high, far exceeding those of naturally occurring materials and rivalling all but the most extreme indices found in artificial media [173]. Due to the non-dispersive nature of the wave at high frequencies, the group index is equal to the mode index, as explained in section 2.2.4. This means the group velocity of the wave is slowed by a factor of 46 compared to a wave in free space. While this is by no means the slowest wave reported [153], helices provide an advantage over

traditional slow wave wave-guides in their tunability. Comparing the mode indices of the two helices at 17 GHz, there is a difference in index of around 3. This was achieved by a stretch of only 6% in the helix, and highlights that helices can be particularly useful for creating tunable and slowly varying high-index wave-guides. With sufficiently careful measurements, helices may also offer a route to experimentally explore non-linear effects in microwave metamaterials [174, 175].

6.2.2 Numerical Model

A finite element method (FEM) model helps to give more insight into the experimental results. By studying plots of the electric field and current, an intuitive interpretation of the linear dispersion can be more easily arrived at. One turn of a helix is modelled with a perfectly electrically conducting surface, and Floquet boundary conditions are placed on perpendicular faces to make an infinite helix, as explained in section 3.3.2. This is the unit cell that defines the size of the BZ. In this model the complexity introduced by coupling between probe and bound wave in the experiment is removed. The modelled dispersion shows the mode that exists in the next BZ folded back into the first positive BZ, as we would expect.

The agreement between the modelled and experimental dispersion is good, as shown in figure 6.4. Small inconsistencies arise from the uncertainty in the measurement of the helix radius, and the slightly inhomogeneous stretching of the helix. The mode index extracted from the FEM model also agrees well with the experimental results. However, at very low frequencies, the FEM model becomes unreliable due to the presence of "box-modes" (i.e. standing waves in the air box of the model), which artificially perturb the modes that are within or on the light-line.

Figure 6.5 shows the components of the electric field ((A), (C) and (E)) and surface current density ((B), (D) and (F)) along the helix axis, at the points indicated by black stars on the inset dispersions. In figure 6.5, (A) $k_x = 0.5$, the fields just above

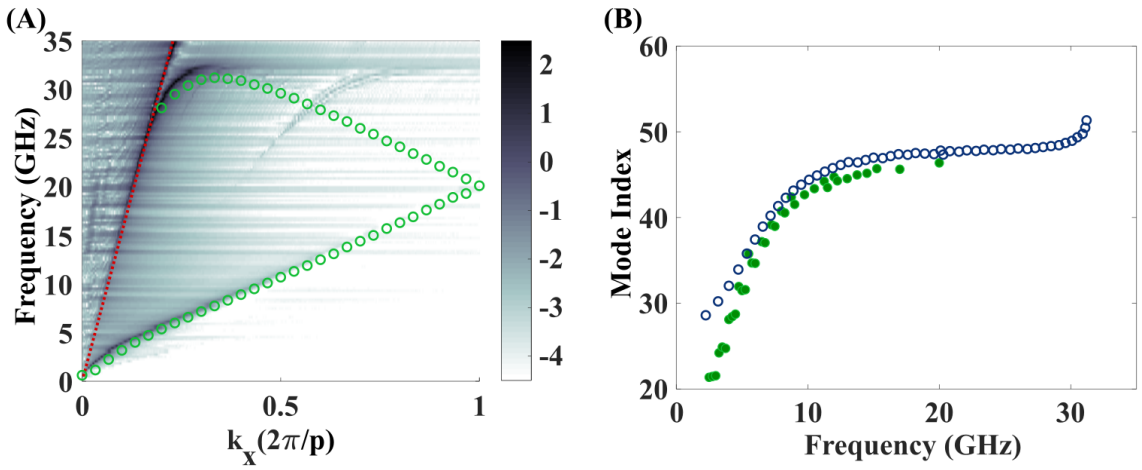

FIGURE 6.4: **Comparison of the experiment and finite element method (FEM) model. (A)** shows the experimental dispersion (colour plot) and the dispersion from the FEM model (circles). The red dashed line represents the light line. **(B)** compares the mode index found from experiment (filled green circles) and FEM model (empty blue circles). All results are for the longer pitch helix in figure 6.2 (B).

the helix are periodic along the helix axis with a periodicity illustrated by the dashed black box surrounding one repeating unit. At this wave-vector the box encloses four turns of the helix. The surface current density in (B) shows that the current reverses direction twice in every repeating unit of the current, indicated by the dark green arrows. The largest surface current density is found at the points on the wire where they are closest to the wire of the adjacent turn. For each turn there are two regions where the currents are strongest. This differs from the case of a straight wire where the surface current density would be constant around the circumference of the wire.

The electric field and surface current density in figure 6.5 (C) and (D) are plotted at the BZ edge, $k_x = 1$. Here, the repeating unit (black dashed box) encloses two turns of the helix. The x-component of the electric field reverses direction with each turn of the helix, as does the current in figure 6.5 (D), shown by the dark green arrows. In fact, the frequency of this mode meets the condition where incident wavelength is equal to twice the length of wire in a single turn.

In figure 6.5 (E) and (F), after $k_x = 1$ we turn around and reach $k_x = 0.5$ in the

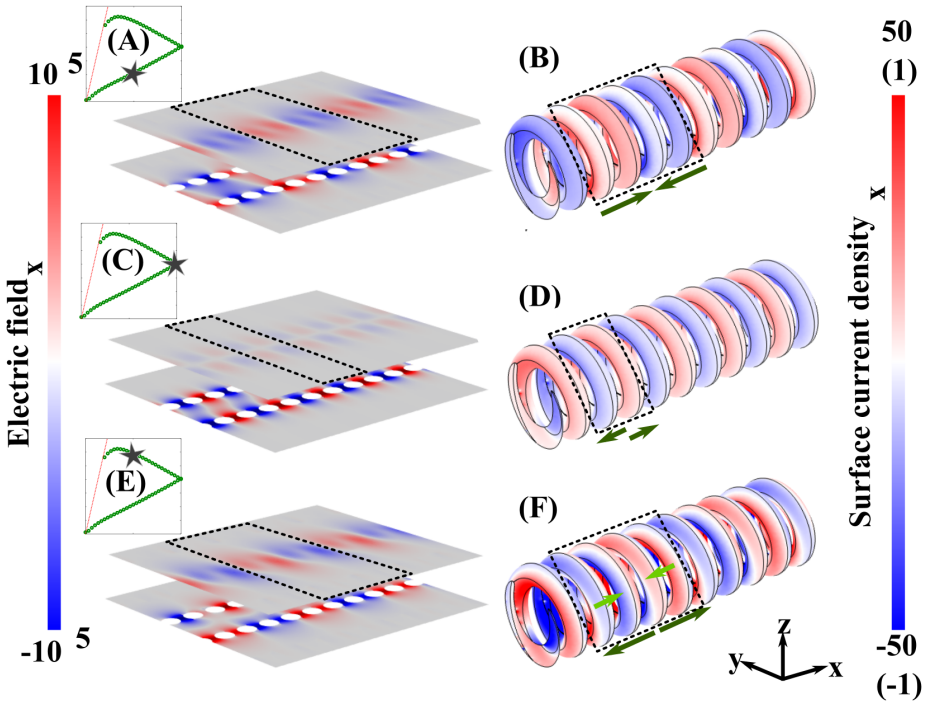

FIGURE 6.5: **Electric field and surface current from the FEM model. (A)**, **(C)** and **(E)** are plots of the electric field component along the helix axis in a slice through the centre of the helix and on a plane 0.1 mm above the helix. **(B)**, **(D)** and **(F)** show the surface current density along the helix axis. The numbers in brackets on the scale bar refer to **(D)**. Black stars on the inset dispersions show the wave-vectors at which the fields and currents have been extracted. Dotted black boxes highlight the size of the repeating unit in the fields or currents at each wave-vector. Dark green arrows show the direction of current in each repeating unit, and in **(F)** the light green arrows show the direction of current within the repeating unit on the far side of the helix.

second band, which could more accurately be referred to as $k_x = 1.5$ in the extended zone scheme. Similar to the electric field in (A), the repeating unit contains four turns of the helix, although now there is a slight skew in the fields. The origin of this is in the periodicity of the surface currents along the helical wire, plotted in figure 6.5 (F). Past the BZ edge, where one half-wavelength fits inside each turn of the helix, the current distribution becomes more complicated as more than one wavelength fits inside one turn of the helix. Figure 6.5 (F) shows that within each repeating unit the current no longer simply goes from positive to to negative. There is an extra flip in the direction of current, illustrated by the light green arrows in

figure 6.5 (F).

This explains why the energy-dispersion of the wave is linear. The pattern illustrated by a few examples in figure 6.5 is repeated as the wave-vector increases, with more and more wavelengths fitting inside each turn of the helix. The wire of the helix is continuous, so there is no condition that restricts the wavelengths to be the function of a dimension. Therefore waves of every wavelength will experience the same environment and the same mode index. (This is evidently not true across the whole frequency range, and the factors that pull the dispersion away from the ideal linear case will be discussed in section 6.3.)

6.2.3 Geometrical Approximation

Figure 6.5 show that the current along the helical wire is strongest at the points where the wires in adjacent turns are closest. This implies that the currents, and therefore the wave, follow a path along the length of the coiled up wire in the helix. This assumption can be used to derive a geometrical approximation for the dispersion of the wave. For a perfectly electrically conducting straight wire the wave would travel at the speed of light in the surrounding medium (air in this case) [176], and this is a valid approximation at GHz frequencies. Bending the wire into a helical shape is equivalent to folding up space and increases the length of the path the wave must travel. The dispersion of the wave, and the mode index, can be calculated by finding the ratio between the distances covered travelling around the wire or straight along the axis of the helix, via the equation,

$$k_x^{\text{geom}} = k_0 \frac{\sqrt{p^2 + 4\pi^2 a^2}}{p} \tag{6.1}$$

where k_0 is the wave-vector of a wave that disperses along the light-line. In the case of small pitch helices, the circumference of a turn is roughly equal to the circumference of the projection of the turn, so we can write,

$$k_x^{\text{geom, small } p} = k_0 \frac{2\pi a}{p} \tag{6.2}$$

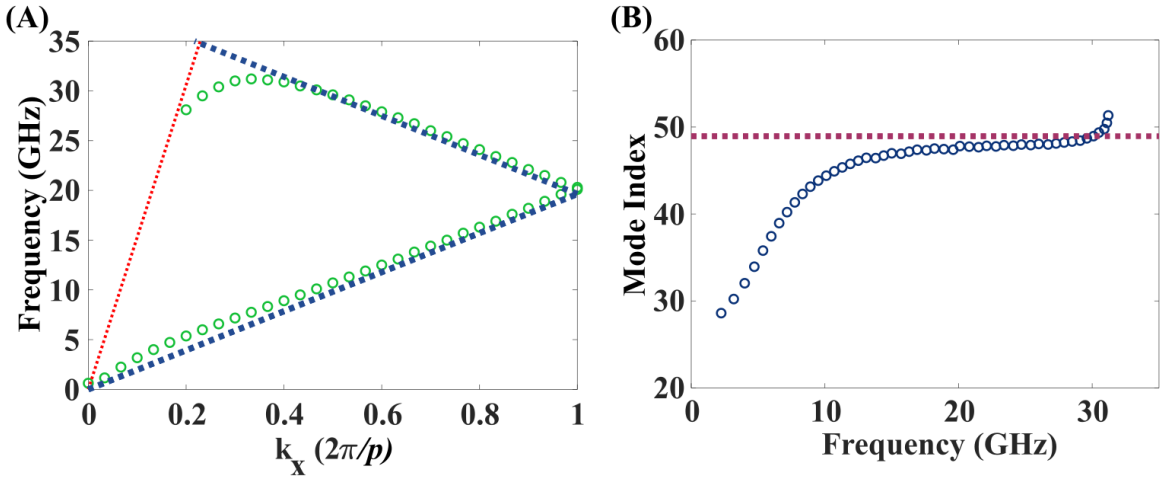

FIGURE 6.6: **Comparison of the finite element method (FEM) and geometrical approximation.** **(A)** shows the dispersion found by the FEM model (green empty circles) compared to that calculated using a geometrical (blue dotted line). **(B)** shows the mode index from the FEM model (blue empty circles) and the asymptotic mode index (magenta dotted line) found from the geometrical approximation. The agreement is good only at moderate wave-vectors. The dimensions of the helix are the same as those in figure 6.2 (B).

A comparison between the results of the FEM model and the geometrical approximation is shown in figure 6.6. Both the dispersion and the mode index are predicted well by the geometrical approximation for moderate wave-vectors. The agreement between modelling and geometrical approximation at these wave-vectors increases as the thickness of the wire decreases and the wave is more confined to travel along only this path. This is a useful approximation when designing high index media, as a plot like that in figure 6.8 (A) can be used to select the geometry required for a given index. However it is only valid in the frequency range where the dispersion is linear and the index is constant, even for infinitely thin wires. The index found using this method is referred to as the asymptotic mode index.

6.2.4 Analytical Calculation

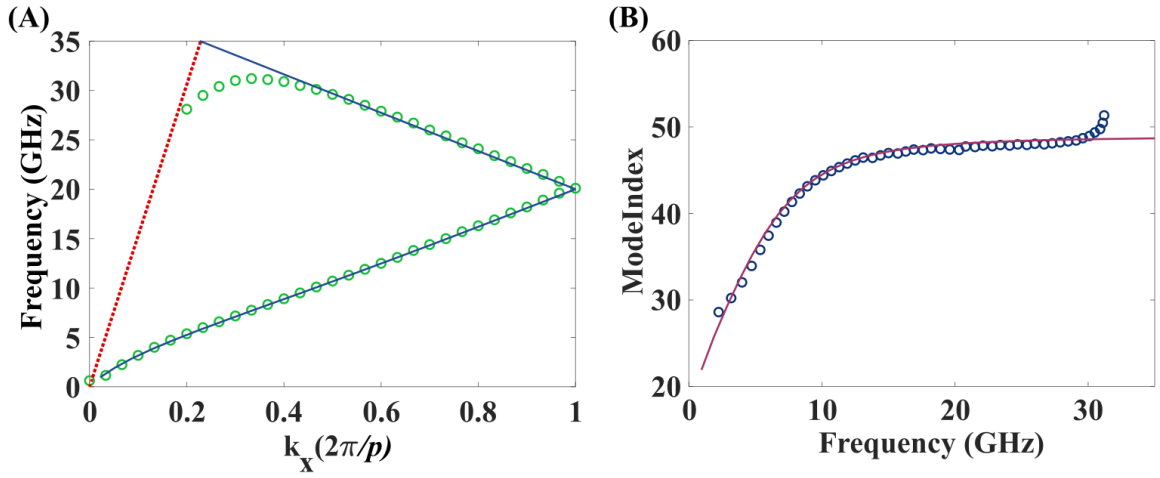

FIGURE 6.7: **Comparison of the finite element method (FEM) and the sheath helix theory.** **(A)** shows the dispersion found from the FEM model (green empty circles) compared to that calculated using the sheath helix theory [105] (blue line). **(B)** shows the mode index from the FEM model (blue empty circles) and that found from the sheath helix theory (magenta line). The agreement is good at low and moderate wave-vectors. The dimensions of the helix are the same as those in figure 6.2 (B).

A more accurate way to find the dispersion of the wave on a helix is through an analytical model, such as the sheath helix theory [105]. It is assumed that the helix can be simplified to an infinitely thin conducting cylinder with an anisotropic impedance. These assumptions reduce the accuracy of the theory slightly, and more recent works have built upon these to include the width of the wire, and the coupling of adjacent turns of helices [172]. However this model is sufficient to describe the low frequency behaviour of the wave bound to a long helix, as illustrated by comparing the results to those of an FEM model in figure 6.7.

The waves inside the helix are described by modified Bessel functions of the first kind (I_n) of order n and argument (γa), while the fields outside the helix are described by modified Bessel functions of the second kind (K_n). This is to ensure that the fields outside the helix decay with increasing distance from the helix, and

that inside they grow as they approach the helix. γ is a relative wave-vector, and is defined as:

$$\gamma^2 = k_x^2 - k_0^2 \tag{6.3}$$

A full derivation of the dispersion relation can be found in Appendix B. The equation that is reached is:

$$\frac{I_n'(\gamma a)K_n'(\gamma a)}{I_n(\gamma a)K_n(\gamma a)} = \frac{\left(\gamma^2 a^2 + k_x n a \cot\psi\right)^2}{k_0^2 a^2 \gamma^2 a^2 \cot^2\psi} \tag{6.4}$$

where the prime signifies differentiation with respect to the argument, and a, p and $\psi = \cot^{-1}(2\pi a/p)$ are as defined in figure 6.1. For the $n = 0$ mode this simplifies to:

$$\frac{I_1(\gamma a)K_1(\gamma a)}{I_0(\gamma a)K_0(\gamma a)} = \frac{\gamma^2}{k_0^2 \cot^2\psi} \tag{6.5}$$

Taking the low frequency limit of this equation confirms that at zero frequency the wave will travel along the helix at the speed of the wave in air. Rearranging the equation for convenience:

$$a^2 k_x^2 = \frac{I_1(\gamma a)K_1(\gamma a)}{I_0(\gamma a)K_0(\gamma a)} k_0^2 a^2 \cot^2\psi - k_0^2 a^2 \tag{6.6}$$

In the limit of very small γa:

$$a^2 k_x^2 \simeq 0 - k_0^2 a^2 \tag{6.7}$$

$$a k_x \simeq \pm k_0 a \tag{6.8}$$

From this it is clear that the wave-vector of the bound wave is the same as that of the incident wave-vector in free space at the lowest wave-vector.

The high frequency limit of this dispersion relation can also be investigated. Starting from equation 6.5 and solving for the limit of very large k_x:

$$a^2k_x^2 = 1 \times k_0^2a^2\cot^2\psi - k_0^2a^2 = \frac{-k_0^2a^2}{\sin^2\psi} \tag{6.9}$$

$$ak_x = \pm k_0a\frac{1}{\sin\psi} \tag{6.10}$$

This result is approximately equal to that given by 6.2, and further validates the geometrical approximation made in section 6.2.3.

These are the two limits of the theoretical dispersion at very low and high wavevectors. As γa increases the dispersion of the wave will turn towards the linear region with a curvature dependent on the argument of the Bessel functions. Since these describe the fields inside and outside the helix, it could be supposed that the curvature of the dispersion in this region is determined by the decay of the fields in relation to the radius of the helix. In fact this will be shown explicitly in section 6.3.1.

6.3 Limits to the Bandwidth

6.3.1 Low Frequency Limit

Good agreement is seen between dispersions found from the sheath helix theory and the FEM model at low frequencies in figure 6.7. This theory can be used to probe the low frequency behaviour of the bound wave for various dimensions of helices. In figure 6.8 (A) the asymptotic mode index, calculated using the geometrical approximation, is plotted for various helices. As expected, the highest indices are found for short pitch and large radius helices. The orange dotted lines represent geometries that will give the same asymptotic index. In figure 6.8 (B), the mode indices for

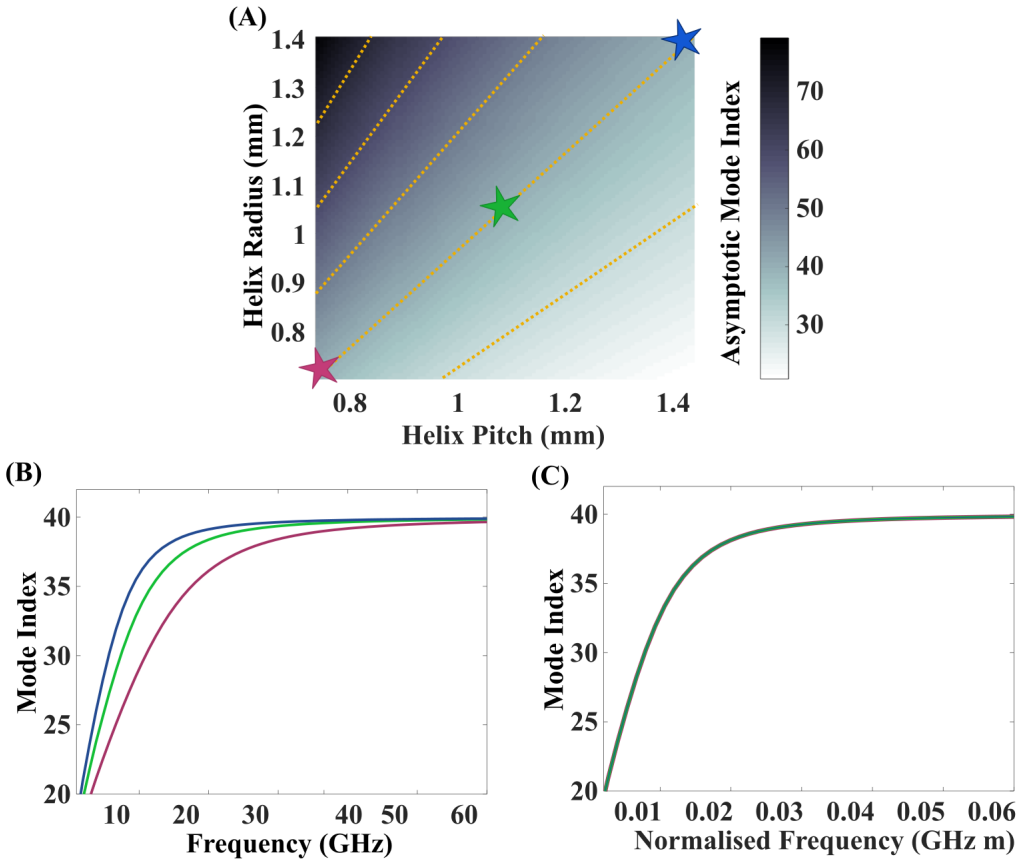

FIGURE 6.8: **Investigating the low frequency limit to the region of constant index.** **(A)** is a plot of the asymptotic mode index derived from the geometrical approximation for helices of various dimensions. Orange dotted lines show the sets of dimensions that will lead to the same asymptotic mode index. **(B)** shows the mode index as a function of frequency for three dimensions of helices with the same asymptotic mode index. The colours of the lines correspond to the geometries marked by the stars in **(A)**. In **(C)** the same dispersions have been plotted against a normalised frequency parameter, $f_{\text{norm}} = f \times a$. The three lines perfectly overlap, showing the relationship between the bandwidth and helix dimension.

three geometries highlighted by the stars of corresponding colour in 6.8 (A) are plotted, and the difference in the low frequency behaviour becomes apparent. In figure 6.8 (C) the mode indices for the same helices have been plotted, but now against a new parameter of frequency normalised to the helix radius, $f_{\text{norm}} = f \times a$. The frequency at which the bound wave on the helix approaches the asymptotic limit is proportional to $1/a$, so when plotted against the f_{norm} parameter the dispersions perfectly overlap. This verifies the argument put forward in section 6.2.4 based on the sheath helix theory - the curvature of the dispersion at low wave-vectors is determined by the decay length of the fields around the helices compared to the helix radius. A similar normalisation could be done using the pitch instead of the radius as the mode index is determined by their ratio.

This highlights the origins of the low frequency limit to the bandwidth of a constant mode index. This limit can be somewhat avoided by making the helix radius as large as possible, so that even at low frequencies the decay of the fields is over a small length scale in proportion to the helix dimensions. Up to a certain point, this limit is straightforward to avoid, but practical implementations will mean limits on size that cannot be avoided. Another way to avoid this problem is discussed in section 6.4.

6.3.2 High Frequency Limit

There is also a high frequency limit to the region of non-dispersive index. This is not taken into account in either the geometrical approximation or the theoretical calculations, but is clearly seen in the experimental (figure 6.2) and FEM dispersions (figure 6.4). It is caused by the presence of a wave supported by the helix that lies along the light line - the axial mode. This is essentially a grazing incidence photon that is trapped along the helix but does not experience a high mode index due to the turns.

Both axial and helical modes exist along the helix within the first BZ, with different dispersions. The frequency and wave-vector of both modes match at a point where the two waves are travelling in opposite directions along the helix. The waves will interfere to produce a standing wave with zero group velocity. The mode index increases accordingly at this point.

This limit is not so straightforward to work around, as tuning the overall size of the helix will not help. Instead, this limit is proportional to the index of the helix. In figure 6.9 the mode indices of two different helices are shown as a function of frequency. It is clear that the frequency at which the region of linear index ends is inversely proportional to the index. This is because the axial wave will always disperse in the same manner on all helices (in air), but a helical wave with a higher index will have a dispersion with a larger gradient, and so will meet the axial wave at a lower frequency on the dispersion diagram. This is illustrated in the schematic inset in figure 6.9.

6.4 Increasing Bandwidth

The previous sections have shown that the bandwidth of the constant index is dependent on different factors at the high and low frequency limit. The high frequency limit is determined by the interference of the axial and helical mode. At low frequencies the decay of fields around the helix must be over a short distance compared to the radius of the helix to achieve a constant index. Equipped with this knowledge, it is possible to suggest a modification to the geometry that will increase the bandwidth through manipulation of the fields. A straight wire is inserted in the centre of the helix. Having a cylindrical wire in the centre does not alter the symmetry of the system, as doing so would cause band-gaps to appear according to the new order of screw symmetry (see section 2.2.4). This modification will also leave the helix open so that the wave can be used to probe non-linear and enhanced interactions, and

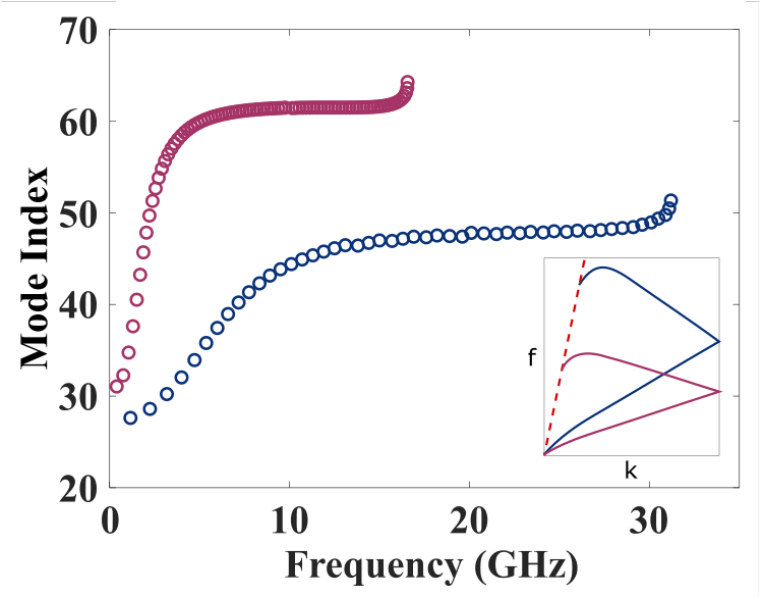

FIGURE 6.9: **Investigating the high frequency limit to the region of constant index.** The mode index as a function of frequency for two helices, calculated from a finite element method model. Blue circles correspond to the helix described in figure 6.2 (B), and the magenta circles are for a helix with $\psi = 5.83°$, $p = 1.54$ mm, $a = 2.4$ mm and $a_{\text{wire}} = 0.7$ mm. The upper frequency limit to the region of constant index is inversely proportional to the asymptotic mode index. This is due to interference with the axial mode, as illustrated by the schematic dispersions inset.

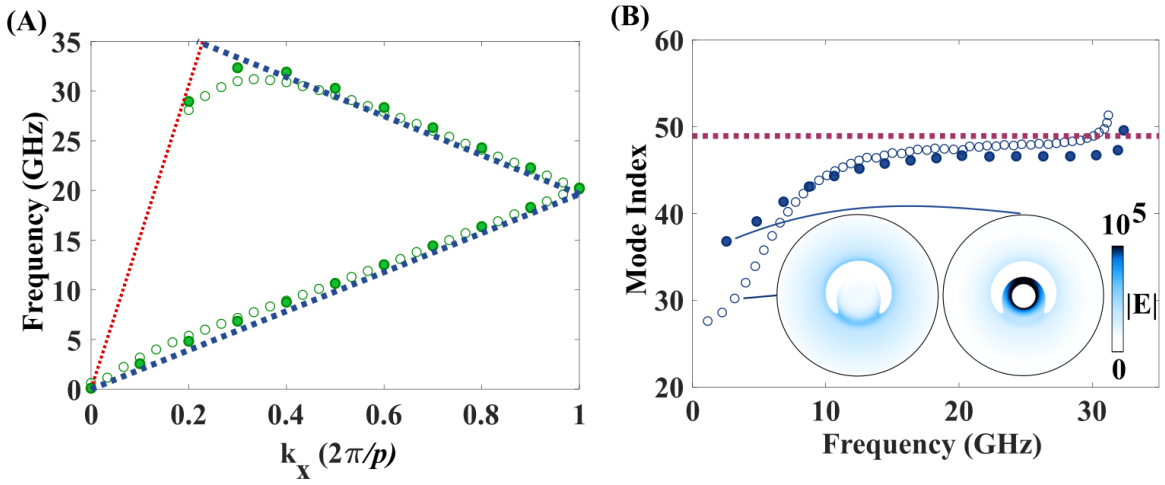

FIGURE 6.10: **Adding a cylindrical wire at the centre of the helix. (A)** shows the dispersion and **(B)** is the mode index for a helix with dimensions stated for figure 6.2 (B). The dotted lines are from the geometrical approximation, and the circles are from a finite element method (FEM) model of a helix (empty circles), and a helix with a cylindrical wire in the centre with radius $a_{\text{central wire}} = 1.5a_{\text{wire}}$ (filled circles). Insets in **(B)** show the electric field intensity in a cross-section through the helix (left) and the helix with a wire in the centre (right) at $k_x = 0.1$.

allow the measurement technique described in section 3.2.3 to be used. However, the presence of the wire will perturb the evanescent fields within the helix, and lead to an increase in bandwidth as discussed in more detail below.

Inset in figure 6.10 (B) are two plots of the electric field intensity at cross-sections through an empty helix (left) and one with a wire in the centre (right) at the same low wave-vector. There is a significant difference in the distribution of the electric field in both cases. When a wire is present in the centre of the helix the electric field is more strongly confined to the helix, in particular the centre. The wire creates new boundary conditions on the fields at the centre, so that the tangential electric field must be zero and the normal magnetic field must be zero. This forces the fields to decay over a shorter length scale. According to the sheath helix theory and the conclusions drawn in section 6.3.1, this will lead to a more linear dispersion at low frequencies.

As seen in figure 6.10 (A), the dispersion of the wave on the helix with the central wire (filled circles) tends more towards the geometrical approximation than the empty helix (empty circles) at both low and high wave-vectors. At moderate wave-vectors the dispersion does not change significantly with the addition of the central wire, as most of the electric field is concentrated around the wire of the helix. The mode index shown in figure 6.10 (B) does not reach such low values at low frequencies, as expected from the distribution of the fields.

The presence of the central wire also increases the upper frequency limit. As shown in figure 6.10 (B), the region of constant index extends to frequencies around 2 GHz higher than that of the empty helix. The axial mode is still present, so the axial and helical modes still interfere, but the extent in wave-vector over which the interference occurs is smaller. This can be explained by considering that the confinement of the fields is greater when the central wire is present. This causes the mode overlap between axial and helical modes at wave-vectors slightly away from the point of matched frequency to decrease, and the interaction of the modes to become weaker.

The central wire provides a new degree of freedom that can be tuned to give a greater range of properties. A straight wire in the centre will not introduce band-gaps, but if it is moved closer to one side, the order of screw symmetry will be reduced to $n = 1$, and a band-gap will open after two trips around the BZ. One can now imagine replacing the straight central wire with a periodically varying one, for example a sinusoid, saw-tooth or square wave. If this periodicity is on a length scale much larger than the pitch of the helix and chosen carefully, it is possible to create a wave-guide with a varying mode index based on broken symmetries.

6.5 Conclusions

In this chapter, the electromagnetic waves supported on an infinitely long helix have been investigated. Two modes were measured in the experiment - an axial mode that dispersed along the light line, and a helical mode with a high mode index.

Due to the screw symmetry of the helix, the helical mode did not produce a band-gap at the edge of the Brillouin zone, and had a large region of constant mode index. This asymptotic mode index could be predicted by a geometrical model, based on the length of the wire in one turn. A more tightly wound helix, with a larger radius or shorter pitch, produced a higher index, and this could be tuned by stretching or pulling the helix.

The origins of the upper and lower frequency limits to this region of constant index were then investigated. Thanks to the results of a sheath helix analytical theory, it was found that the lower frequency limit was proportional to the ratio between wavelength and helix dimension, and a larger overall helix would decrease the frequency at which the dispersion became linear. The upper frequency limit was set by the interference of the axial and helical modes on the helix, and was found to be inversely proportional to the mode index.

Finally, the addition of a straight wire in the centre of the helix was studied. It was found that this small addition improved the linearity of the dispersion, by forcing a faster decay in the electric fields inside the helix, and pushing the dispersion towards the asymptotic limit at lower frequencies. The tighter confinement of the fields to the helix also weakened the interaction between the axial and helical modes, increasing the upper limiting frequency at the same time.

Chapter 7

Future Work

Introduction

In this chapter I will present some ideas for the continuation of the work presented in the previous chapters of this thesis.

The first area that warrants further investigation is that of higher-order chiral arrangements, or in other words, placing subwavelength chiral objects in a larger unit cell, arranged in a chiral patter. It is possible that arranging small chiral objects, such as biomolecules or metal helices, in chiral arrangements with a larger extent in space will have an interesting effect on the chiroptical signals measured.

My next suggestion is to study in more detail the effects of placing chiral objects next to mirrors of different kinds, as orientation and separation can greatly influence the circular dichroism measured in reflection from such a system.

Finally, I present a method for analysing experimentally the interaction between a field with orbital angular momentum and an array of helices. According to recent theoretical studies this may be a route to more sensitive detection of chiral molecules.

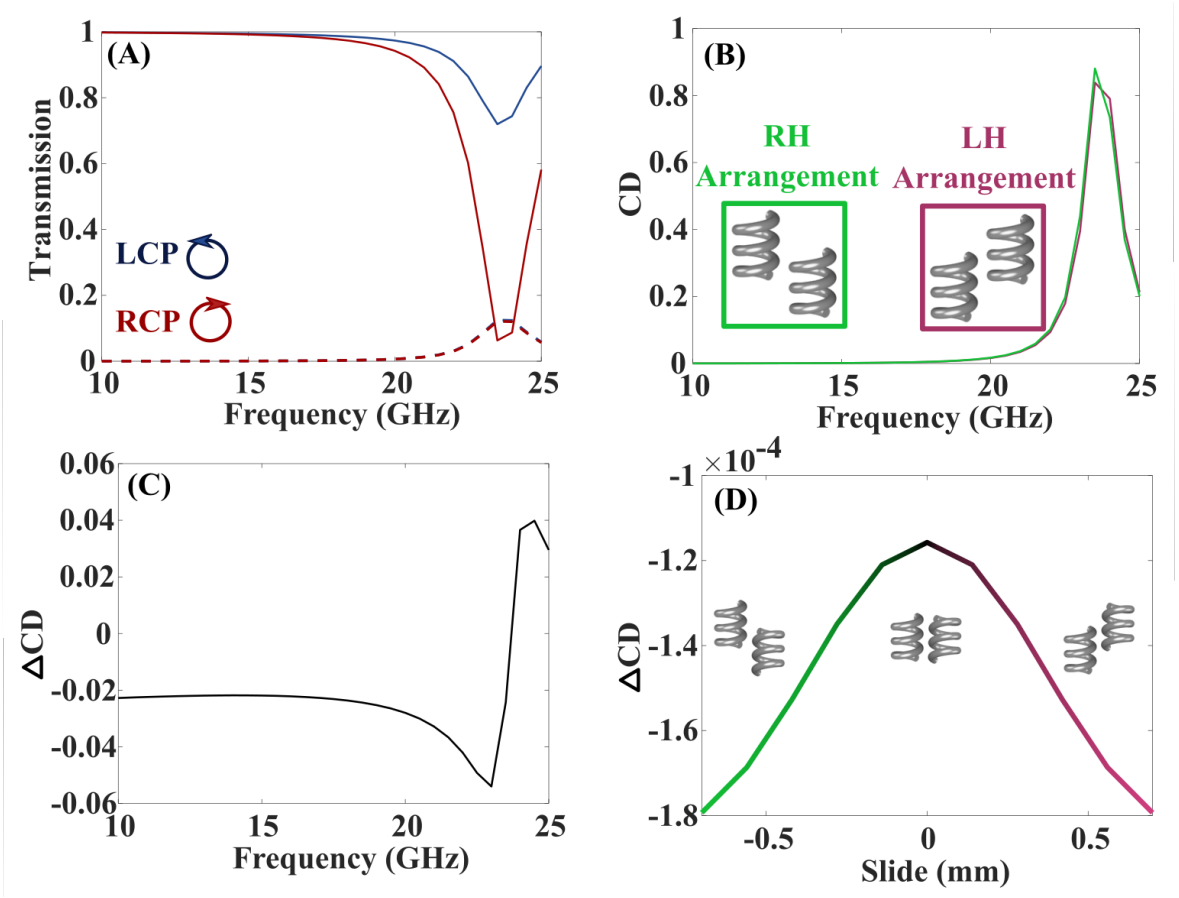

FIGURE 7.1: **Planar-chiral arrangements of helices. (A)** is the transmission spectrum of circularly polarised waves through a an array of left-handed (LH) helices in a LH arrangement, illustrated in the inset of **(B)**, which shows the circular dichroism (CD) from arrays of both handedness. **(C)** is a plot of the difference in CD for left- and right-handed arrays, and **(D)** is the difference in CD as a function of the slide between the two helices in a unit cell.

7.1 Higher-Order Chiral Arrangements

In works that report enhanced sensitivity in the detection of chiral molecules thanks to chiral plasmonic particles, it is likely that the molecules stick preferentially to the nanoparticles, and are forced into a chiral arrangement [33, 52]. It is already known that the orientation of individual chiral molecules is important in determining the strength of the chiral interaction [70, 71], but the effects of the symmetry of the entire arrangement is yet to be investigated.

These effects may offer a route to enhancing chiroptical interactions, as the strength

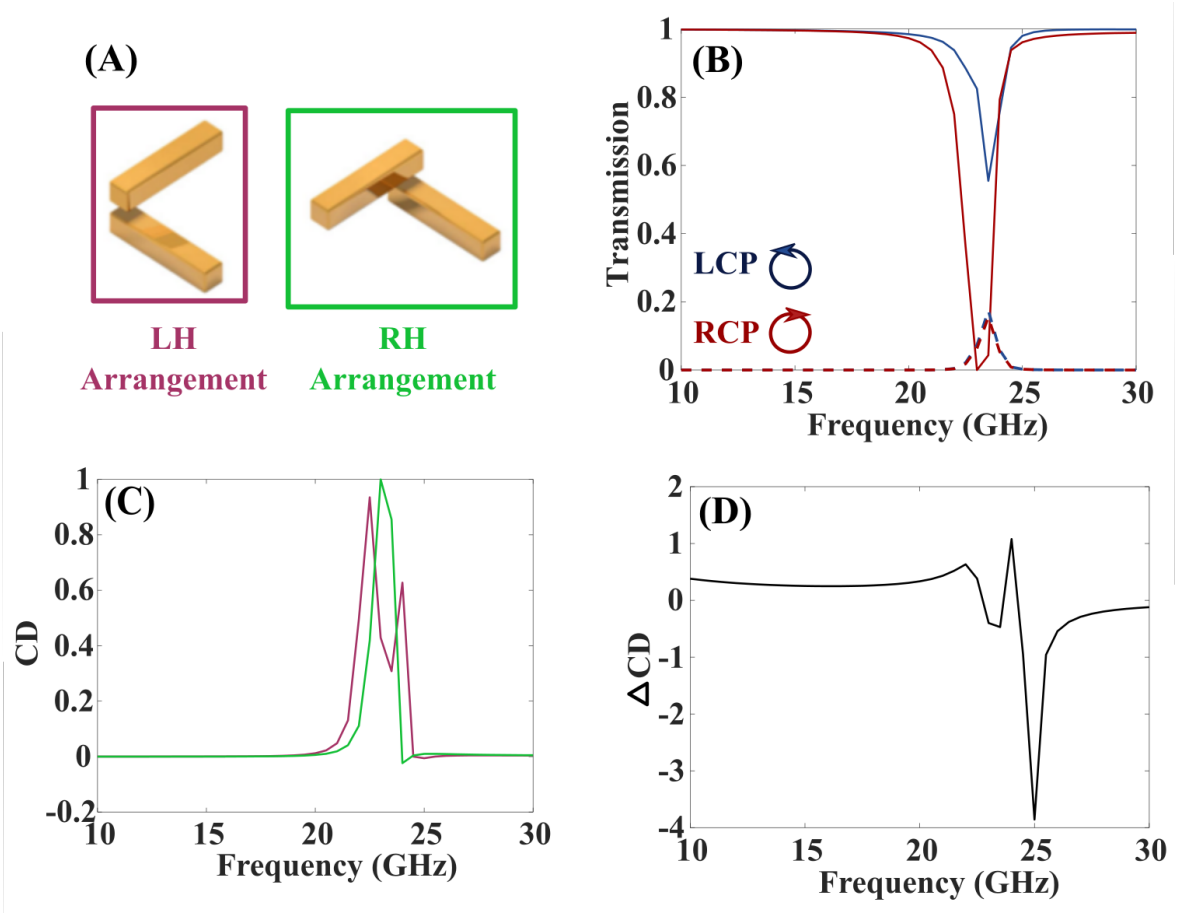

FIGURE 7.2: **Three-dimensionally chiral arrangements of helices.** The helices are arranged as the rods are in **(A)** to make three-dimensional left-handed (LH) and right-handed (RH) arrangements. **(B)** is the transmission of circularly polarised waves through LH helices in a RH arrangement, and **(C)** is the circular dichroism (CD) for each handedness of array. **(D)** is the difference in CD from LH and RH arrays as a function of frequency.

of the chiral signal is dependent on the difference in length scales between the wavelength and the structure [14]. It may also offer an explanation into the results found in [33]. If the handedness of the arrangement of chiral molecules is important, it could provide a cheap and simple way to improve the sensitivity of detection (e.g. by placing molecules on substrates with engraved patterns, eliminating the need for expensive metals and fabrication techniques).

I present here some preliminary modelling of a microwave analogy to such an experiment, similar to that carried out in chapter 5. The transmission of circularly

polarised waves through an array of helices with dimensions the same as those in chapter 5 is shown in figure 7.1 (A). There are two helices per unit cell, and they are staggered with respect to each other by half their length, creating a planar chiral pattern out of 3-dimensionally chiral objects. The left-handed (LH) and right-handed (RH) arrangements are illustrated in the inset of figure 7.1 (B), which shows the CD of the two arrays. Figure 7.1 (C) is a plot of the difference in CD for RH and LH staggered pairs of helices, and shows a peak at the resonant frequency of the helices, and more interestingly a small signal at low frequencies. However this offset is not a feature of the chirality of the system, as in figure 7.1 (D) the difference in CD is plotted again as a function of the "slide" between the two helices. A positive value means a LH arrangement, a negative value is a RH arrangement, and at zero slide the arrangement is achiral. In this case, the helices have been rotated so that the ends of their wires both meet at the centre, and there is no contribution from the arrangement to the CD signal.

Helices can also be arranged in 3D chiral patterns, such as the twisted stacks illustrated by two rods in figure 7.2 (A) [29]. In this case the transmission of circularly polarised waves through each array is quite different, as shown by the CD plot in figure 7.2 (C). The peak in CD at the resonance splits into two peaks when the handedness of the arrangement matches the handedness of the helices. The reasons behind this are not yet fully understood, and may also be influenced by the relative rotations of the helices in each stack.

In terms of applications to bio-sensing, such an arrangement of chiral molecules would be very difficult to create and so not very useful for industrial applications. The splitting of the peak in CD would highlight this kind of effect if achieved accidentally. However further investigation of these kinds of effects would deepen understanding of interactions between chiral molecules with different relative orientations.

7.2 Chiral Media Next to Mirrors

The results presented in chapter 5 show that the interaction between a chiral medium and a chiral electromagnetic field is highly dependent on the separation. It would be useful to study in greater depth the chiroptical signals from an array of helices next to a reflecting surface, and perhaps study the effect of different types of mirrors.

Some work has previously been published on planar chiral objects next to mirrors, and it was found that a CD could be measured when at angles off from normal incidence [21]. The paper also stated that no CD would be measured from 3-dimensional objects next to a mirror, as the wave will change handedness upon reflection from the mirror and the interactions of the forward and reflected wave will cancel. However I have found that this depends on the orientation of the chiral object, the distance between the mirror and helices, and absorption in the chiral layer.

I have performed some initial modelling on an array of helices next to a perfectly electrically conducting (PEC) mirror, presented in figure 7.3. The helices are the same dimension as those studied in chapter 5, and are surrounded by the same lossy dielectric described in that chapter. The CD was measured in reflection, and in reflection this means measuring the difference between converted circular polarisations.

Figure 7.3 (A) and (B) show the orientations in-plane and out-of-plane helices respectively, next to a perfectly electrically conducting (PEC) mirror, along with the electric (red arrows) and magnetic (blue arrows) dipoles in the original and image helices. In both cases, the image helix has the opposite handedness to the original. Plotted in figure 7.3 (C) is the CD at 25 GHz of the wave reflected from the in-plane helices and mirror, as a function of the separation. The value is small, but not zero, and shows an oscillatory nature based on the wavelength of incident radiation. The green line is drawn at the separation at which one half wave-length fits between

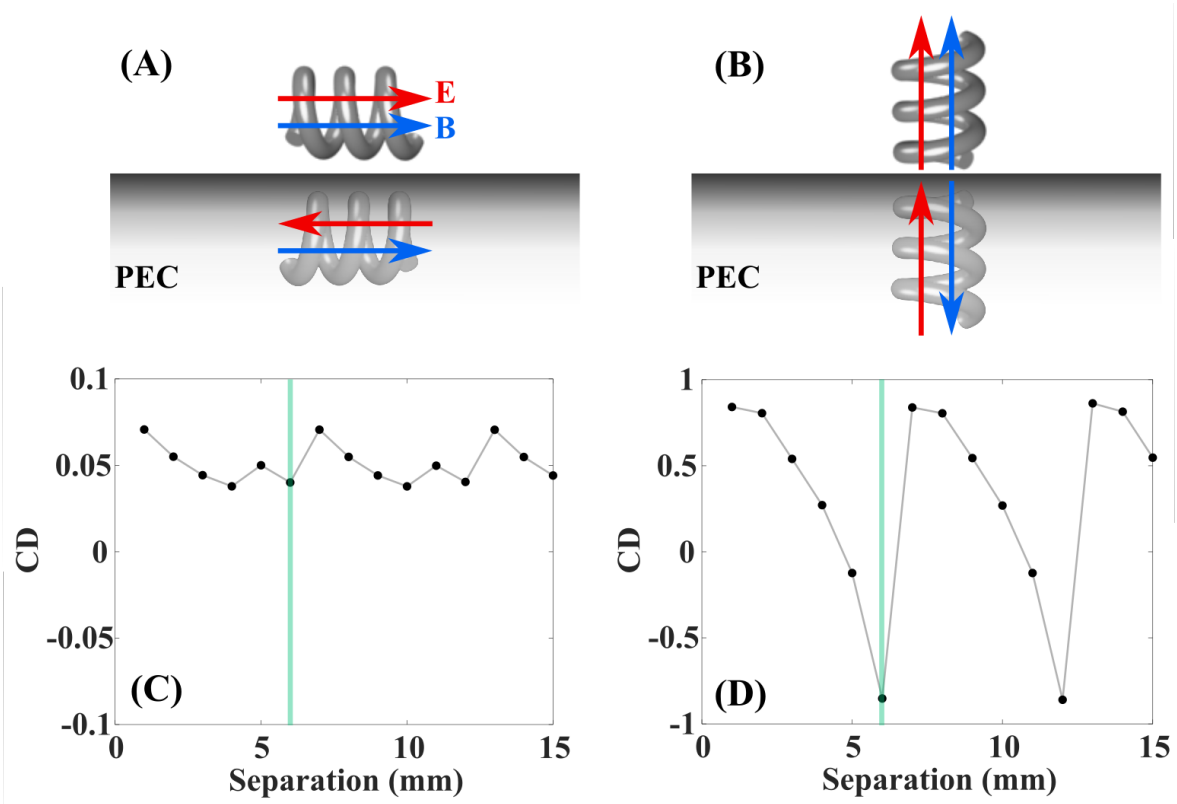

FIGURE 7.3: **Circular dichroism (CD) from helices next to mirrors.** **(A)** and **(B)** are diagrams of the in-plane and out-of-plane helices next to a perfectly electrically conducting (PEC) mirror. Electric (red arrows) and magnetic (blue arrows) dipoles for the original and image helices show a change in handedness upon reflection in both cases. **(C)** and **(D)** are the CD in reflection from arrays of in-plane and out-of-plane helices respectively. The green line highlights the separation at which one half-wavelength fits between the mirror and the closest edge of the helices.

the mirror and the lower edge of the helices. In figure 7.3 (D) the helices have been rotated so they are aligned normal to the surface of the mirror, and a huge increase in the measured CD is seen. The CD oscillates between negative and positive, depending on the separation of mirror and helices in relation to the wavelength. This is very similar to the Drexhage effect that acts on molecules close to mirrors [150].

These surprising results are worthy of further investigation, both to search for new methods to characterise chiral molecules and understand better the subtle consequences of chiroptical interactions between molecules and reflecting surfaces. In addition such a system could be very useful for narrow-band, tunable polarisers, particularly since at optical wavelengths the required shift in the position of chiral material is small. There are many other possible systems that could provide interesting findings. For example, with the use of metasurfaces it is possible to design mirrors with unusual surface impedances, from perfect magnetic conductors [177] to those that are actively tunable [178], and it would be interesting to see how this would alter the results outlined above. The study could also be extended to look at chiral layers inside cavities of different heights and made of different mirrors.

7.3 Orbital Angular Momentum for Enhanced Chiral Detection

Another potential route to observing enhanced chiroptical interactions is through the presence of orbital angular momentum (OAM). Optical beams with OAM can be created using a diffraction grating [46], and this technique could be easily applied at GHz frequencies.

A proposed experimental set-up is shown in figure 7.4. A diffraction grating creates beams of light with $l = \pm 1$ orders of OAM, which could each be used to measure the CD in transmission through arrays of aligned helices. If the OAM of

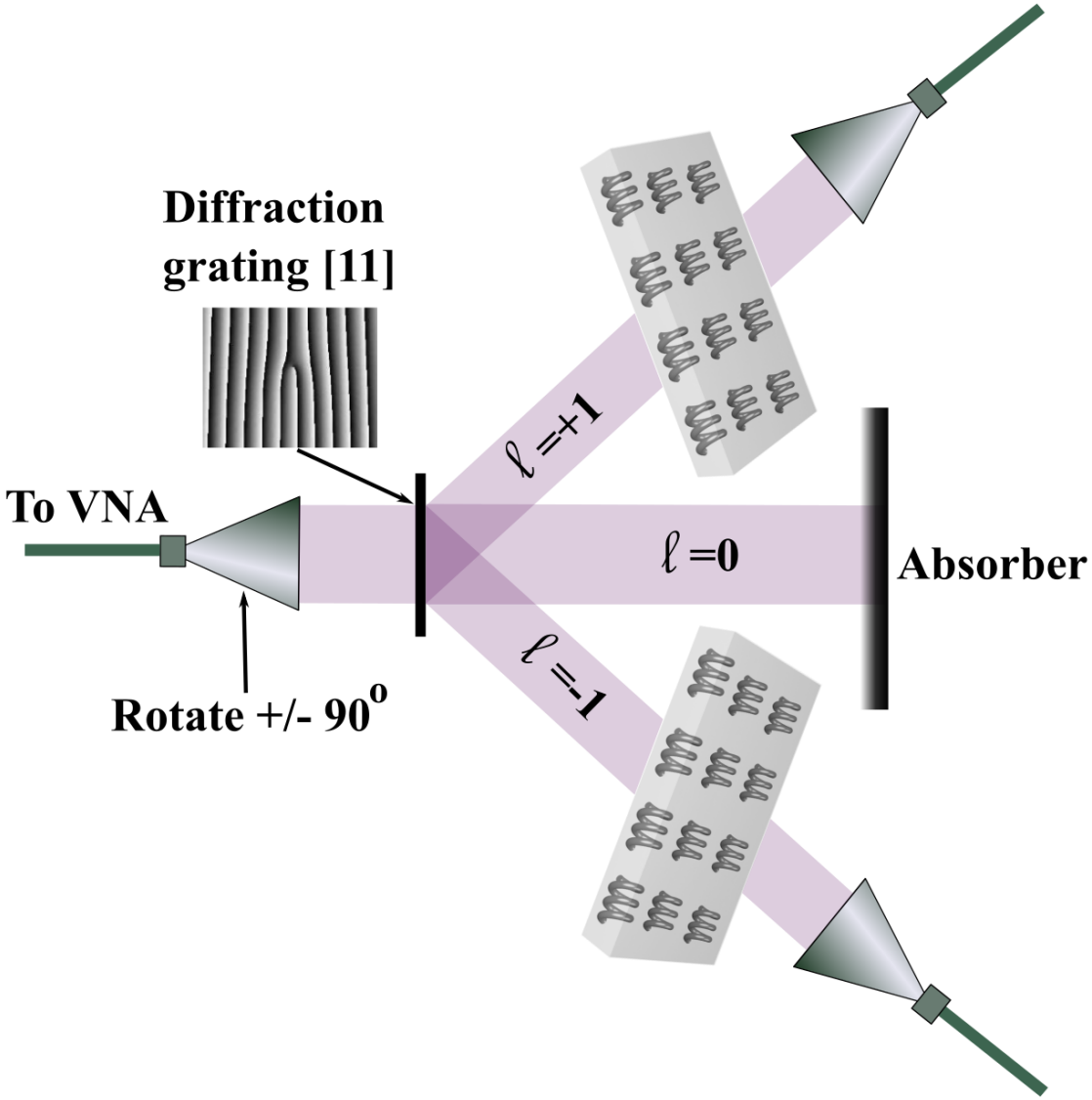

FIGURE 7.4: **Schematic of experiment to measure orbital angular momentum (OAM) contribution to chiroptical interaction.** A linearly polarised beam emitted from a horn antenna is incident on a diffraction grating that emits diffracted beams with positive and negative OAM ($l = \pm 1$) [46]. A layer of aligned helices can be placed alternately into each of these beams and the transmission measured with another horn antenna. The horn antennas can be rotated by 90° so that the circularly polarised transmission coefficients can be found, and the circular dichroism of the helices measured under illumination of beams with positive and negative OAM. The measurement could also be repeated with randomly aligned helices.

the beam is contributing to the measurement, I should see different values of CD depending on the sign of l. A proof would be to compare these results to those measured through an array of randomly oriented helices, where the quadrupole moment should average to zero and we should see no contribution from the OAM. Higher orders of l, with more twist per wavelength, could also be investigated.

It has been shown theoretically that the OAM per unit energy of an evanescent wave is reduced compared to a propagating beam [179]. Testing the interaction between far-field and near-field sources of OAM would yield information about the relation between OAM per unit density, versus the structure of the field, to the contribution to chiroptical interactions. Plasmonic particles that generate fields with OAM have been shown [180], and similar patterns may be created to work at microwave frequencies. As the antennas that are used to generate fields with OAM are themselves planar-chiral, they will have a small CD signal of their own that will need to be taken into account in the analysis.

7.4 Conclusions

This chapter has outlined three suggestions for future work, based on the work presented in the earlier parts of this thesis. Firstly, the CD from chiral arrangements of subwavelength chiral objects, such as small helices arranged in staggered pairs or twisted stacks, were discussed. Preliminary results showed a signal from staggered pairs of helices due to azimuthal rotation between the helices in the pair, but three-dimensional twisted stacks of helices led to more intricate CD spectra.

Secondly, the CD from an array of helices next to reflecting surfaces was suggested as a further topic to study. These spectra are highly dependent on the separation between the helices and mirror in relation to the wavelength, as well as the orientation of the helices. Loss plays an important role in this system, as this is the

cause of the difference in intensity between circular polarisations upon reflection from the mirror.

The final suggested topic is the impact of orbital angular momentum (OAM) on the interaction between a chiral electromagnetic field and a chiral medium, as proposed by recent theoretical work. An experimental method was suggested for probing a helical layer with far-field radiation, and the study could be extended to look at near-fields with OAM, and different arrangements of helices.

Chapter 8

Conclusions

Introduction

This chapter presents the conclusions drawn from each of the studies in chapters 4, 5 and 6 of this thesis, and the suggestions for future work in chapter 7. It finishes with a summary of the findings from the entire thesis, and a comment on the projected future of this field of study.

8.1 Chapter 4 - Pure Optical Rotation from a Twisted-Cross Metasurface

In chapter 4 the broadband, pure optical rotation in twisted cross metamaterials was studied. Two distinct cases were compared: a bilayer structure comprising of arrays of metallic crosses where the crosses in the second layer are twisted (cross/cross), and the case where the second layer is instead and array of complementary crosses (cross/c-cross). In both structures, pure optical rotation occurs in a frequency band between two transmission minima, where alignment of electric and magnetic dipole moments occurs. The natures of these resonances are different in the different systems. In the cross/c-cross structure the image currents in the c-cross layer are always out of phase with those in the cross layer, i.e. antisymmetric, while the cross/cross structure exhibits symmetric and antisymmetric resonances. For the cross/c-cross, this gives rise to a broad region of pure, near dispersionless optical rotation (OR) spanning a range from 19.0 GHz to 37.7 GHz, which is also a region of maximum transmission. The bandwidth and magnitude of the OR are found to be relatively independent of layer separation. This makes the cross/c-cross an ideal candidate for optical rotatory materials in the transmission geometry.

8.2 Chapter 5 - Probing Chiral Media with Chiral Electromagnetic Near-Fields

In chapter 5 the chiral electromagnetic (EM) near-fields generated by an array of staggered-rod antennas were investigated. An layer of subwavelength metallic helices acted as a probe of the chiral fields. The chiral antenna dichroism (CAD) was used as a measure of the interaction strength between the chiral near-fields and

helices. This represented the difference in transmission through the combined antenna and helix system upon changing the handedness of the antennas. This was measured experimentally, and compared to a model of an equivalent homogeneous medium. It was found that the CAD of the helical layer could be predicted fairly accurately by approximating it as a homogeneous chiral material. This work was a method to probe the contribution to a chiral interaction from multipolar terms (as proposed originally by Hendry et al, Nat. Nanotech., 2010), where the chirality of biomolecules was detected with increased sensitivity using chiral plasmonic particles. The work in this chapter has shown that the non-local contribution to the chiral interaction, due to the structure of the evanescent chiral field, is minimal. However other effects, such as enhanced field intensity, absorption and alignment of molecules may account for the results reported in previous publications.

8.3 Chapter 6 - Broadband Dispersionless Slow Waves on Long Helices

In chapter 6 the EM waves bound to an infinitely long metal helix were investigated. Two modes were measured in the experiment - an axial mode that dispersed along the light line, and a helical mode with a high mode index. Due to the screw symmetry of the helix, the helical mode did not have a band-gap at the edge of the Brillouin zone, and had a large region of constant mode index that could be predicted by a geometrical model based on the length of the wire in one turn. An analytical model for the dispersion gave insight into the origins of the lower frequency limit to the constant mode index, which depended on the decay length of fields around the helix compared to the size of the helix itself. The upper frequency limit was set by the interference of the axial and helical modes on the helix, and was found to be inversely proportional to the mode index. Finally, the addition of a straight wire in the centre

of the helix was found to improve the linearity of the dispersion by forcing a faster decay in the electric fields, and weakening the interaction between helical and axial modes.

8.4 Chapter 7 - Future Work

Chapter 7 outlined three suggestions for future work based on the work presented in the earlier parts of this thesis. Firstly, the circular dichroism (CD) from chiral arrangements of subwavelength helices arranged in two and three dimensional chiral unit cells was discussed. Preliminary results showed a signal from staggered pairs of helices due to azimuthal rotation between the helices in the pair, but three-dimensional twisted stacks of helices led to more intricate CD spectra. Secondly, the CD from an array of helices next to reflecting surfaces was suggested. Initial spectra were found to be highly dependent on the separation and orientation of the helices, and due to the loss in the surrounding material. The final suggested topic was the use of orbital angular momentum to enhance the detection of the chirality as proposed by recent theoretical work (Forbes et al, Opt. Lett., 2018). An experimental method was suggested for probing a helical layer with far-field radiation, and the study could be extended to look at near-fields with OAM, and different arrangements of helices.

8.5 Final Comment

The work presented in this thesis has been mostly of a fundamental nature. The aim was to gain a better understanding of how electromagnetic fields can interact with and be manipulated by chiral structures. The experiments and simulations were carried out in the microwave part of the electromagnetic spectrum, where the wavelength is on the order of millimetres, and the structures can be designed and built

on a similar length scale. The fairly large scale afforded better control of sample fabrication and measurement, and the results granted new insights into chiroptical interactions in three regimes - propagating plane-waves, evanescently decaying near-fields and waves bound to an interface.

In each chapter, some recommendations for applications were suggested, where the results obtained might be put to use. This could be in higher bandwidth optical communications thanks to efficient and accurate polarisation manipulation, or more refined, cheaper sensors of small concentrations of chiral molecules for economic drug production, or increased light-matter interactions for efficient solar-cells and compact data storage devices. The future of all the work presented here lies in the journey towards implementation in technology that will, hopefully, improve the lives of this and future generations.

Chapter 9

Publications and Conferences

9.1 Publications

- Barr, L. E., Diaz-Rubio, A. Tremain, B., Carbonell, J., Sanchez-Dehesa, J., Hendry, E., Hibbins, A. P. On the origin of pure optical rotation in twisted-cross metamaterials. *Sci. Rep.* **6**, 30307 (2016).

- Yang, B., Guo, Q., Tremain, B., Barr, L. E., Gao, W., Liu, H., Beri, B., Xiang, Y., Fan, D., Hibbins, A. P., Zhang, S. Direct observation of topological surface-state arcs in photonic metamaterials. *Nat. Comm.* **8**, 1-7 (2017).

- Yang, B., Guo, Q., Tremain, B., Liu, R., Barr, L. E., Yan, Q., Gao, W., Liu, H., Xiang, Y., Chen, J., Fang, c., Hibbins, A., Lu, L., Zhang, S. Ideal Weyl points and helicoid surface states in artificial photonic crystal structures. *Science* **1221**, 1-8 (2018).

- Barr, L. E., Horsley, S. A. R., Hooper, I. R., Eager, J. K., Gallagher, C. P., Hornett, S. M., Hibbins, A. P., Hendry, E. Investigating the nature of chiral near-field interactions. *Phys. Rev. B* **97**, 155418 (2018).

9.2 Conferences

9.2.1 Oral Presentations

- CIMTEC Conference on Smart Materials: Barr, L. E., Horsley, S. A. R., Hornett, S. M., Eager, J., Hooper, I. R., Hibbins, A. P., Hendry, E. Towards Enhanced Chirality in the Near-Field of Electromagnetic Metamaterials. Perugia, Italy. June 2016.

- EM Modelling and Simulations for RF and Microwave Applications: Barr, L. E., Horsley, S. A. R., Hornett, S. M., Eager, J., Hooper, I. R., Hibbins, A. P., Hendry, E. Investigating Near-Field Chiral Interactions Using Handed Metamaterials. Nottingham, England. November 2016.

- Metamaterials2017: Barr, L. E., Horsley, S. A. R., Hornett, S. M., Eager, J., Hooper, I. R., Hibbins, A. P., Hendry, E. Near-Field Interactions in Metamaterials. Marseille, France. August 2017.

- Recent Appointees in Materials Science 2017: Barr, L. E., Horsley, S. A. R., Hornett, S. M., Eager, J., Hooper, I. R., Hibbins, A. P., Hendry, E. On the Nature of Chiral Near-Field Interactions in Metamaterials. Exeter, England. September 2017.

- Exeter Microwave Metamaterials Meeting 2017: Barr, L. E., Horsley, S. A. R., Hornett, S. M., Eager, J., Hooper, I. R., Hibbins, A. P., Hendry, E. On the Nature of Chiral Near-Field Interactions. Exeter, England. December 2017.

9.2.2 Poster Presentations

- Royal Society Conference on Spatial Transformations: Barr, L. E., Diaz-Rubio, A. Tremain, B., Carbonell, J., Sanchez-Dehesa, J., Hendry, E., Hibbins, A. P. Chiral Phenomena in the Near-Field of Handed Metamaterials. Buckinghamshire,

England. January 2015.

- Optical Polarisation Conversion in the Near Field: Barr, L. E., Diaz-Rubio, A. Tremain, B., Carbonell, J., Sanchez-Dehesa, J., Hendry, E., Hibbins, A. P. The Origin of Pure Optical Rotation in Chiral Metamaterials. Exeter, England. June 2015.

- EUPROMETA Fundamentals of Metamaterial Electromagnetics: Barr, L. E., Diaz-Rubio, A. Tremain, B., Carbonell, J., Sanchez-Dehesa, J., Hendry, E., Hibbins, A. P. The Origin of Pure Optical Rotation in Chiral Metamaterials. Ruka, Finland. December 2015.

- Defence Materials Forum: Barr, L. E., Diaz-Rubio, A. Tremain, B., Carbonell, J., Sanchez-Dehesa, J., Hendry, E., Hibbins, A. P. The Origin of Pure Optical Rotation in Chiral Metamaterials. Exeter, England. May 2016.

- Nano-Meta 2017: Barr, L. E., Horsley, S. A. R., Hornett, S. M., Eager, J., Hooper, I. R., Hibbins, A. P., Hendry, E. Investigating Chiral Near-Fields Using Handed Metamaterials. Seefeld, Austria. January 2017.

Appendix A

Derivation of Helical Fourier Transform

The following derivation is relevant to chapter 5.

In chapter 5, the Fourier transform (FT) of the electric fields above a staggered-rod antenna is plotted in terms of right and left circularly polarised (R/LCP) waves. The following is an account of the derivation of the helical FT. The FT of the x, y and z components of the field are first converted into S and P polarisations, as defined in figure A.1, then converted into RCP and LCP components.

The complex electric field in a plane above the structure of interest can be written as:

$$\mathbf{E}(x,y,z) = \sum_{n_1,n_2} \left[\varepsilon_{\mathrm{S}}\left(n_1,n_2\right)\hat{e_1} + \varepsilon_{\mathrm{P}}\left(n_1,n_2\right)\hat{e_2}\right] e^{ik_{\mathrm{x}}(n_1)x} e^{ik_{\mathrm{y}}(n_2)y} e^{ik_{\mathrm{z}}(n_{1,2})z} \tag{A.1}$$

The wave-vectors along x, y and z are:

$$k_{\mathrm{x}} = \frac{2\pi n_1}{d} \tag{A.2}$$

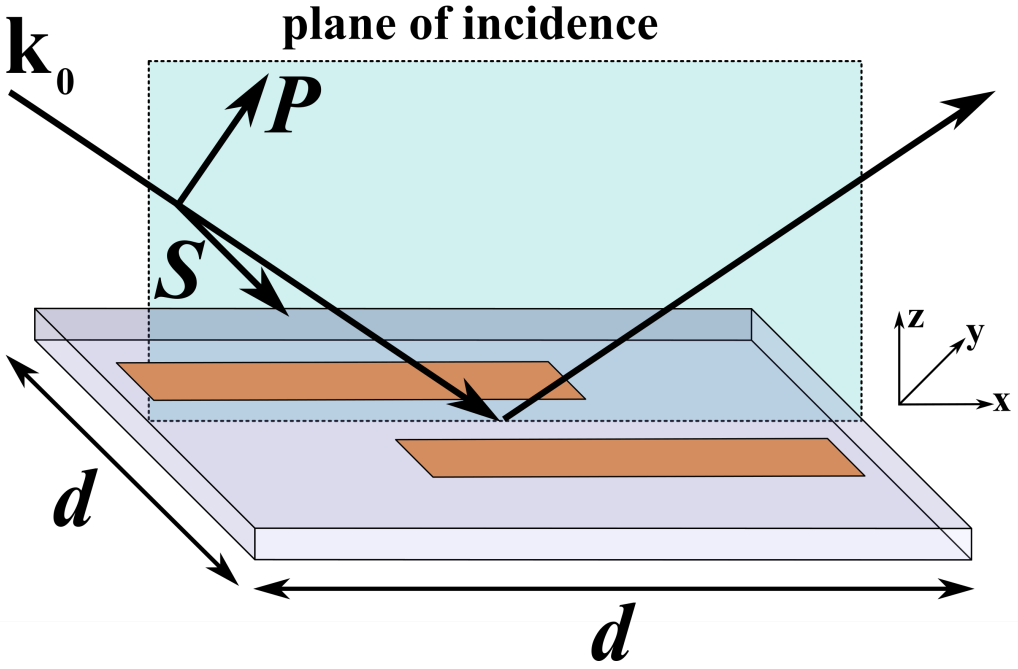

FIGURE A.1: **Geometry of the problem.** The plane of incidence is shown as the pale blue sheet, with the S and P polarisation vectors indicated with respect to the incident wave-vector, k_0. d is the period of the array.

$$k_y = \frac{2\pi n_2}{d} \tag{A.3}$$

$$k_z = \sqrt{k_0^2 - \left(\frac{2\pi n_1}{d}\right)^2 - \left(\frac{2\pi n_2}{d}\right)^2} \tag{A.4}$$

where $\varepsilon_{S,P}$ is the Fourier amplitude of the S and P unit vectors, d is the period of the array, shown in figure A.1, and $n_{1,2}$ is the number of pixels measured along x and y. For simplicity $n_1 = n_2$. The unit vectors that define S and P polarisations are:

$$S \equiv \hat{e_1} = \hat{z} \times \hat{k_{||}} = \hat{z} \times \frac{k_x\hat{x} + k_y\hat{y}}{\sqrt{k_x^2 + k_y^2}} \tag{A.5}$$

and

$$P \equiv \hat{e_2} = \hat{k_0} \times \hat{e_1} \tag{A.6}$$

Splitting the complex electric field in equation A.1 into the components along x and y:

$$E_{\mathrm{x}}(x,y,z) = \sum_{n_1,n_2} \left[\varepsilon_{\mathrm{S}}\hat{x}\cdot\hat{e_1} + \varepsilon_{\mathrm{P}}\hat{x}\cdot\hat{e_2}\right] e^{ik_{\mathrm{x}}(n_1)x} e^{ik_{\mathrm{y}}(n_2)y} e^{ik_{\mathrm{z+}}(n_{1,2})z} \tag{A.7}$$

$$E_{\mathrm{y}}(x,y,z) = \sum_{n_1,n_2} \left[\varepsilon_{\mathrm{S}}\hat{y}\cdot\hat{e_1} + \varepsilon_{\mathrm{P}}\hat{y}\cdot\hat{e_2}\right] e^{ik_{\mathrm{x}}(n_1)x} e^{ik_{\mathrm{y}}(n_2)y} e^{ik_{\mathrm{z\text{-}}}(n_{1,2})z} \tag{A.8}$$

To find the component of the electric field along the direction of S and P polarisation, the dot products between the S and P unit vectors and the x and y electric field components are taken.

$$\begin{aligned}\hat{x}\cdot\hat{e_1} &= \hat{x}\cdot\frac{\hat{z}\times\left(k_{\mathrm{x}}\hat{x}+k_{\mathrm{y}}\hat{y}\right)}{\sqrt{k_{\mathrm{x}}^2+k_{\mathrm{y}}^2}} \\ &= \frac{-k_{\mathrm{y}}}{\sqrt{k_{\mathrm{x}}^2+k_{\mathrm{y}}^2}}\end{aligned} \tag{A.9}$$

$$\begin{aligned}\hat{x}\cdot\hat{e_2} &= \hat{x}\cdot\frac{\hat{k_0}\times\hat{z}\times\left(k_{\mathrm{x}}\hat{x}+k_{\mathrm{y}}\hat{y}\right)}{\sqrt{k_{\mathrm{x}}^2+k_{\mathrm{y}}^2}} \\ &= \hat{x}\cdot\frac{\left(k_{\mathrm{x}}\hat{x}+k_{\mathrm{y}}\hat{y}++k_{\mathrm{z}}\hat{z}\right)\times\hat{z}\times\left(k_{\mathrm{x}}\hat{x}+k_{\mathrm{y}}\hat{y}\right)}{k_0\sqrt{k_{\mathrm{x}}^2+k_{\mathrm{y}}^2}} \\ &= \frac{-k_{\mathrm{z}}k_{\mathrm{x}}}{k_0\sqrt{k_{\mathrm{x}}^2+k_{\mathrm{y}}^2}}\end{aligned} \tag{A.10}$$

$$\begin{aligned}\hat{y}\cdot\hat{e_1} &= \hat{y}\cdot\frac{\hat{z}\times\left(k_{\mathrm{x}}\hat{x}+k_{\mathrm{y}}\hat{y}\right)}{\sqrt{k_{\mathrm{x}}^2+k_{\mathrm{y}}^2}} \\ &= \frac{k_{\mathrm{x}}}{\sqrt{k_{\mathrm{x}}^2+k_{\mathrm{y}}^2}}\end{aligned} \tag{A.11}$$

$$\begin{aligned}\hat{y}\cdot\hat{e_2} &= \hat{y}\cdot\frac{\hat{k_0}\times\hat{z}\times\left(k_x\hat{x}+k_y\hat{y}\right)}{\sqrt{k_x^2+k_y^2}}\\ &= \hat{x}\cdot\frac{\left(k_x\hat{x}+k_y\hat{y}++k_z\hat{z}\right)\times\hat{z}\times\left(k_x\hat{x}+k_y\hat{y}\right)}{k_0\sqrt{k_x^2+k_y^2}}\\ &= \frac{-k_yk_z}{k_0\sqrt{k_x^2+k_y^2}}\end{aligned} \tag{A.12}$$

Substituting the equations for the dot products (A.9, A.10, A.11 and A.12) into the equations for the complex electric field (A.7 and A.8), and taking the FT of both sides gives:

$$\mathcal{F}[E_x] = \varepsilon_S\left(\frac{-k_y}{\sqrt{k_x^2+k_y^2}}\right)+\varepsilon_P\left(\frac{-k_xk_z}{k_0^2\sqrt{k_x^2+k_y^2}}\right) \tag{A.13}$$

$$\mathcal{F}[E_y] = \varepsilon_S\left(\frac{k_x}{\sqrt{k_x^2+k_y^2}}\right)+\varepsilon_P\left(\frac{-k_yk_z}{k_0^2\sqrt{k_x^2+k_y^2}}\right) \tag{A.14}$$

Rearranging to find the S and P Fourier amplitudes:

$$\varepsilon_S = \frac{k_x\mathcal{F}[E_x]-k_y\mathcal{F}[E_y]}{k_0^2\sqrt{k_x^2+k_y^2}} \tag{A.15}$$

$$\varepsilon_P = -\left(\frac{k_0}{k_z}\right)\frac{k_x\mathcal{F}[E_x]+k_y\mathcal{F}[E_y]}{k_0^2\sqrt{k_x^2+k_y^2}} \tag{A.16}$$

These can then be used to find the Fourier amplitudes of the left (-) and right (+) helical components of the field:

$$\varepsilon_+ = \frac{\varepsilon_S - i\varepsilon_P}{\sqrt{2}} \tag{A.17}$$

$$\varepsilon_{-} = \frac{\varepsilon_{S} + i\varepsilon_{P}}{\sqrt{2}} \tag{A.18}$$

These are the helical FT components calculated in figure 5.2 in chapter 5, showing the difference in wave-vector components in chiral evanescent fields above and below a planar-chiral antenna.

Appendix B

Derivation of Sheath Helix Dispersion Relation

The following derivation is relevant to chapter 6.

In this appendix, the dispersion relation for a wave bound to a helix is derived. The geometry of the problem is as depicted in figure B.1.
We start with Maxwell's equations:

$$\nabla \times \bar{E} = -i\omega\mu\bar{H} \tag{B.1}$$

$$\nabla \times \bar{H} = i\omega\epsilon\bar{E} \tag{B.2}$$

where $\bar{E}$ and $\bar{H}$ are the electric and magnetic fields, μ and ϵ are the permittivity and permeability of the surrounding medium (assumed to be free space throughout this work), ω is the frequency of the incident radiation, ∇ means differentiation with respect to the three Cartesian spacial coordinates. The solutions to Maxwell's equations can be written in terms of Hertzian vector potentials, $\bar{\Pi}$, that are defined using the scalar ϕ and vector $\bar{A}$ potentials:

$$\phi = -\nabla \cdot \bar{\Pi} \tag{B.3}$$

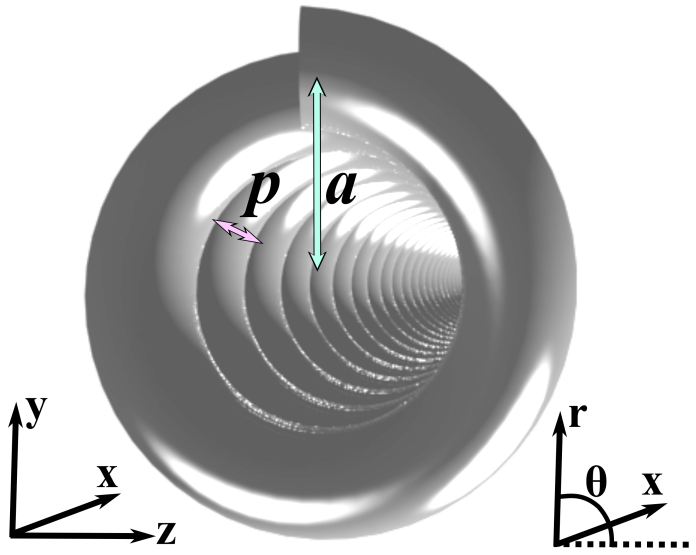

FIGURE B.1: **Geometry of the problem.** The parameters are the same as those used in chapter 6. a is the helix radius and p is the helix pitch. The Cartesian and cylindrical coordinate systems are also illustrated.

$$\bar{A} = \mu\epsilon\frac{\partial\bar{\Pi}}{\partial t} \tag{B.4}$$

The solutions to the wave equation in this approach are:

$$\bar{E} = \nabla\times\nabla\times\bar{\Pi} - i\omega\mu\nabla\times\bar{\Pi}^* \tag{B.5}$$

$$\bar{H} = \nabla\times\nabla\times\bar{\Pi}^* + i\omega\epsilon\nabla\times\bar{\Pi} \tag{B.6}$$

Both $\bar{\Pi}$ and $\bar{\Pi}^*$ satisfy the same wave equation:

$$\nabla\times\nabla\times\bar{\Pi} - \nabla\nabla\cdot\bar{\Pi} - k^2\bar{\Pi} = 0 \tag{B.7}$$

$$\nabla\times\nabla\times\bar{\Pi}^* - \nabla\nabla\cdot\bar{\Pi}^* - k^2\bar{\Pi}^* = 0 \tag{B.8}$$

Assuming that $\bar{\Pi}$ and $\bar{\Pi}^*$ have only components along the direction of the helix

axis, x, equations B.5 and B.6 can be expanded, and the electric and magnetic fields written in cylindrical coordinates:

$$E_{\mathrm{r}} = \frac{\partial^2 \Pi_{\mathrm{x}}}{\partial x \partial r} - \frac{i\omega\mu}{r}\frac{\partial \Pi_{\mathrm{x}}^*}{\partial \theta} \tag{B.9}$$

$$E_{\theta} = \frac{1}{r}\frac{\partial^2 \Pi_{\mathrm{x}}}{\partial x \partial \theta} + i\omega\mu\frac{\partial \Pi_{\mathrm{x}}^*}{\partial r} \tag{B.10}$$

$$E_{\mathrm{x}} = \frac{\partial^2 \Pi_{\mathrm{x}}}{\partial x^2} + k^2 \Pi_{\mathrm{x}} \tag{B.11}$$

$$H_{\mathrm{r}} = \frac{\partial^2 \Pi_{\mathrm{x}}^*}{\partial x \partial r} + \frac{i\omega\epsilon}{r}\frac{\partial \Pi_{\mathrm{x}}}{\partial \theta} \tag{B.12}$$

$$H_{\theta} = \frac{1}{r}\frac{\partial^2 \Pi_{\mathrm{x}}^*}{\partial x \partial \theta} - i\omega\epsilon\frac{\partial \Pi_{\mathrm{x}}}{\partial r} \tag{B.13}$$

$$H_{\mathrm{x}} = \frac{\partial^2 \Pi_{\mathrm{x}}^*}{\partial x^2} + k^2 \Pi_{\mathrm{x}}^* \tag{B.14}$$

Now, Π_{x} and Π_{x}^* satisfy the same scalar wave equation:

$$\nabla^2 \Pi_{\mathrm{x}} + k^2 \Pi_{\mathrm{x}} = \frac{1}{r}\frac{\partial}{\partial r}\left(r\frac{\partial \Pi_{\mathrm{x}}}{\partial r}\right) + \frac{1}{r^2}\frac{\partial^2 \Pi_{\mathrm{x}}}{\partial \theta^2} + \frac{\partial^2 \Pi_{\mathrm{x}}}{\partial z^2} + k^2 \Pi_{\mathrm{x}} = 0 \tag{B.15}$$

$$\nabla^2 \Pi_{\mathrm{x}}^* + k^2 \Pi_{\mathrm{x}}^* = \frac{1}{r}\frac{\partial}{\partial r}\left(r\frac{\partial \Pi_{\mathrm{x}}^*}{\partial r}\right) + \frac{1}{r^2}\frac{\partial^2 \Pi_{\mathrm{x}}^*}{\partial \theta^2} + \frac{\partial^2 \Pi_{\mathrm{x}}^*}{\partial z^2} + k^2 \Pi_{\mathrm{x}}^* = 0 \tag{B.16}$$

Taking only the Π_{x} component for illustration, it can be separated into three variables, each dependent on one of the spatial coordinates:

$$\Pi_{\mathrm{x}}(r, \theta, x) = R(r)\Theta(\theta)X(x) \tag{B.17}$$

Filling this into equation B.15, the wave equation can then be written:

$$\frac{1}{r}\frac{\mathrm{d}}{\mathrm{d}r}\left(r\frac{\mathrm{d}R}{\mathrm{d}r}\right)\Theta X + \frac{1}{r^2}\frac{\mathrm{d}^2\Theta}{\mathrm{d}\theta^2}RX + \frac{\mathrm{d}^2X}{\mathrm{d}x^2}R\Theta + k^2R\Theta Z = 0 \tag{B.18}$$

Define some new variables:

$$\frac{1}{X}\frac{\mathrm{d}^2X}{\mathrm{d}x^2} = A = -\beta^2 \tag{B.19}$$

$$\frac{1}{\Theta}\frac{\mathrm{d}^2\Theta}{\mathrm{d}\theta^2} = B = -n^2 \tag{B.20}$$

The negative sign is added to β to ensure that the fields decay exponentially, not grow, as a function of x. n must be an integer so that the fields obey 2π periodicity in the radial direction. Divide equation B.18 by $RZ\Theta$, multiply by r^2 and substitute for A and B, to find:

$$\frac{r}{R}\frac{\mathrm{d}}{\mathrm{d}r}\left(r\frac{\mathrm{d}R}{\mathrm{d}r}\right) + \left(A + k^2\right)r^2 + B = 0 \tag{B.21}$$

The separated variables have been found:

$$\left.\begin{aligned} X &= e^{-i\beta x} \\ \Theta &= e^{-inx} \\ R(r) &= f(r) \end{aligned}\right\} \quad \Pi_{\mathrm{x}} = f(r)e^{-i\beta z}e^{-in\theta} \tag{B.22}$$

Multiplying the wave equation, equation B.21, by R and substituting in n and β results in:

$$r^2\frac{\mathrm{d}^2R}{\mathrm{d}r^2} + r\frac{\mathrm{d}R}{\mathrm{d}r} - \left[\left(\beta^2 - k^2\right)r^2 + n^2\right]R = 0 \tag{B.23}$$

Define a new value, γa, where a is the helix radius and γ is the relative wave-vector:

$$\gamma a = \sqrt{\beta^2 - k^2} r \tag{B.24}$$

$$\frac{\mathrm{d}}{\mathrm{d}r} = \sqrt{\beta^2 - k^2} \frac{\mathrm{d}}{\mathrm{d}(\gamma a)} \tag{B.25}$$

Substituting for γa in equation B.23, results in the modified Bessel differential equation of argument γa:

$$(\gamma a)^2 \frac{\mathrm{d}^2 R}{\mathrm{d}\,(\gamma a)^2} + (\gamma a) \frac{\mathrm{d}R}{\mathrm{d}\,(\gamma a)} - \left((\gamma a)^2 + n^2\right) R = 0 \tag{B.26}$$

To ensure the fields are finite, modified Bessel functions of the first kind (I_n) are chosen to describe fields and vector potentials inside the helix, denoted by subscript i, and modified Bessel functions of the second kind (K_n) are chosen for fields and vector potentials outside the helix, denoted by subscript e. Therefore the vector potentials are:

$$\Pi_\mathrm{x}^\mathrm{i} = A_\mathrm{n}^\mathrm{i} I_\mathrm{n}(\gamma r)\, e^{-i\beta x} e^{-in\theta} \tag{B.27}$$

$$\Pi_\mathrm{x}^\mathrm{e} = A_\mathrm{n}^\mathrm{e} K_\mathrm{n}(\gamma r)\, e^{-i\beta x} e^{-in\theta} \tag{B.28}$$

$$\Pi_\mathrm{x}^{*\mathrm{i}} = B_\mathrm{n}^\mathrm{i} I_\mathrm{n}(\gamma r)\, e^{-i\beta x} e^{-in\theta} \tag{B.29}$$

$$\Pi_\mathrm{x}^{*\mathrm{i}} = B_\mathrm{n}^\mathrm{i} K_\mathrm{n}(\gamma r)\, e^{-i\beta x} e^{-in\theta} \tag{B.30}$$

A and B are coefficients that are functions of n and ω but not r. Using the expressions for the Hertzian dipoles above in equations B.10, B.11, B.13 and B.14 gives the

tangential electric and magnetic fields. Then apply the following boundary conditions:

$$E_{\mathrm{x}}^{\mathrm{i}} = E_{\mathrm{x}}^{\mathrm{e}} \tag{B.31}$$

$$E_{\theta}^{\mathrm{i}} = E_{\theta}^{\mathrm{e}} \tag{B.32}$$

$$E_{\mathrm{x}}^{\mathrm{i,e}} = -E_{\mathrm{x}}^{\mathrm{i,e}} \mathrm{cot}\psi \tag{B.33}$$

$$H_{\mathrm{x}}^{\mathrm{i}} + H_{\theta}^{i} \mathrm{cot}\psi = H_{\mathrm{x}}^{\mathrm{e}} + H_{\theta}^{\mathrm{e}} \mathrm{cot}\psi \tag{B.34}$$

where ψ is the helix pitch angle, and is calculated:

$$\psi = \mathrm{cot}^{-1}\left(\frac{2\pi a}{p}\right) \tag{B.35}$$

Equations B.31 and B.32 state that the tangential electric field at the boundary $r = a$ must be continuous. Equation B.33 ensures that the electric field is periodic along the helix axis in a way that is consistent with the turns of the helix, and that currents flow only along the direction of the turns. Equation B.34 states that the perpendicular magnetic fields are continuous across the boundary.

Applying the boundary conditions the solution of the system of linear equations for coefficients A and B can be found:

$$A_{\mathrm{n}}^{\mathrm{e}} = \frac{I_{\mathrm{n}}}{K_{\mathrm{n}}} A_{\mathrm{n}}^{\mathrm{i}} \tag{B.36}$$

$$B_{\mathrm{n}}^{\mathrm{i}} = \frac{\gamma^2 + \frac{\beta n}{a}\mathrm{cot}\psi}{i\omega\mu\gamma\mathrm{cot}\psi} \frac{I_{\mathrm{n}}}{I_{\mathrm{n}}'} A_{\mathrm{n}}^{\mathrm{i}} \tag{B.37}$$

$$B_{\mathrm{n}}^{\mathrm{e}} = \frac{I_{\mathrm{n}}'}{K_{\mathrm{n}}'} B_{\mathrm{n}}^{\mathrm{i}} = \frac{\gamma^2 + \frac{\beta n}{a}\mathrm{cot}\psi}{i\omega\mu\gamma\mathrm{cot}\psi} \frac{I_{\mathrm{n}}}{K_{\mathrm{n}}'} A_{\mathrm{n}}^{\mathrm{i}} \tag{B.38}$$

The argument for each of the Bessel functions is γa, removed here for clarity, and the prime means differentiate with respect to the argument.

Finally, the determinantal equation for the dispersion of a wave on a helix is found:

$$\frac{I_{\mathrm{n}}'(\gamma a) K_{\mathrm{n}}'(\gamma a)}{I_{\mathrm{n}}(\gamma a) K_{\mathrm{n}}(\gamma a)} = \frac{\left(\gamma^2 \mathrm{a}^2 + \beta n a \mathrm{cot}\psi\right)^2}{k^2 a^2 \gamma^2 a^2 \mathrm{cot}^2\psi} \tag{B.39}$$

This is the equation used to find the dispersion of a wave on an infinitely long helix in chapter 6. The solution is found through implementation of a minimisation algorithm. It finds the values of β at various incident wave-vectors for which the difference between the right and left sides of the equation is minimal.

Bibliography

1. Poisson, S.-D., Arago, F. & Biot, J.-B. *Memoires de la Classe des Sciences Mathematiques et Physiques* 1st (Chez Firmin Didot, Imprimeur de l'Institut Imperial de France at Librarie pour le Mathematiques, 24 rue Jacob, Paris, 1811).
2. Kelvin, W. T. *The molecular tactics of a crystal* 65 (Oxford University Press, 1894).
3. Pasteur, L. *et al. Lecons de Chimie Professees en 1860* 1st (Societe Chimique de Paris, Paris, 1861).
4. Lindell, I.V., Sihvola, A. H., Tretyakov, S. A., Viitanen, A. J. *Electromagnetic Waves in Chiral and Bi-Isotropic Media* 1st, 332 (Artech House Inc., 1994).
5. Bose, J. C. On the Rotation of Plane of Polarisation of Electric Waves by a Twisted Structure. *Proceedings of the Royal Society of London (1854-1905)* **63,** 146–152 (1898).
6. Barron, L. True and false chirality and parity violation. *Chemical Physics Letters* **123,** 423–427 (1986).
7. Barron, L. D. True and false chirality and absolute asymmetric synthesis. *Journal of the American Chemical Society* **108,** 5539–5542 (1986).
8. Bliokh, K. Y., Kivshar, Y. S. & Nori, F. Magnetoelectric effects in local light-matter interactions. *Physical Review Letters* **113,** 1–6 (2014).
9. Bliokh, K. Y., Bekshaev, A. Y. & Nori, F. Dual electromagnetism: Helicity, spin, momentum and angular momentum. *New Journal of Physics* **15.** arXiv: 1208.4523 (2013).

10. Narushima, T., Hashiyada, S. & Okamoto, H. Nanoscopic Study on Developing Optical Activity with Increasing Chirality for Two-Dimensional Metal Nanostructures. *ACS Photonics* **1,** 732–738 (2014).

11. Lipkin, D. M. Existence of a New Conservation Law in Electromagnetic Theory. *Journal of Mathematical Physics* **5,** 696 (1964).

12. Tang, Y. & Cohen, A. E. Optical Chirality and Its Interaction with Matter. *Physical Review Letters* **104,** 163901 (2010).

13. Barnett, S. M. *et al.* On the natures of the spin and orbital parts of optical angular momentum. *Journal of Optics* **18,** 064004 (2016).

14. Barron, L. D. *Molecular Light Scattering and Optical Activity* 2nd, 443 (Cambridge University Press, 2004).

15. Schäferling, M., Dregely, D., Hentschel, M. & Giessen, H. Tailoring Enhanced Optical Chirality: Design Principles for Chiral Plasmonic Nanostructures. *Physical Review X* **2,** 031010 (2012).

16. Kuwata-Gonokami, M. *et al.* Giant optical activity in quasi-two-dimensional planar nanostructures. *Physical Review Letters* **95,** 1–4 (2005).

17. Arteaga, O. *et al.* Relation between 2D/3D chirality and the appearance of chiroptical effects in real nanostructures. *Optics Express* **24,** 2242 (2016).

18. Wu, X. *et al.* Anisotropic metasurface with near-unity circular polarization conversion. *Applied Physics Letters* **108,** 183502 (2016).

19. Khanikaev, A. B. *et al.* Experimental demonstration of the microscopic origin of circular dichroism in two-dimensional metamaterials. *Nature Communications* **7,** 12045 (2016).

20. Zhu, A. Y. *et al.* Giant intrinsic chiro-optical activity in planar dielectric nanostructures. *Light: Science & Applications* **7,** 17158 (2018).

21. Plum, E. *et al.* Metamaterials: Optical activity without chirality. *Physical Review Letters* **102,** 1–4 (2009).

22. Collins, J. T. *et al.* Chirality and Chiroptical Effects in Metal Nanostructures: Fundamentals and Current Trends. *Advanced Optical Materials* **5,** 1700182 (2017).

23. Tinoco, I. & Freeman, M. P. The optical activity of oriented copper helices. I. Experimental. *Journal of Physical Chemistry* **61,** 1196–1200 (1957).

24. Pinheiro, F. A., Fedotov, V. A., Papasimakis, N. & Zheludev, N. I. Spontaneous natural optical activity in disordered media. *Physical Review B* **95,** 1–5 (2017).

25. Polavarapu, P. L. Kramers-Kronig transformation for optical rotatory dispersion studies. *Journal of Physical Chemistry A* **109,** 7013–7023 (2005).

26. Mitchell, S. The Cotton Effect. *Monographs on Modern Chemistry* **92,** 552 (1933).

27. Gorkunov, M. V., Dmitrienko, V. E., Ezhov, A. a., Artemov, V. V. & Rogov, O. Y. Implications of the causality principle for ultra chiral metamaterials. *Scientific Reports* **5,** 9273 (2015).

28. Bechhoefer, J. Kramers–Kronig, Bode, and the meaning of zero. *American Journal of Physics* **79,** 1053 (2011).

29. Yin, X., Schäferling, M., Metzger, B. & Giessen, H. Interpreting chiral nanophotonic spectra: The plasmonic Born-Kuhn model. *Nano Letters* **13,** 6238–6243 (2013).

30. Govorov, A. O., Fan, Z., Hernandez, P., Slocik, J. M. & Naik, R. R. Theory of circular dichroism of nanomaterials comprising chiral molecules and nanocrystals: Plasmon enhancement, dipole interactions, and dielectric effects. *Nano Letters* **10,** 1374–1382 (2010).

31. Auguié, B., Alonso-Gómez, J. L., Guerrero-Martínez, A. & Liz-Marzán, L. M. Fingers crossed: Optical activity of a chiral dimer of plasmonic nanorods. *Journal of Physical Chemistry Letters* **2,** 846–851 (2011).

32. Barron, L. Electric quadrupole contributions to the optical activity of crystalline transition metal complexes. *Molecular Physics* **21,** 241–246 (1971).

33. Hendry, E *et al.* Ultrasensitive detection and characterization of biomolecules using superchiral fields. *Nature nanotechnology* **5,** 783–7 (2010).

34. Tang, Y. & Cohen, A. E. Enhanced enantioselectivity in excitation of chiral molecules by superchiral light. *Science (New York, N.Y.)* **332,** 333–336 (2011).

35. Bliokh, K. Y. & Nori, F. Characterizing optical chirality. *Physical Review A - Atomic, Molecular, and Optical Physics* **83,** 1–3 (2011).

36. Choi, J. S. & Cho, M. Limitations of a superchiral field. *Physical Review A - Atomic, Molecular, and Optical Physics* **86,** 1–22 (2012).

37. Alizadeh, M. H. & Reinhard, B. M. Enhanced Optical Chirality through Locally Excited Surface Plasmon Polaritons Abstract : *ACS Photonics* **2,** 942–949 (2015).

38. Maradudin, Alexei A., Sambles, J. Roy, Barnes, W. L. *Modern Plasmonics* 1st (Elsevier B.V., 2014).

39. Davis, T. & Hendry, E. Superchiral electromagnetic fields created by surface plasmons in nonchiral metallic nanostructures. *Physical Review B* **87,** 085405 (2013).

40. Kang, L., Ren, Q. & Werner, D. H. Leveraging Superchiral Light for Manipulation of Optical Chirality in the Near-Field of Plasmonic Metamaterials. *ACS Photonics* **4,** 1298 –1305 (2017).

41. Kelly, C. *et al.* Controlling Metamaterial Transparency with Superchiral Fields. *ACS Photonics* **5,** 535–543 (2018).

42. Kramer, C., Schäferling, M., Weiss, T., Giessen, H. & Brixner, T. Analytic Optimization of Near-Field Optical Chirality Enhancement. *ACS Photonics* **4,** 396–406 (2017).

43. Cameron, R. P., Barnett, S. M. & Yao, A. M. Optical helicity, optical spin and related quantities in electromagnetic theory. *New Journal of Physics* **14** (2012).

44. Philbin, T. G. Lipkin's conservation law, Noether's theorem, and the relation to optical helicity. *Physical Review A - Atomic, Molecular, and Optical Physics* **87** (2013).

45. Fernandez-Corbaton, I. & Rockstuhl, C. Objects of maximum electromagnetic chirality. arXiv: 1508.04049 (2015).

46. Padgett, M. & Allen, L. Light with a twist in its tail. *Contemporary Physics* **41,** 275–285 (2000).

47. Bliokh, K., Rodríguez-Fortuño, F., Nori, F. & Zayats, A. Spin-orbit interactions of light. *ArXiv,* 1505.02864 (2015).

48. Rosales-Guzmán, C., Volke-Sepulveda, K. & Torres, J. P. Light with enhanced optical chirality. *Optics Letters* **37,** 3486 (2012).

49. Molina-Terriza, G., Torres, J. P. & Torner, L. Twisted photons. *Nature Physics* **3,** 305–310 (2007).

50. Forbes, K. A. & Andrews, D. L. Optical orbital angular momentum: twisted light and chirality. *Optics Letters* **43,** 435 (2018).

51. Francote, E. Linder, W. *Chirality in Drug Research* (Wiley-VCH, 2006).

52. Tullius, R. *et al.* "Superchiral" Spectroscopy: Detection of Protein Higher Order Hierarchical Structure with Chiral Plasmonic Nanostructures. *Journal of the American Chemical Society* **137,** 8380 –8383 (2015).

53. Stiles, P. L., Dieringer, J. A., Shah, N. C. & Van Duyne, R. P. Surface-Enhanced Raman Spectroscopy. *Annual Review of Analytical Chemistry* **1,** 601–626 (2008).

54. Campion, A. & Kambhampati, P. Surface-Enhanced Raman Scattering. *Chemical Society Reviews* **27,** 241–250 (1998).

55. Tobing, L. Y. M. *et al.* Polarization invariant plasmonic nanostructures for sensing applications. *Scientific Reports* **7,** 7539 (2017).

56. Birke, R. L., Znamenskiy, V. & Lombardi, J. R. A charge-transfer surface enhanced Raman scattering model from time-dependent density functional theory calculations on a Ag10-pyridine complex. *The Journal of Chemical Physics* **132,** 214707 (2010).

57. Liu, Y. *et al.* Strong superchiral field in hot spots and its interaction with chiral molecules. *EPL (Europhysics Letters)* **110,** 17008 (2015).

58. Schäferling, M., Engheta, N., Giessen, H. & Weiss, T. Reducing the complexity: Enantioselective chiral near-fields by diagonal slit and mirror configuration. *ACS Photonics* **3,** 1076 –1084 (2016).

59. Ma, W. *et al.* Attomolar DNA detection with chiral nanorod assemblies. *Nature Communications* **4,** 1–8 (2013).

60. Davis, T. J. & Gómez, D. E. Interaction of localized surface plasmons with chiral molecules. *Physical Review B* **90,** 235424 (2014).

61. Finazzi, M., Biagioni, P., Celebrano, M. & Duo, L. Quasistatic limit for plasmon-enhanced optical chirality. *Physical Review B - Condensed Matter and Materials Physics* **91,** 1–5 (2015).

62. Meinzer, N., Hendry, E. & Barnes, W. L. Probing the chiral nature of electromagnetic fields surrounding plasmonic nanostructures. *Physical Review B* **88,** 041407 (2013).

63. Wang, R. Y. *et al.* Experimental observation of giant chiroptical amplification of small chiral molecules by gold nanosphere clusters. *Journal of Physical Chemistry C* **118,** 9690–9695 (2014).

64. Wu, L. *et al.* Circular polarization converters based on bi-layered asymmetrical split ring metamaterials. *Applied Physics A: Materials Science and Processing* **116,** 643–648 (2014).

65. Garcia-Etxarri, A. & Dionne, J. A. Surface-enhanced circular dichroism spectroscopy mediated by nonchiral nanoantennas. *Physical Review B - Condensed Matter and Materials Physics* **87,** 1–5 (2013).

66. Jack, C. *et al.* Biomacromolecular Stereostructure Mediates Mode Hybridization in Chiral Plasmonic Nanostructures. *Nano Letters* **16,** 5806–5814 (2016).

67. Gorkunov, M. V., Darinskii, A. N. & Kondratov, A. V. Enhanced sensing of molecular optical activity with plasmonic nanohole arrays. *Journal of the Optical Society of America B* **34,** 315 (2017).

68. Maoz, B. M. *et al.* Amplification of chiroptical activity of chiral biomolecules by surface plasmons. *Nano Letters* **13,** 1203–1209 (2013).

69. Nesterov, M. L., Yin, X., Schäferling, M., Giessen, H. & Weiss, T. The role of plasmon-generated near-fields for enhanced circular dichroism spectroscopy. *ACS Photonics* **3,** 578 –583 (2016).

70. Zhang, W., Wu, T., Wang, R. & Zhang, X. Surface-Enhanced Circular Dichroism of Oriented Chiral Molecules by Plasmonic Nanostructures. *The Journal of Physical Chemistry C* **121,** 666–675 (2017).

71. Lu, F. *et al.* Discrete nanocubes as plasmonic reporters of molecular chirality. *Nano Letters* **13,** 3145–3151 (2013).

72. Appleby, H. With or after, or sometimes beyond. It' s from the Greek, of course. *Yes, Minister* **Season 2,** 6′ 22″ (1982).

73. Pendry, J. B., Holden, a. J., Robbins, D. J. & Stewart, W. J. Magnetism from conductors and enhanced nonlinear phenomena. *IEEE Transactions on Microwave Theory and Techniques* **47,** 2075–2084 (1999).

74. Shelby, R. A., Smith, D. R. & Schultz, S. Experimental verification of a negative index of refraction. *Science* **292,** 77–9 (2001).

75. Smith, D. R., Pendry, J. B. & Wiltshire, M. C. K. Metamaterials and negative refractive index. *Science* **305,** 788–92 (2004).

76. Alitalo, P. & Tretyakov, S. Electromagnetic cloaking with metamaterials. *Materials Today* **12,** 22–29 (2009).

77. Chen, H., Chan, C. T. & Sheng, P. Transformation optics and metamaterials. *Nature Materials* **9,** 387–396 (2010).

78. Yang, B. *et al.* Direct observation of topological surface-state arcs in photonic metamaterials article. *Nature Communications* **8,** 1–7 (2017).

79. Lindmann, K. F. Rotation polarisation of electromagneticwaves generated by the isotropic system of spiral resonators. *Annalen der Physik* **63,** 621–644 (1920).

80. Pendry, J. B. A chiral route to negative refraction. *Science (New York, N.Y.)* **306,** 1353–5 (2004).

81. Gansel, J. K. *et al.* Gold helix photonic metamaterial as broadband circular polarizer. *Science (New York, N.Y.)* **325,** 1513–5 (2009).

82. Rogacheva, a. V., Fedotov, V. a., Schwanecke, a. S. & Zheludev, N. I. Giant Gyrotropy due to Electromagnetic-Field Coupling in a Bilayered Chiral Structure. *Physical Review Letters* **97,** 177401 (2006).

83. Gao, W. & Tam, W. Y. Optical activities in complementary double layers of six-armed metallic gammadion structures. *Journal of Optics* **13,** 015101 (2011).

84. Li, Z. *et al.* Chiral metamaterials with negative refractive index based on four "U" split ring resonators. *Applied Physics Letters* **97,** 081901 (2010).

85. Zhu, W., Rukhlenko, I. D., Huang, Y., Wen, G. & Premaratne, M. Wideband giant optical activity and negligible circular dichroism of near-infrared chiral metamaterial based on a complementary twisted configuration. *Journal of Optics* **15,** 125101 (2013).

86. Valev, V. K., Baumberg, J. J., Sibilia, C. & Verbiest, T. Chirality and chiroptical effects in plasmonic nanostructures: Fundamentals, recent progress, and outlook. *Advanced Materials* **25,** 2517–2534 (2013).

87. Falcone, F. *et al.* Babinet Principle Applied to the Design of Metasurfaces and Metamaterials. *Physical Review Letters* **93,** 197401 (2004).

88. Hentschel, M., Weiss, T., Bagheri, S. & Giessen, H. Babinet to the half: Coupling of solid and inverse plasmonic structures. *Nano Letters* **13,** 4428–4433 (2013).

89. Urade, Y., Nakata, Y., Nakanishi, T. & Kitano, M. Theoretical study on dynamical planar-chirality switching in checkerboard-like metasurfaces. *EPJ Applied Metamaterials* **4,** 2 (2017).

90. Cheng, Z. Z., Cheng, Y. Z. & Fang, C. Compact asymmetric metamaterial circular polarization transformer based on twisted double split-ring resonator structure. *Journal of Electromagnetic Waves and Applications* **28,** 485–493 (2014).

91. Fedotov, V. a. *et al.* Circular conversion dichroism in planar chiral metamaterials. *Physical Review Letters* **97,** 6 (2006).

92. Li, Z., Mutlu, M. & Ozbay, E. Chiral metamaterials: from optical activity and negative refractive index to asymmetric transmission. *Journal of Optics* **15,** 023001 (2013).

93. Jia, Y. P. *et al.* Complementary chiral metasurface with strong broadband optical activity and enhanced transmission. *Applied Physics Letters* **104** (2014).

94. Hannam, K., Powell, D. a., Shadrivov, I. V. & Kivshar, Y. S. Dispersionless optical activity in metamaterials. *Applied Physics Letters* **102,** 201121 (2013).

95. Liu, Z. *et al.* Single-Layer Plasmonic Metasurface Half-Wave Plates with Wavelength-Independent Polarization Conversion Angle. *ACS Photonics* **4,** 2061–2069 (2017).

96. Hooper, I. R., Tremain, B., Dockrey, J. A. & Hibbins, A. P. Massively sub-wavelength guiding of electromagnetic waves. *Scientific Reports* **4,** 1–5 (2014).

97. .

98. Jin, Y., He, J. & He, S. Surface polaritons and slow propagation related to chiral media supporting backward waves. *Physics Letters, Section A: General, Atomic and Solid State Physics* **351,** 354–358 (2006).

99. Engheta, N & Pelet, P. Surface waves in chiral layers. *Optics letters* **16,** 723–5 (1991).

100. Mi, G. & Van, V. Characteristics of surface plasmon polaritons at a chiral-metal interface. *Optics letters* **39,** 2028–31 (2014).

101. Pellegrini, G., Finazzi, M., Celebrano, M., Duò, L. & Biagioni, P. Chiral Surface Waves for Enhanced Circular Dichroism. arXiv: `1611.05782` (2016).

102. Kraus, J. The Helical Antenna. *Proceedings of the IRE* **37,** 263–272 (1949).

103. Cutler, C. C. Experimental Determination of Helical-Wave Properties. *Proceedings of the IRE* **36,** 230–233 (1948).

104. Sollfrey, W. Wave Propagation on Helical Wires. *Journal of Applied Physics* **22,** 905–910 (1951).

105. Sensiper, S. Electromagnetic Wave Propagation on Helical Structures (A Review and Survey of Recent Progress). *Proceedings of the IRE* **43,** 149–161 (1955).

106. McVay, J., Engheta, N. & Hoorfar, A. High Impedance Metamaterial Surfaces Using Hilbert-Curve Inclusions. *IEEE Microwave and Wireless Components Letters* **14,** 130–132 (2004).

107. De Zuani, S. *et al.* High-Order Hilbert Curves: Fractal Structures with Isotropic, Tailorable Optical Properties. *ACS Photonics* **2,** 1719–1724 (2015).

108. Fernández-Domínguez, A. I. *et al.* Terahertz surface plasmon polaritons on a helically grooved wire. *Applied Physics Letters* **93,** 10–13 (2008).

109. Rüting, F., Fernández-Domínguez, A. I., Martín-Moreno, L. & García-Vidal, F. J. Subwavelength chiral surface plasmons that carry tuneable orbital angular momentum. *Physical Review B - Condensed Matter and Materials Physics* **86,** 2–6 (2012).

110. Yao, H. & Zhong, S. Chiral Terahertz Surface Wave on the Helically Grooved Metal Wire. *Progress in Electromagnetic Research Symposium (PIERS)* **1,** 8–11.

111. Hibbins, A. P., Lockyear, M. J. & Sambles, J. R. Otto coupling to a transverse-electric-polarized mode on a metamaterial surface. *Physical Review B - Condensed Matter and Materials Physics* **84,** 1–5 (2011).

112. Dahlberg, O., Mitchell-Thomas, R. C. & Quevedo-Teruel, O. Reducing the Dispersion of Periodic Structures with Twist and Polar Glide Symmetries. *Scientific Reports* **7,** 1–6 (2017).

113. Mock, A., Lu, L. & O'Brien, J. Space group theory and Fourier space analysis of two-dimensional photonic crystal waveguides. *Physical Review B* **81,** 155115 (2010).

114. Knorr, Jeffrey B. and McIsaac, P. R. A Group Theoretic Investigation of the Single-Wire Helix. *IEEE Transactions on Microwave Theory and Techniques* **19,** 854–861 (1971).

115. Ghasemifard, F., Norgren, M. & Quevedo-Teruel, O. Dispersion Analysis of 2-D Glide-Symmetric Corrugated Metasurfaces Using Mode-Matching Technique. *IEEE Microwave and Wireless Components Letters* **28,** 1–3 (2018).

116. Camacho, M., Mitchell-Thomas, R. C., Hibbins, A. P., Roy Sambles, J. & Quevedo-Teruel, O. Designer surface plasmon dispersion on a one-dimensional periodic slot metasurface with glide symmetry. *Optics Letters* **42,** 3375 (2017).

117. Hessel, A., Oliner, A. A., Chen, M. H. & Li, R. C. Propagation in Periodically Loaded Waveguides with Higher Symmetries. *Proceedings of the IEEE* **61,** 183–195 (1973).

118. Maurin, F., Claeys, C., Van Belle, L. & Desmet, W. Bloch theorem with revised boundary conditions applied to glide, screw and rotational symmetric structures. *Computer Methods in Applied Mechanics and Engineering* **318,** 497–513 (2017).

119. Niklasson, G. A. & Granqvist, C. G. Effective medium models for the optical properties of inhomogeneous materials. *Applied Optics* **20,** 26 –30 (1981).

120. Gorlach, M. A., Voytova, T. A., Lapine, M., Kivshar, Y. S. & Belov, P. A. Nonlocal homogenization for nonlinear metamaterials. *Physical Review B - Condensed Matter and Materials Physics* **93,** 1–9 (2016).

121. Chung, C. Y. & Whites, K. W. Effective constitutive parameters for an artificial uniaxial bianisotropic chiral medium. *Journal of Electromagnetic Waves and Applications* **10,** 1363–1388 (1996).

122. Whites, K. W. & Chung, C. Y. Composite uniaxial bianisotropic chiral materials characterization: comparison of predicted and measured scattering. *Journal of electromagnetic waves and applications* **11,** 371–394 (1997).

123. Gorlach, M. A. & Belov, P. A. Nonlocality in uniaxially polarizable media. *Physical Review B* **085107,** 1–5 (2015).

124. Ciattoni, A. & Rizza, C. Nonlocal homogenization theory in metamaterials: Effective electromagnetic spatial dispersion and artificial chirality. *Physical Review B - Condensed Matter and Materials Physics* **91,** 42–45 (2015).

125. Zhao, R., Koschny, T. & Soukoulis, C. M. Chiral metamaterials: retrieval of the effective parameters with and without substrate. *Optics express* **18,** 14553–14567 (2010).

126. Wang, B., Zhou, J., Koschny, T., Kafesaki, M. & Soukoulis, C. M. Chiral metamaterials: simulations and experiments. *Journal of Optics A: Pure and Applied Optics* **11,** 114003 (2009).

127. Agilent Tecnologies inc. *Agilent Network Analyser Basics* (2004).

128. Gogoi, J. P., Bhattacharyya, N. S. & James Raju, K. C. Synthesis and microwave characterization of expanded graphite/novolac phenolic resin composite for microwave absorber applications. *Composites Part B: Engineering* **42,** 1291–1297 (2011).

129. Li, Z. *et al.* Coupling effect between two adjacent chiral structure layers. *Optics express* **18,** 5375–83 (2010).

130. Monzon, C. & Forester, D. W. Negative refraction and focusing of circularly polarized waves in optically active media. *Physical Review Letters* **95,** 1–4 (2005).

131. Dong, J., Zhou, J., Koschny, T. & Soukoulis, C. Bi-layer cross chiral structure with strong optical activity and negative refractive index. *Optics express* **17,** 14172–14179 (2009).

132. Zhou, J. *et al.* Negative refractive index due to chirality. *Physical Review B - Condensed Matter and Materials Physics* **79,** 3–6 (2009).

133. Decker, M. *et al.* Strong optical activity from twisted-cross photonic metamaterials. *Optics Letters* **34,** 2501 (2009).

134. Li, Z., Alici, K. B., Colak, E. & Ozbay, E. Complementary chiral metamaterials with giant optical activity and negative refractive index. *Applied Physics Letters* **98,** 161907 (2011).

135. Hannam, K., Powell, D. A., Shadrivov, I. V. & Kivshar, Y. S. Broadband chiral metamaterials with large optical activity. *Physical Review B - Condensed Matter and Materials Physics* **89,** 1–6 (2014).

136. Luk'Yanchuk, B. *et al.* The Fano resonance in plasmonic nanostructures and metamaterials. *Nature Materials* **9,** 707–715 (2010).

137. Kenanakis, G., Economou, E. N., Soukoulis, C. M. & Kafesaki, M. Controlling THz and far-IR waves with chiral and bianisotropic metamaterials. *EPJ Applied Metamaterials* **2,** 15 (2015).

138. Genet, C. & Ebbesen, T. W. Light in tiny holes. *Nature* **445,** 39–46 (2007).

139. Grigorenko, a. N., Nikitin, P. I. & Kabashin, a. V. Phase jumps and interferometric surface plasmon resonance imaging. *Applied Physics Letters* **75,** 3917–3919 (1999).

140. Zhao, Y. *et al.* Chirality detection of enantiomers using twisted optical metamaterials. *Nature Communications* **8,** 14180 (2017).

141. Gorecka, E *et al.* Enhanced chirality by adding achiral molecules into the chiral system. *Physical Review E* **67,** 61704 (2003).

142. Bliokh, K. Y., Bekshaev, A. Y. & Nori, F. Extraordinary momentum and spin in evanescent waves. *Nature communications* **5,** 14 (2013).

143. Bliokh, K. Y., Alonso, M. a., Ostrovskaya, E. a. & Aiello, A. Angular momenta and spin-orbit interaction of nonparaxial light in free space. *Physical Review A - Atomic, Molecular, and Optical Physics* **82,** 4–10 (2010).

144. Coles, M. M. & Andrews, D. L. Chirality and angular momentum in optical radiation. *Physical Review A - Atomic, Molecular, and Optical Physics* **85,** 1–17 (2012).

145. Poulikakos, L. V. *et al.* The Optical Chirality Flux as a Useful Far-Field Probe of Chiral Near Fields. *ACS Photonics* **9,** 1–10 (2016).

146. Andrews, D. L. & Coles, M. M. Optical superchirality and electromagnetic angular momentum. *Spie Opto* **8274,** 827405–827405–7 (2012).

147. Hendry, E., Mikhaylovskiy, R. V., Barron, L. D., Kadodwala, M. & Davis, T. J. Chiral electromagnetic fields generated by arrays of nanoslits. *Nano Letters* **12,** 3640–3644 (2012).

148. Barron, L. D. Fundamental symmetry aspects of chirality. *Bio Systems* **20,** 7–14 (1987).

149. Yang, N. & Cohen, A. E. Local geometry of electromagnetic fields and its role in molecular multipole transitions. *Journal of Physical Chemistry B* **115,** 5304–5311 (2011).

150. Drexhage, K. H. Influence of a dielectric interface on fluorescence decay time. *Journal of Luminescence* **1-2,** 693–701 (1970).

151. Barnes, W. L. Fluorescence near interfaces: the role of photonic mode density. *Journal of Modern Optics* **45,** 661–699 (1998).

152. Plum, E. Extrinsic chirality: Tunable optically active reflectors and perfect absorbers. *Applied Physics Letters* **108** (2016).

153. Hau, L. V., Harris, S. E., Dutton, Z. & Behroozi, C. H. Light speed reduction to 17 metres per second in an ultracold atomic gas. *Nature* **397,** 594–598 (1999).

154. Matsuda, N. *et al.* Slow light enhanced optical nonlinearity in a silicon photonic crystal coupled-resonator optical waveguide. *Optics Express* **19,** 19861 (2011).

155. Scullion, M. G., Arita, Y., Krauss, T. F. & Dholakia, K. Enhancement of optical forces using slow light in a photonic crystal waveguide. *Optica* **2,** 816 (2015).

156. Atre, A. C., García-Etxarri, A., Alaeian, H. & Dionne, J. A. Toward high-efficiency solar upconversion with plasmonic nanostructures. *Journal of Optics* **14,** 024008 (2012).

157. Yu, L., Liu, G. L., Kim, J., Mejia, Y. X. & Lee, L. P. Nanophotonic crescent moon structures with sharp edge for ultrasensitive biomolecular detection by local electromagnetic field enhancement effect. *Nano Letters* **5,** 119–124 (2005).

158. Challener, W. A. *et al.* Heat-assisted magnetic recording by a near-field transducer with efficient optical energy transfer. *Nature Photonics* **3,** 220–224 (2009).

159. Chikkaraddy, R. *et al.* Single-molecule strong coupling at room temperature in plasmonic nanocavities. *Nature* **535,** 127–130 (2016).

160. Savo, S., Casse, B. D., Lu, W. & Sridhar, S. Observation of slow-light in a metamaterials waveguide at microwave frequencies. *Applied Physics Letters* **98,** 1–4 (2011).

161. Lu, W. T., Savo, S., Casse, B. D. F. & Sridhar, S. Slow Microwave Waveguide Made of Negative Permeability Metamaterials. *Microwave and Optical Technology Letters* **5,** 2705 (2009).

162. Tsakmakidis, K. L., Hess, O., Boyd, R. W. & Zhang, X. Ultraslow waves on the nanoscale. *Science* **358.**

163. Impagliazzo, J. Multimode Propagation on Radiating Traveling-Wave Structures with Glide-Symmetric Excitation. *IEEE Transactions on Antennas and Propagation* **AP-18,** 3–7 (1970).

164. Crepeau, P. J. & McIsaac, P. R. Consequences of Symmetry in Periodic Structures. *Proceedings of the IEEE* **52,** 33–43 (1964).

165. Ebrahimpouri, M., Rajo-Iglesias, E., Sipus, Z. & Quevedo-Teruel, O. Low-cost metasurface using glide symmetry for integrated waveguides. *2016 10th European Conference on Antennas and Propagation, EUCAP 2016*, 5–6 (2016).

166. Quesada, R. Waveguiding Enabled By Coupled Conformal Surface Plasmons. *Optics Letters* **39,** 2990–2993 (2014).

167. Maci, S. & Neto, A. Green's function of an infinite slot printed between two homogeneous dielectrics - Part II: Uniform asymptotic solution. *IEEE Transactions on Antennas and Propagation* **52,** 666–676 (2004).

168. Neto, A. & Maci, S. Green's function for an infinite slot printed between two homogeneous dielectrics - Part I: Magnetic currents. *IEEE Transactions on Antennas and Propagation* **51,** 1572–1581 (2003).

169. Liu, K., Ghasemifard, F. & Quevedo-Teruel, O. Broadband metasurface Luneburg lens antenna based on glide-symmetric bed of nails. *2017 11th European Conference on Antennas and Propagation, EUCAP 2017,* 358–360 (2017).

170. Quevedo-Teruel, O., Ebrahimpouri, M. & Ng Mou Kehn, M. Ultrawideband Metasurface Lenses Based on Off-Shifted Opposite Layers. *IEEE Antennas and Wireless Propagation Letters* **15,** 484–487 (2016).

171. Ebrahimpouri, M., Quevedo-Teruel, O. & Rajo-Iglesias, E. Design guidelines for gap waveguide technology based on glide-symmetric holey structures. *IEEE Microwave and Wireless Components Letters* **27,** 542–544 (2017).

172. Knight, D. W. *The self-resonance and self-capacitance of solenoid coils* 1–29 (2010).

173. Choi, M. *et al.* A terahertz metamaterial with unnaturally high refractive index. *Nature* **470,** 369–373 (2011).

174. Lapine, M., Shadrivov, I. V., Powell, D. a. & Kivshar, Y. S. Magnetoelastic nonlinear metamaterials. *Nature Materials* **11,** 4 (2011).

175. Slobozhanyuk, A. P. *et al.* Flexible helices for nonlinear metamaterials. *Advanced Materials* **25,** 3409–3412 (2013).

176. Collin, R. E. *Field Theory of Guided Waves* 851 (IEEE Press, 1990).

177. Liu, L.-L. *et al.* A corrugated perfect magnetic conductor surface supporting spoof surface magnon polaritons. *Optics Express* **22,** 10675 (2014).

178. Zhu, B. O. *et al.* Dynamic control of electromagnetic wave propagation with the equivalent principle inspired tunable metasurface. *Scientific Reports* **4,** 1–7 (2014).

179. Yang, Z. Optical orbital angular momentum of evanescent Bessel waves. *Optics Express* **23,** 12700 (2015).

180. Spektor, G. *et al.* Revealing the subfemtosecond dynamics of orbital angular momentum in nanoplasmonic vortices. *Science* **355,** 1187–1191 (2017).